Measuring adhesion and friction in mems

Kokorian, J.

DOI
10.4233/uuid:14746f2d-786f-4176-8418-25b75e2c19b6

Publication date
2020

Document Version
Final published version

Citation (APA)
Kokorian, J. (2020). *Measuring adhesion and friction in mems*. [Dissertation (TU Delft), Delft University of Technology]. https://doi.org/10.4233/uuid:14746f2d-786f-4176-8418-25b75e2c19b6

MEASURING ADHESION AND FRICTION IN MEMS

Dissertation

for the purpose of obtaining the degree of doctor
at Delft University of Technology,
by the authority of Rector Magnificus prof. dr ir. T.H.J.J. van der Hagen,
chair of the Board for Doctorates,
to be defended publicly on
Tuesday, December 22, 2020, at 10:00 o'clock

by

Jaap KOKORIAN

Master of Science in Electrical Engineering, University of Twente, the Netherlands,
born in Paris, France

This dissertation has been approved by the promotor and the copromotor.

Composition of the doctoral committee:

Rector Magnificus,	chairperson
Prof. dr. U. Staufer,	Delft University of Technology, *promotor*
Dr. ir. W. M. van Spengen,	Delft University of Technology, *copromotor*

Independent members:

Prof. dr. ir. L. Abelmann,	University of Twente
Prof. dr. P. J. French	Delft University of Technology
Prof. dr. G. C. A. M. Janssen	Delft University of Technology, *reserve member*
Prof. dr. E. Meyer,	University of Basel, Switzerland
Dr. ir. R. A. J. van Ostayen	Delft University of Technology

The research described in this PhD thesis has been financially sponsored by the Dutch NWO-STW foundation in the 'Vidi' program under ref. no. 10771.

Cover: A MEMS adhesion sensor inside a temperature-controlled vacuum chamber underneath a microscope. Cover design by Lisanne Brouwer.

ISBN 978-94-6366-348-9

An electronic version of this dissertation is available at

http://repository.tudelft.nl/

To my grandfathers

Krikor ‘Papachig’ Kokorian
(1924 – 2015)

Heinrich Gustav Niehus
(1921 – 2011)

CONTENTS

1

INTRODUCTION

"For every complex question, there is a simple answer. And it is wrong."

(Andreas M. Antonopoulos)

My grandfather once set out to build an engine that would run forever, and would even generate more energy in the process: a perpetual motion machine. It didn't work of course, because of the most fundamental property of our universe we know of: the second law of thermodynamics. The second law states that entropy always increases, which popularly translates to "chaos always increases" or "there is no such thing a free lunch". Chaos theory and pseudoscience aside, the second law has a far more mundane consequence, which prevented my grandfather from solving the 1970s oil crisis, but enabled our prehistoric ancestors to make fire: when two things are rubbed together, they get hot.

This book is about the things that happen when things touch each other, and also about the things that happen when things move while touching each other; adhesion science and tribology.

For millennia, people have been trying to control the forces of adhesion and friction. Figure 1.1 shows the earliest image we have of a tribologist at work. It depicts an ancient Egyptian dumping a slurry in front off a sled that carries a huge stone statue, and it dates back to the year 2000 BC. The study of tribology has existed ever since, and we invented many more lubricants to make things slippery, rubber compounds to make things grippy, adhesives to make things sticky, and hard ceramics to make things durable.

Despite numerous innovations however, many problems associated with friction in particular remain unsolved. A large part of the world's energy production is lost as heat in the frictional contacts of machinery. Finding a structural way to decrease the amount of friction between moving components, even by a tiny fraction, would save vast amounts of energy.

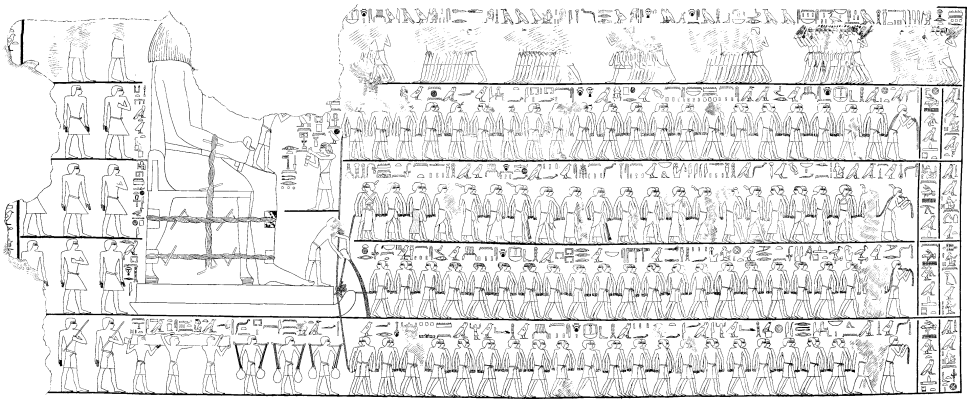

Figure 1.1.: The ancient Egyptian dumping the liquid in front of the sled that carries the huge statue may well be the first tribologist in recorded history [1].

1.1. CONTACT MECHANICS AT DIFFERENT SCALES

Adhesion science and tribology are two branches within the multi-disciplinary field of contact-mechanics, which involve traditional sciences such as chemistry, physics, materials science, as well as many engineering sciences. Research on contact mechanics is split into three different fields: macro-scale contact mechanics, nano-scale contact mechanics, and meso-scale contact mechanics.

The field of macro-scale contact mechanics is occupied with modelling and acquiring data on lubricants, friction coefficients and wear rates, under a large number of circumstances. This is extremely valuable information for designing a large ('macro') mechanical system like an engine, a mars rover, or a oil drill. Much of the macro-scale tribological research has a direct application in engineering.

The field of nano-scale, or atomic-scale contact mechanics, is relatively young, and is occupied with the study of adhesion, friction and wear on a more fundamental level. Great advances have been made in our understanding of atomic scale friction due to the invention of the Atomic Force Microscope (AFM), and in particular the Friction Force Microscope (FFM). In both forms of microscopy, an atomically sharp needle on the tip of a micro-meter sized cantilever is used to measure atomic-scale forces, and can resolve individual atoms on a surface.

The difference between the physics of a macro-scale contact and an atomic scale contact is the number of points, or *asperities* at which the contacting surfaces actually make intimate contact. In a macro-scale contact, the number of asperities approaches infinity. The consequence of this is that the complex physics of the individual asperities are 'averaged out', and only phenomenological models can be created.

Atomic-scale contacts, on the other hand, have only a single asperity: the tip of the FFM. Mechanically, this is a much simpler system, and the Prandtl–Tomlinson model [2]

predicts the tip motion of an FFM with reasonable accuracy. There are phenomenological models [3–7] which predict the behaviour of macro-scale friction forces to a certain extend. However, the differences in experimental conditions between atomic- and macro-scale contacts are simply too great to create a model capable of predicting the tabulated macro-scale data from first principles.

The missing link is to be found at the meso-scale, which sits in between the macro-scale and the atomic scale. The number of asperities in a meso-scale contact is larger than one, but too small to be considered infinite. As we shall see, this means that the meso-scale combines the disadvantages of both the atomic-scale and the macro-scale. Everything is very small, and it is hard to model.

Unlike atomic-scale contact mechanics though, research on meso-scale contacts has direct practical relevance to the domain of microsystems and microtechnology, and in particular to the design of microelectromechanical systems (MEMS).

1.2. MICROELECTROMECHANICAL SYSTEMS (MEMS)

Since the invention of the transistor in 1947, the electronics industry has strived to make transistors as small as possible. Decreasing the size of a transistor makes it faster, more energy efficient, and allows more of them to be squeezed into the same area. In the early days, transistors were discrete components that were soldered together manually, in order to create functional electrical circuits. The tedium of manual assembly was reduced significantly with the invention of the Integrated Circuit (IC): a single, monolithic piece of silicon that contains all the transistors and the interconnections between them. ICs are fabricated in complex processes involving multiple steps of photolithography. These processes are incredibly expensive to setup and run, but they eventually allow thousands of identical ICs to be created in a single batch, which reduces the cost per device to almost nothing. Due to the industry's continuing success in keeping up with Moore's law [8], the component density of ICs doubles every 18 months, and transistors with channel lengths as short as 5 nm are now a reality.

The same technology used to fabricate ICs can also be used to make small mechanical structures, called microelectromechanical systems (MEMS). Many MEMS devices have already found their ways into our daily lives, the sensor that triggers the airbag in a car, the accelerometers, gyroscopes, and microphones in smartphones, inkjet printer heads, and the two-dimensional arrays of tiny mirrors that create the image in a digital projector (see figure 1.2).

These are just the examples of the prevalent commercial successes, but there is a myriad of experimental devices being developed: femtoliter pipettes [9], scanners [10, 11], Coriolis mass-flow sensors [12], automatic optical fiber aligners [13]... The list is almost endless and keeps growing.

Replacing existing components by equivalent MEMS alternatives can lower the costs per unit significantly, because of the advantages provided by the IC manufacturing technology. More importantly, however, the behaviour of MEMS devices can be vastly different

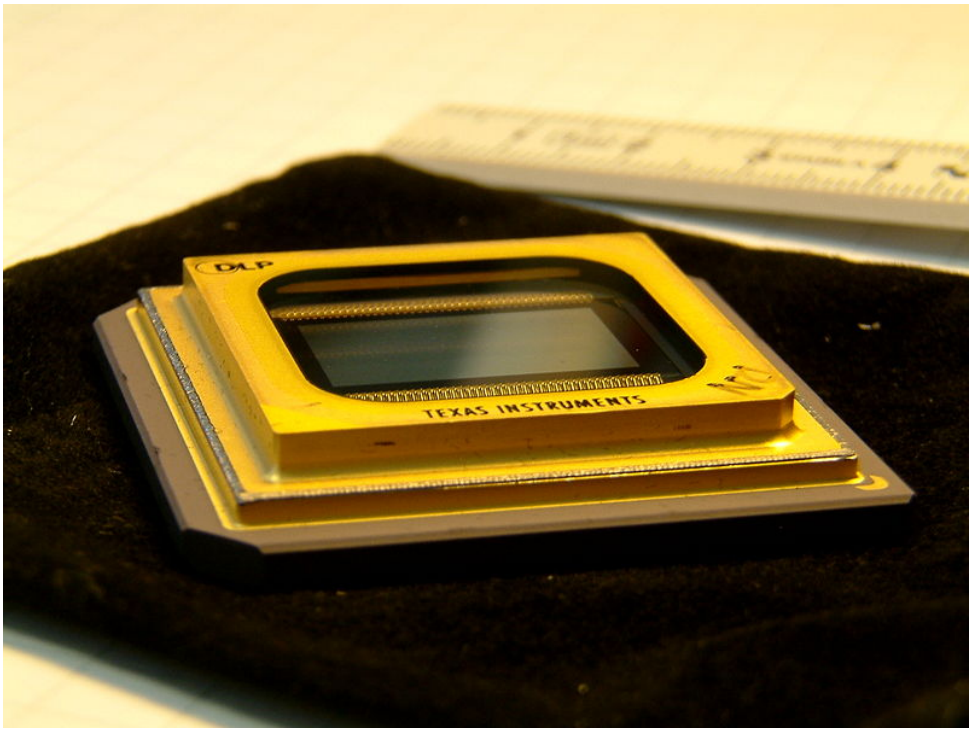

Figure 1.2.: The Texas Instruments Digital Micromirror array. The only commercially successful MEMS device that relies on touching components for its operation. The DMD can be found in many beamers, where it modulates a uniform light source into an image. Each mirror can be in 'on' position, where it reflects the light towards the projector lenses and the pixel is at maximum brightness, or in an 'off' position, where it reflects the light onto a heat sink, and the pixel is fully dark. Different grayscale values are created by alternating the mirror between its on and off state at a high frequency. Image source: wikimedia commons.

compared to an equivalent macro-scale machine, because the laws of physics manifest themselves differently at small scales. This unlocks many new possibilities and applications, while simultaneously opening up a Pandora's box of challenges to overcome.

1.3. SCALING DOWN MECHANICAL SYSTEMS

The behaviour of any mechanical system is determined by the balance between a number of forces: gravity, inertial forces, magnetic forces, electrostatic forces, adhesion, friction, etc. All forces are proportional to the scale of the system. When a system is scaled down in size, all forces decrease in magnitude, but they do so at different rates. This results in a change of the force balance, which creates many possibilities. The decrease of inertial and gravitational forces in particular, shifts the force balance in a positive manner. For example, diamagnetic forces are usually negligible. At micrometer dimensions however, they are much stronger than gravity, enabling futuristic scenarios such as passive levitation of magnets [14, 15] and droplets of water [16].

1.3.1. UNRELIABILITY BECAUSE OF SCALING

However, not all scaling effects are beneficial. When mechanical components are sized down far enough, forces that are proportional to surface area will become dominant over forces that are proportional to volume. This means that adhesion and friction forces will dominate the behaviour of systems with contacting surfaces.

An important aspect of downscaling a mechanical system is that only the features that are designed by the engineer are actually scaled: the structure and roughness of the materials does not change. When two surfaces come into contact in a macro-scale contact, the number of points at which the surfaces make contact approaches infinity. In a MEMS device this is not the case, which has an important consequence: the size and shape of the contact become dependent on the exact location of the contact [17]. This is illustrated in figure 1.3. Every mechanical contact is fundamentally different, even though the roughness statistics of the contacting surfaces are identical. This effect causes a large spread in contact phenomena within a single device and between separate devices.

The dominance of surface interactions in MEMS combined with their unpredictability has a detrimental effect on the reliability of small scale devices that depend on touching or sliding components for their functionality. This is best illustrated with a small thought experiment, downscaling an everyday macro-scale scenario to the micro-scale. First we will focus on what happens when two objects first make contact, and treat the phenomenon of adhesion. Then we will focus on what happens when objects slide, and treat the phenomenon of friction.

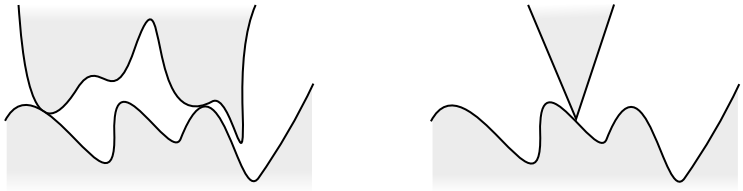

Figure 1.3.: Schematic overview of a meso-scale multi-asperity contact and a nano-scale single asperity contact. The meso-scale differs from the nano-scale by the number of contact points, or asperities between two contacting surfaces. A single asperity means nano-scale, an infinity number of asperities means macro-scale, and everything in between means meso-scale.

ADHESION

Adhesion refers to the phenomena of 'things sticking together'. This always happens when two objects touch each other, even when the effect is unnoticeable on a macro-scale. When you place a glass of milk on a table for example, the glass and the table will stick together. The reason we don't notice this when we pick up the glass, is that the glass is relatively heavy, and our muscles are very powerful by comparison. The extra force required to overcome the tiny adhesion force that glues the glass to the table is completely irrelevant compared to the force of gravity we already needed to overcome in order to lift the glass into the air.

We may notice some adhesive forces when the glass has a flat bottom, and the table is slightly wet. This is because of capillary effects that 'suck' the water out from underneath the glass, forming a ring around the edge. Although in this case we would notice the adhesion force, our muscles are strong enough to overcome it.

Now imagine we make everything a factor of $s = 10^4$ smaller, creating a MEMS version of the glass, the table, and ourselves. The force generated by our muscles, as well as the force of gravity generated by the mass of the glass, are proportional to their respective volumes. Both forces therefore decrease by a factor of $s^3 = 10^{12}$. The surface area of the bottom of the glass on the other hand, decreases only by a factor $s^2 = 10^8$. Adhesion forces scale with surface area, which means that compared to the force of gravity, the force of adhesion has become ten thousand times more relevant to our microscopic muscles than it was originally.

If our original glass has a mass of 200 g and its bottom has a diameter of 5 cm, the MEMS version of it would have a diameter of 50 µm: roughly the thickness of a human hair. Its mass would be a mere 200 pg: a tiny speck of dust. Assuming the table is of the 'rustic' kind: not very clean and full of dents and grooves, the MEMS table would still be exactly as rustic as before, even though its total area will have decreased. This is because the dimensions of the topological imperfections of the table surface are a material property, which does not scale down with the dimensions of the system.

When we now put down the glass on the table, it matters at what exact position we do so. The bottom of the original glass covered multiple grooves and dents, but the MEMS glass will now fit entirely inside one single groove. Moreover, the adhesive force generated by the capillary action of the water on the table surface, will suck the glass down and trap it there permanently, an effect referred to as stiction. Our tiny muscles will not have enough strength to pull it free again.

FRICTION

Friction is what happens when things are rubbed together. Usually when friction is to high, you apply an appropriate lubricant, or when friction is too low, you sprinkle some sand between the rubbing parts, or you make one of the parts out of rubber. For macro-scale mechanics, a wealth of empirical data is available on the magnitude of the friction force for different materials, at different pressures, temperatures, with different lubricants, etc. This makes it relatively straightforward to select the proper materials and lubricants for a specific engineering purpose.

At the micro-scale, things are rather different, and we will see why by reverting to the example of the MEMS glass on the rustic table. Imagine now that the table still has all of its grooves and dents, but has been thoroughly cleaned and dried, reducing the capillary adhesion force to zero. Furthermore, imagine scaling everything down further by a factor 100, to a total scaling factor of one million. The bottom of the glass will now have a diameter of only 500 nm, which is a realistic size for a MEMS contact.

If we would attempt to find out how much force it would require to slide our glass over the tabletop by using the macro-scale data available on glass–wood interactions, we would fail. This is because the data was obtained in an experiment where the surface of the glass was in contact with a large number of wood fibers and it touched each fiber at an infinite number of asperities.

In our earlier example we silently assumed that the glass was perfectly smooth, and the only irregular thing about the table surface were its dents and grooves. Now, however, the size of the glass is in the same order of magnitude as the microscopic roughness of the glass material itself, so the number of asperities at which it touches the surface is no longer infinite. When we set it down on the table, the tiny glass may end up exactly between two fibers of wood, in which case it is completely stuck, and the macro-scale data is useless. It may also end up on top of a single fiber of wood. The roughness of a single fiber however, has no relationship with the apparent roughness of the complete table top, so the macro-scale data is useless in this case as well.

1.3.2. INTUITION AND SMALL-SCALE PHENOMENA

Of course, the example of the MEMS glass of milk on the wooden table is a bit artificial. No MEMS designer in his right mind would use wood as a structural material when a flat surface is required. The issues related to capillary condensation and surface roughness are very real, however. As we shall see now, this is only the beginning.

Because of the nano-meter distances and limited number of asperities involved in meso-scale contact mechanics, we will have to deal with phenomena usually only encountered on the atomic scale. It has been demonstrated that very thin layers of water are much more viscous than usual, making them act as glue [18], or even turning them into ice[19]. Under some circumstances, the force of friction has been shown to vanish completely, an effect known as superlubricity [20, 21]. Both of these phenomena are likely to manifest themselves in meso-scale systems as well [22]. Especially the discovery of superlubricity rekindles the hope that there may indeed be a way to lower the friction force in all mechanical systems, large and small. Once more we are directed towards meso-scale research, where the gap between the atomic scale and the macro scale may be bridged.

It is clear that our natural intuition for "what will work, and what won't work", cannot be relied upon when reasoning about meso-scale phenomena. Tiny insects would be much better equipped to design MEMS if they would have the mental capacity to do so: they are used to living in a world where one can walk on water, or swim in air, and where one can drown in a tiny bit of syrup. The only way to improve our intuition, is by gathering empirical data, and by performing *in-situ* measurements of meso-scale contact phenomena.

1.4. MEASURING MESO-SCALE PHENOMENA IS HARD

As we have seen, macro-scale empirical data and the models derived from it, cannot be relied upon when making predictions about the behavior of micro-scale contacts. It is therefore important to obtain data and create models specifically for micro-scale contacts. There are two main reasons this is hard to accomplish: first, it is nearly impossible to design an experiment that yields repeatable results under 'real-world' circumstances due to the unpredictable topology (and chemistry) of the contacting surfaces.

Second, we simply have not been able to measure what exactly happens in micro-scale contact. Although the interaction forces between the contacting surfaces are large enough to cause permanent failure of a MEMS device, these forces are still extremely small to for a typical measurement instrument. The phenomena that are likely to occur in micro-scale contact mechanics range from atomic scale forces and displacements, to almost macro-scale forces and displacements. These quantities have not yet been measured with sufficient resolution, and without the need to average hundreds of measurements together.

1.4.1. MICRO-SCALE APPROXIMATION TECHNIQUES

Surface interaction phenomena in MEMS devices are often studied using techniques common to the macro scale or the atomic scale that are adapted to replicate micro-scale conditions. Results from AFM or FFM measurements are often extrapolated to make claims about MEMS devices. However, the characteristic multi-asperity contact mechanics of MEMS devices are very different from the single-asperity contact mechanics of an AFM. It is possible to perform a multi-asperity measurement with an AFM by replacing

the atomically sharp tip by a tiny sphere. However, performing an AFM measurement on an etched sidewall of a MEMS device is highly impractical. A macro-scale version of this device is the ball-on-flat tribometer, which suffers from the same deficit: it fails to accurately recreate the conditions present in a real MEMS device because it does not have the same etched surfaces. In addition, the resolution of these measurements is too low to capture the small forces of interest.

1.5. MOTIVATION FOR THIS THESIS

With the advancements of AFM and FFM technologies, we are getting a firm grasp on the elementary physics of friction and adhesion for single asperity, atomic-scale contacts. Thanks to centuries of macro-scale tribology research, we also have an accurate view of the emergent properties of many atomic-scale contacts brought together. What we cannot do yet, is to deduce the empirical models of the macro scale, from the physical models of the atomic scale. The reason for the existence of this knowledge gap is that we still have a very limited understanding of the unique physics at play at the meso scale.

What we need most of all in order to increase our understanding of meso-scale contact mechanics, is a reliable method to perform measurements inside real MEMS devices, with sufficient resolution to expose atomic-scale details of the contact-mechanics.

1.5.1. MAIN AIM

The aim of the work described in this thesis is to find and test an experimental method to expose the atomic-scale details of meso-scale contact mechanics. We will develop a system to measure the atomic-scale phenomena that constitute the emergent properties of a meso-scale contact, thereby laying the foundations that will allow a final closure of the gap between atomic-scale and macro-scale contact mechanics.

1.6. OUTLINE

In part I, we will first treat the details of the measurement technology. In chapter 2 we demonstrate an optical technique to measure sub-nanometer in-plane displacements using a normal optical microscope and a Charge-Coupled Device (CCD) or Complementary Metal-Oxide-Semiconductor (CMOS) camera. We analyze how factors such as contrast, camera resolution and light intensity influence the measurement resolution. We also show how this method can be used to measure adhesion forces between two etched sidewalls in a MEMS tribometer. In chapter 3 we will apply the technique for executing high-speed measurements with a line-scan camera, and demonstrate how it can be used to measure the dynamics of MEMS.

In part II, we will apply the measurement technique treated in part I, to study the evolution of adhesion and friction forces in MEMS. In chapter 4 we characterize how the *run-in* of sidewall contacts, and measure the evolution of the adhesion force differs between several

'identical' MEMS tribometers. In chapter 5 we will demonstrate the difference in the evolution of the adhesion force between a clean and a contaminated MEMS tribometer. Nanometer-sized deviations in the measured displacements, indicate that a rubber-like compound formed at the contacts, after millions of repeated contacts.

In chapter 6 we leave the topic of adhesion behind, and proceed with the measurement of the evolution of friction forces in MEMS, during millions of sliding motions. To cope with the large volume of raw data produced in this experiment, we introduce several new ways of visualizing and analyzing friction force measurements. This allows us to unravel two separate energy dissipation modes.

I

MESO-SCALE MEASUREMENTS WITH ATOMIC RESOLUTION

2

AN OPTICAL IN-PLANE DISPLACEMENT MEASUREMENT TECHNIQUE WITH SUB-NANOMETER RESOLUTION

In this chapter we introduce a new optical method for determining in-plane displacements in MEMS with deep sub-nanometer resolution. We give a thorough analysis of the factors that influence the measurement resolution and we validate the method by measuring the adhesion force between two silicon MEMS sidewalls. We conclude that the best resolution is obtained by maximizing the amount of light that illuminates the MEMS device, and by maximizing the contrast of the digital image.

This chapter was published as a standalone journal paper [23]. Some editorial changes where added for inclusion in this thesis.

2.1. INTRODUCTION

2.1.1. THE OBSERVATION OF MOTION IN MEMS

Since the advent of MEMS in the 1980s, many measurement techniques have been used to study the lateral and out-of-plane motions of these tiny devices. Although capacitive sensing is commonly used in commercial products like accelerometers and gyroscopes, this method has disadvantages when used in the lab due to the fact that parasitic capacitances cause excessive noise if the readout chip is not monolithically integrated with the moving MEMS [24], or at least placed right next to it in the same package. Also, it is difficult to unambiguously detect motion if it occurs in more then one dimension at the same time, and detection speed is often limited.

For this reason, many optical motion detection methods are in use as well. Commonly applied for out-of-plane motion assessment is laser Doppler vibrometry [25], TV holography [26] or interferometry, either with continuous illumination [27] or stroboscopic illumination [28]. All these techniques have in common that they provide a considerably higher precision than the optical resolution limit, caused by the wavelength of the light with which the object is being imaged. They accomplish this, in one way or another, by making use of the wave nature of light.

It is difficult to use interference to enhance in-plane motion detection, which is why considerably fewer techniques are available, and they are not employed as often as the out-of-plane methods [29]. However, in-plane motion detection is important because many MEMS devices exhibit in-plane motion of some sort, comb drive actuators being a notorious example. Typical motion ranges are in the microns but can usually be controlled down to the nanometer level. The high accuracy of these actuators calls for detection methods to be considerably better than the raw resolution that can be obtained by simple optical imaging. The resolution of optical microscopy is limited roughly by the wavelength of the light being used, which is known as the Rayleigh criterion or the optical diffraction limit. In a typical high-quality microscope this amounts to around 500 nm. In this chapter, we present a powerful method to circumvent this limit.

2.1.2. IN-PLANE MOTION DETECTION TECHNIQUES CIRCUMVENTING THE RESOLUTION LIMIT

Several methods exist that enhance the resolution of in-plane motion detection beyond the Rayleigh criterion to monitor the motion of MEMS devices.

For studies on relatively large-scale motion, as in the assessment of the reliability of the rotating gear train MEMS devices of Sandia National Laboratories [30], no sub-wavelength resolution was actually required. Simple edge enhancement was sufficient to obtain an accurate measure for the rotational angle of the cogwheels. To follow the fast moving microscopic parts, stroboscopic illumination was employed.

Widely used is digital image correlation [31, 32], a method that has been investigated thoroughly by Davis and Freeman [33]. Guo *et al.* [34] use a similar technique based on

optical flow: a mathematical concept that formalizes the concept difference between two images in terms of motion, which can be calculated using image correlation.

The basic principle is that a shifted version of an image of a device at rest, the 'template', is used to find the position of the device in another image that is made when displacement has taken place. The image of the device is assumed to be constant in shape and intensity, and hence by shifting the template image progressively with respect to the new image B and calculating the correlation for every position, a maximum can be found in the correlation function that corresponds to the new position. To find this position accurately, the template image needs to be displaced by sub-pixel amounts, which means that a new image needs to be generated by interpolation between the pixels of the original template. Results with nanometer resolution can be obtained, and even sub-nanometer if spatio-temporal filtering is employed [35, 36]. The latter technique however, requires the motion of the device to be smooth, without any jerks or sudden stops. If the motion is jerky, this will be smoothed due to the filtering.

Powerful as the technique may be, one drawback seriously limits the accuracy with which motion can be detected. Kleinemeier [37], and Davis and Freeman [38] have shown that the interpolation required to obtain the shifted version of the template image causes systematic errors when noise is present in the system. These errors are more or less sinusoidally varying over the displacement by less than a single pixel. Under extreme circumstances, this can result in systematic position determination errors up to a significant portion of a single image pixel. Although the use of proper light conditions and sophisticated detection algorithms can mitigate the effect to a large extent, the error is always there at some level.

A technique reported by Yamahata *et al.* [39] uses Fourier analysis with great success. They extract the position of a feature from the phase of the discrete spatial Fourier transform of an image. When analyzing a time-series of images, typically a movie of a moving device, the movement of the feature can be tracked by observing how the phase-shift of the principal peak in the frequency spectrum changes. The technique works especially well with periodic features, multiple parallel beams for example. The resolution depends strongly on the number of feature periods and can become as precise as 0.2 nm (root-mean-square).

Burns and Helbig [40] use a clever approach for high-speed imaging. They describe a setup in which fast resonances of MEMS devices are tracked by investigating how much motion-related blur would appear when an image is taken with a long acquisition period compared to the period of the motion, which they call the 'blur-synthesis technique'. The amount of motion-induced blur is investigated by adjusting a reference image of the same device at rest by calculating what it would look like if a certain amount of motion-induced blurring would take place. By comparing these artificial images with the measured images containing motion-induced blur using χ^2-minimization, they are able to extract very precise resonance curves using a relatively standard microscopy system.

A technique that was recently reported, which is capable of reaching a very high resolution (< 1.8 nm), is based on a MEMS-based movable grating that rotates due to the motion of linearly moving comb drives [41] of which the motion is to be determined. The direction

of the reflection of a laser which is incident on the grating changes with the rotation, which allows a type of detection that is quite similar to the detection of out-of-plane cantilever motion in AFM systems. The laser light is incident on a photosensitive detector and changes in illumination can be very accurately monitored. Disadvantage of this technique is of course that it requires dedicated structures, and hence it cannot be used on most devices. Also, the detection is only indirect: the rotation of a dedicated structure is monitored instead of the primary linear motion.

We may conclude that there are many techniques available that provide a better in-plane displacement resolution than the optical diffraction limit. However, many of these techniques are limited by periodic errors, cannot be used for measurements of 'jerky' motions, or require the integration of complicated mechanical structures. Yamahata *et al.* [39] reports the lowest position noise so far using Fourier analysis. Can we do better?

The technique that we report on in the current chapter is based on fitting a mathematical model of the intensity variations of the image to detect motion between images. Pioneered for imaging by Hachicha and Simon [42], this is a very powerful technique that, to our knowledge, has never been applied to MEMS device monitoring. It is similar to the way the position of a peak is found in a spectrogram, for example to detect shifts in the Raman spectrum of mono-crystalline silicon under the influence of mechanical stress [43].

2.2. METHOD AND THEORY

We will explain our technique using the comb drive based nano battering ram [44] shown in figure 2.1a. For our purposes here, the intended function of the device (measuring adhesion) is not important. We could have used any linear MEMS actuator.

The inset of figure 2.1a shows a close-up of the ram, the counter-surface and the anchor point for one of the springs. An even smaller area with just two sections of the support springs is to the right. The left beam is a small section of the support spring close to the ram and the right beam is a section of the support spring close to the anchor. When the ram moves, the left beam will move with it, but the right beam remains stationary.

The pixel intensities of each image line plotted against the pixel x-position will show a similar 'intensity profile' with two distinct peaks of which the positions corresponds to the positions of the two beams. When the intensity profiles of all lines are summed, a much smoother curve is obtained, as is shown in figure 2.1b. If we manage to find a mathematical function that roughly matches the shape of a peak, we can apply a curve-fitting algorithm to find the value of the parameter that describes its center position. This technique is routinely used in many kinds of spectroscopy. A thorough investigation into the uncertainty of extracted peak position has recently been conducted by van Spengen [45] and we will use his theory here to investigate which parameters influence the measurement precision.

There are several ways to choose an appropriate fit-function to match the shape of the intensity profile. One way is to mathematically 'design' an algebraic function that resembles the intensity profile. The function should have a parameter x_0 that determines

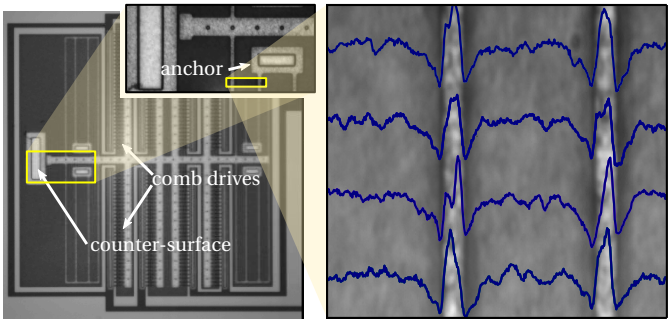

(a)

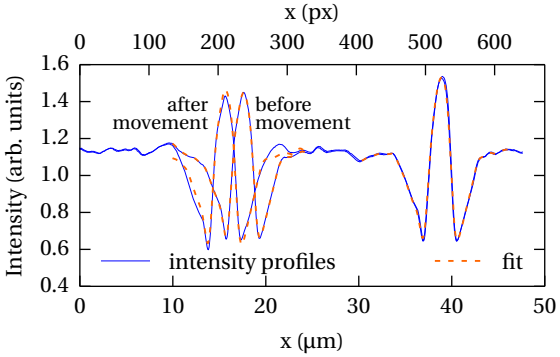

(b)

Figure 2.1.: Illustration of the curve fitting procedure for detecting sub-pixel displacements. Figure 2.1a shows a 'nano ram' MEMS adhesion sensor [44]. The ram can be moved by a comb drive actuator until it makes contact with a counter-surface. To measure displacement of the ram, a small region of interest is selected that shows two beams of which one remains stationary and one shows the same movement as the ram. Each horizontal line of pixels shows a similar intensity profile of which four are plotted as an overlay. Figure 2.1b shows the intensity profile that results from vertically summing over all the pixels of the region of interest before and after the left beam has been displaced by about 27 pixels. By fitting a function with a center position parameter, $f(x, x_0)$ to both the left and right peak separately, the position 'x_d' of the left beam with respect to the right beam is found using $d = x_{0,\text{left}} - x_{0,\text{right}}$.

its horizontal shift. The advantage of this method is that it is impossible to accidentally incorporate some of the noise in the fit function. The disadvantage is that a specific function is required for every different type of intensity profile.

A more practical approach is to extract the function from the intensity profile itself by creating an algebraic representation of it in the form of a spline interpolation function $s(x)$. Splines can be created automatically from any array of data by most data-analysis programs. This technique has the disadvantage that all the noise on the profile is also incorporated in the spline function which introduces periodic errors [38]. It should therefore be smoothed or filtered to get rid of the noise. The spline can then be used as a fit function by modifying it with a shift-parameter x_0 and optionally a variable amplitude A and offset y_0 as shown in equation (2.1).

$$f(x) = A \cdot s(x - x_0) + y_0 \tag{2.1}$$

Parameters A and y_0 are not essential, but can help the fit algorithm converge more easily if the amplitude of the intensity profile varies somewhat due to light source intensity fluctuations because of focal drift during a long measurement.

2.2.1. UNCERTAINTY ANALYSIS

The uncertainty of the fitted parameter x_0 is determined by the amount of noise on the intensity profile and the number of pixels that the 'moving part' of the intensity profile is spread across [43, 45].

The camera pixel noise has four components: electronic read noise, quantization noise, dark current, and photon shot noise. Read noise originates in the electronic read-out circuitry of the image sensor. Dark current refers to the current of electrons that are spontaneously freed, without a photon actually hitting the sensor. The amount of dark-current electrons per second depends exponentially on the sensor temperature. In applications that involve very long exposure times or little light, such as Raman spectroscopy and astronomy, the dark current typically dominates the noise figure, which is why CCD sensors used in Raman spectroscopes and large telescopes are often cooled with liquid nitrogen. In bright field microscopy the read noise and dark current are usually orders of magnitude lower than quantization noise and shot noise so we will further disregard them in this chapter for the sake of brevity.

SHOT NOISE

Photon shot noise is caused by the fact that for a constant light intensity, the number of photons that are detected within a certain exposure time will vary. This is a fundamental property of light itself and has nothing to do with the architecture of the camera or the light

source. Shot noise can be described as a Poisson process with parameter $\lambda = N_{\text{photons,px}}$. The signal to shot-noise ratio is given in equation (2.2),

$$SNR_{\text{shot}} = \frac{N_{\text{photons,px}}}{\sqrt{N_{\text{photons,px}}}} = \sqrt{N_{\text{photons,px}}} \tag{2.2}$$

where '$N_{\text{photons,px}}$' is the number of detected photons. The only way to increase it, is to maximize the amount of light that is captured by the sensor. The lower limit of shot noise is then determined by the number of photons that a pixel can detect before it saturates: the full-well-depth (FWD). The full-well-depth is usually expressed as the maximum number of electrons that can be stored on a pixel capacitor.

Important to remember is that the shot noise is related directly and exclusively to the pixel intensity, but in a slightly counter intuitive way: more photons means more shot noise. However, because the noise is equal to the square-root of the amount of photons, the net effect is positive and the signal-to-noise ratio increases for a higher number of photons. Equivalently, the relative uncertainty of a pixel value due to shot noise decreases.

QUANTIZATION NOISE

Quantization noise originates from the limited amount of digitization levels available for digitizing a pixel intensity. Most CMOS and CCD cameras have an analog-to-digital converter (ADC) with a bit-depth of 8,12 or 16 bits, yielding 256, 4096 or 65 536 quantization levels. The quantization error ϵ_q has a uniform probability density function within each quantization step: $p(e_q) = 1/q$ for $-q/2 < \epsilon_q < q/2$. Where $q = I_{\text{FWD}}/(2^N_{\text{bits}} - 1)$. The root-mean-square error can be calculated by integrating the probability density times the error squared:

$$e_{\text{rms}} = \sqrt{\int_{-\infty}^{\infty} p(\epsilon_q) {\epsilon_q}^2} = \frac{q}{\sqrt{12}} = \frac{I_{\text{FWD}}}{\sqrt{12} \cdot (2^N_{\text{bits}} - 1)}, \tag{2.3}$$

and the signal to quantization noise ratio 'SNR_q' becomes:

$$SNR_q = \frac{I_{\text{px}}}{e_{\text{rms}}} = \frac{I_{\text{px}}}{I_{\text{FWD}}} \cdot \sqrt{12} \cdot \left(2^{N_{\text{bits}}} - 1\right) \tag{2.4}$$

Where I_{px} is the pixel intensity, I_{FWD} is the full-well-depth and N_{bits} is the number of digitization bits.

TOTAL PIXEL NOISE

The relative contributions of shot noise and quantization noise are shown in figure 2.2. The pixel intensity is expressed as a percentage of the full-well-depth, which is a fixed number for a given camera that may vary a little per pixel. It can only be increased by buying a different camera or by adding the analog values of a number of adjacent pixels before they are digitized by the camera ADC. Figure 2.2 shows that for cameras with a full-well-depth of around a thousand electrons, the error is always determined by the

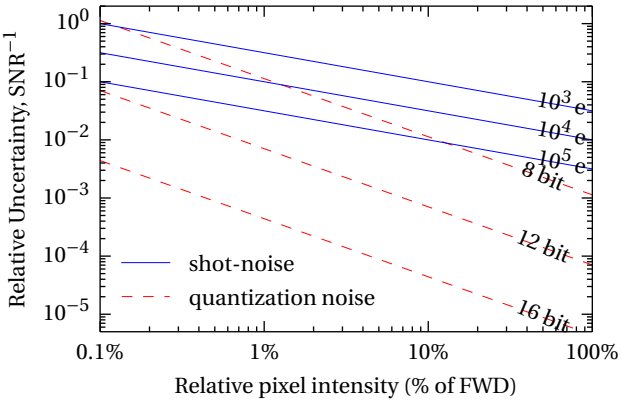

Figure 2.2.: The noise-to-signal ratio per pixel due to shot noise and quantization noise versus the relative pixel intensity $\frac{I_{px}}{I_{FWD}}$. The quantization noise is shown for sensors with 8, 12 and 16 bits AD-converters. The shot-noise is drawn for sensors with a full-well depth of 1000, 10 000 and 100 000 electrons.

shot noise. The bit-depth of the ADC can become an issue when pixel values are 'binned' before quantization. Binning an amount of N_{px} pixels effectively increases the full-well-depth by a factor N_{px} and consequently increases the signal-to-shot noise ratio by a factor $\sqrt{N_{px}}$, making the quantization noise the dominant source of noise.

IMAGE CONTRAST

Thus far we have dealt with the noise of a single pixel, but to understand the contribution of image contrast to the eventual position detection noise we need to consider the intensity profile as a whole. Because we are fitting a parameter that corresponds to horizontal shift, the curve fit accuracy is not influenced by the addition of a constant offset to the intensity profile. This means that the presence of a non-zero background does not add anything to the position noise directly. However, because the maximum value that any pixel can have is physically limited to the full-well-depth of the image sensor, having a non-zero background effectively reduces the amount of pixel values available for the peak and reduces the signal-to-noise ratio.

In addition, any non-zero pixel automatically contains shot noise (see equation (2.2)), so the brighter the background, the more noise it contains. Because having a lighter background automatically means having less contrast (because of the upper limit of determined by the FWD), the peak will drown in the shot noise of the background pixels. The dominant source of noise is now still shot noise, but it originates from the background, not from the signal.

We have modeled the effect of having a brighter background and smaller contrast by

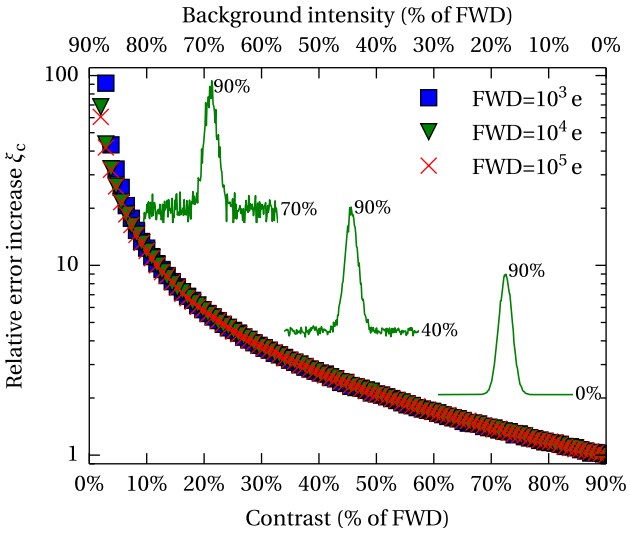

Figure 2.3.: The relative increase in the position error that results from the curve fitting algorithm due to limited contrast. Generated using a Monte Carlo simulation with $N_{MC} = 10000$. The maximum value of the peak was kept at 90 $\%_{FWD}$ while the background intensity was varied.

doing a Monte Carlo simulation of a simple Gaussian peak with an offset and simulated shot noise. The maximum peak value was kept at 90 $\%_{FWD}$ while the background intensity was varied from 0 $\%_{FWD}$ to 90 $\%_{FWD}$ for three different values of the full-well-depth. For each combination of parameters we simulated 1000 realizations of the Gaussian intensity profile and performed a curve fit to obtain an estimate for the center of the peak.

Figure 2.3 shows the relative error increase due to limited contrast ξ (c) against the contrast expressed in $\%_{FWD}$. To obtain the curve, the standard deviation of the peak position parameters of the 10 000 realizations of the Gaussian intensity profile were normalized to the lowest value, which was obtained for a background intensity of 0 $\%_{FWD}$ and a corresponding contrast of 90 $\%_{FWD}$. When the background intensity approaches 90 $\%_{FWD}$, the contrast goes to 0 $\%_{FWD}$ and the fit error goes to infinity. The graph clearly shows that the relative error increase due to the presence of a non-zero background is independent of the absolute value of the full-well-depth.

In a real measurement the contrast will be determined mainly by the material and surface texture of the sample that is being imaged, and of the quality and focus of the optics that are used. If the peak is out of focus or if the optics are not diffraction limited, a smaller contrast will result.

RESOLUTION AND PIXEL BINNING

The uncertainty of the position parameter x_0 that is found with the curve fit procedure also depends on the resolution of the camera. Or more precisely, on the amount of pixels the 'beam'-part of the intensity profile is spread across.

Binning a number of N_{px} adjacent pixels has the combined effect of lowering the effective resolution and raising the effective intensity per pixel which increases the signal-to-shot noise ratio SNR_{shot}. van Spengen and Roca [43] and van Spengen [45] have demonstrated that the negative effect of the decreased resolution is exactly compensated by the positive effect of the increase of the signal-to-shot noise ratio.

However, this theory is only true when we consider only a single line of pixels and we are binning the pixels horizontally. When binning pixels vertically, the resolution remains the same, but the signal intensity increases with the number of vertically binned pixels N_{lines} which increases the signal-to-shot noise ratio by a factor $\sqrt{N_{\text{lines}}}$. Vertical binning can sometimes be performed on the sensor chip itself, but it amounts to exactly the same thing as vertically summing over a number of lines after the image has been captured.

OPTICAL MAGNIFICATION

The knowledge that spreading the signal over a larger number of pixels does not affect the position uncertainty [45] has an interesting consequence for the amount of optical magnification required. Placing a magnifying lens in front of the camera or increasing the camera resolution (by choosing a different camera) will spread the signal over a larger number of pixels, but the total amount of light that is captured will remain the same. This lowers the average pixel intensity and consequently decreases the signal-to-shot noise ratio SNR_{shot}, which according to the theory is counteracted exactly by the positive effect of spreading the signal over a larger number of pixels. When acquisition speed is not an issue, the exposure time of the camera can be increased to increase the pixel intensity. This allows more light to reach the sensor and lowers the position uncertainty.

If the sample is illuminated through the microscope objective, an objective with a higher magnification will cause more light to be focused on the area of interest, which increases the signal-to-shot noise ratio SNR_{shot} and directly results in a lower position uncertainty. Again, this happens because more photons are captured from the interesting part of the intensity profile, not because it is spread across a larger number of pixels.

PERIODIC STRUCTURES

When the maximum amount of light possible for the optical assembly has been reached, the only way to further decrease the uncertainty of the fitted parameter is to spread the signal over more pixels by making the feature that is fitted wider, for example by looking at a periodic pattern of beams instead of just a single beam. This effectively increases the signal-to-shot noise ratio, in this case by increasing the amount of information in the signal. Fitting a single function through a pattern of beams will result in a shot noise

reduction of $\sqrt{\frac{1}{N_{\text{periods}}}}$, where N_{periods} is the number of beams, resulting in a proportionally lower position noise. This is exactly the same as fitting a function through each beam in the pattern, determining the position of each individual beam and averaging the results. Because the noise is statistically independent for each pixel, the uncertainty decreases with the square-root of the number of averaged values (standard error). This trend corresponds to the recommendation by Yamahata *et al.* [39] to use a large number of periodic structures to get a higher precision, when using the Fourier transform method mentioned earlier. The highest resolution found by Petitgrand and Bosseboeuf [36] was obtained on a high contrast sample with a highly textured surface. Translated to our technique, this would be equivalent to observing the collective motion of hundreds of narrow peaks simultaneously.

TOTAL POSITION ERROR

We can summarize the findings of this section with a rule-of-thumb: make sure that the noise per pixel is dominated by shot-noise. When that is the case, the position detection error σ_{pos} is given by equation (2.5).

$$\sigma_{\text{pos}} \sim \frac{1}{\sqrt{N_{\text{photons,px}}}} \cdot \frac{1}{\sqrt{N_{\text{lines}}}} \cdot \frac{1}{\sqrt{N_{\text{periods}}}} \cdot \xi\,(\text{c}) \tag{2.5}$$

Where '$N_{\text{photons,px}}$' is the average number of signal photons per pixel (i.e. the pixel intensity), 'N_{lines}' is the number of lines that are averaged or the vertical pixel binning amount, 'N_{periods}' is the number of periods of the pattern that is being imaged and $\xi\,(\text{c})$ is the effective error increase due to limited contrast (see figure 2.3).

2.3. EXPERIMENTS

To demonstrate the merits of the curve-fitting technique, we will show several measurements using three different MEMS actuators: the nano-ram adhesion sensor comb drive [44] shown in figure 2.1a that we used earlier in this chapter to explain the technique, a 'Leiden MEMS tribometer' [46] and a novel nitrogen-incorporated ultrananocrystalline diamond (N-UNCD) based adhesion sensor [47]. The intensity profiles of their beam springs look slightly different, but the devices are similar in design.

The devices are placed under a Motic PSM-1000 optical microscope with a Motic ULWD50x objective and an additional 2× magnifier lens, giving a total magnification of 100×. The sample is illuminated through the microscope objective with a Motic MLC150C halogen cold light source at its maximum intensity (> 120 000 lx). The images are taken with an Apogee Alta F4000 interline-scan CCD camera with an average pixel full-well depth of 31 000 electrons and a 16-bit analog-to-digital converter. This ensures the quantization noise can be neglected under all circumstances (see figure 2.2).

For all measurements the microscope is focused on a small area that shows a pair of support springs of which one moves with the translating part of the actuator and one

remains stationary with respect to the substrate. To eliminate any unintended motion of the camera with respect to the sample we will only consider the motion of the actuated beam with respect to the stationary beam. The displacement of the actuated beam is calculated by creating separate splines for the moving peak and the reference peak and fitting them for shift parameters x_{act} and x_{ref} respectively. The movement of the actuated beam with respect to the substrate $\hat{x}_{\text{act}}$ is then simply $\hat{x}_{\text{act}} = x_{\text{act}} - x_{\text{ref}}$. Experimental results of non-differential measurements and an in-depth review of the influence of mechanical noise can be found elsewhere [48].

We have measured the position of two silicon beam springs of the nano-ram adhesion sensor. The motion of the left beam spring is equal to the motion of the ram, while the position of the right spring remains stationary with respect to the substrate. The voltage on the comb drive that moves the ram forward is increased from 0 V to 60 V and back to 0 V in 2000 steps. The distance between consecutive voltage steps is decreased quadratically with increasing voltage to compensate for the characteristic quadratic voltage-displacement relation of the comb-drive actuator. The measured intensity profiles are summed over $N_{\text{lines}} = 367$ lines.

It is important to stress that the voltage is not swept in a continuous fashion, but in discrete steps. Each measurement point is obtained by sequentially setting the voltage, acquiring the image by exposing the sensor, and storing the intensity profile. The exposure time is 152 ms. Because the camera has a relatively slow data transfer rate, the time between set-acquire-store sequences is around 0.5 s.

In order to investigate what the position resolution of the curve-fitting technique is, we took a measurement of two stationary beams. Again, one is the 'moving' beam (even though in this case it is stationary) and the other is the reference beam. We measured the position of the moving beam with respect to the reference beam 200 times, for different values of N_{lines}. We executed this measurement using the 'Leiden MEMS tribometer' and the N-UNCD based adhesion sensor. The Leiden MEMS tribometer shows a better optical contrast than the nano-ram adhesion sensor that we used for the adhesion measurement. Compared to the silicon devices, the N-UNCD adhesion sensor's contrast is worse because the diamond device layer is slightly transparent.

DISCRIMINATION OF MECHANICAL NOISE

Because we do a differential position measurement using a stationary MEMS beam as an on-chip reference, low frequency mechanical vibrations of the sample with respect to the microscope will be rejected. The resonance frequencies of our MEMS structures (a few kilohertz) are orders of magnitude higher than the acquisition frame-rate (about 2 frames per second), so high frequency mechanical disturbances will 'average out' and translate to motion blur. To prevent this, the entire camera-microscope-sample assembly is suspended in bungee-cords inside an acoustic isolation booth on top of an active vibration isolated table. However, experiments carried out without any of these vibration isolation measures have shown that the influence of motion blur is not noticeable [48] and that our vibration isolation measures are not vital for a precise position measurement.

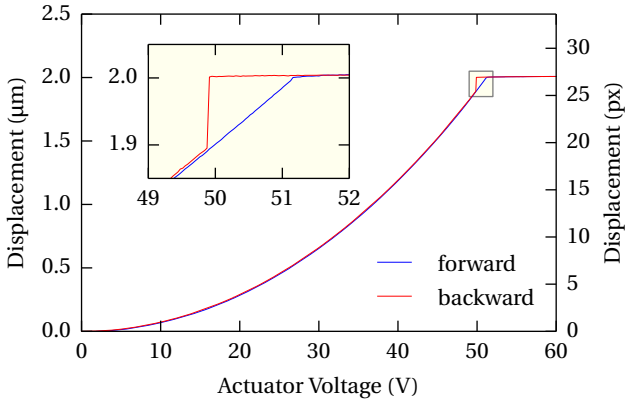

Figure 2.4.: Displacement of the ram towards the counter-surface and back to its initial position in the nano-ram adhesion sensor. At 51.2 V the ram touches the counter surface and stops moving. When the voltage is decreased, the ram adheres to the surface until it snaps off at 49.9 V and makes a jump of 106.2 nm ± 0.3 nm.

2.4. RESULTS AND DISCUSSION

2.4.1. ADHESION MEASUREMENT

The results of the adhesion sensor measurements are shown in figure 2.4. They show that the ram moves quadratically with the applied comb drive voltage until it touches the counter surface at 51.2 V. From lithography we know that the total gap between the ram and the counter surface is 2 µm. The ram displacement at the touching point is 26.9 pixels, so the amount of nanometers per pixel is 74.4 nm/pixel.

When the voltage is decreased, it shows that at the point where the ram touched the counter surface during the forward motion, it now sticks to the counter surface until the voltage is decreased further down to 49.9 V, where the ram suddenly snaps-off, and displaces by 106.2 nm. We estimated the position noise of the measurement by fitting a 12^{th} order polynomial trend line through the displacement graph between 10 V to 45 V and subtracting it from the measurement. The high order of the polynomial was necessary to correct for thermal effects and comb drive levitation that cause the voltage-displacement relationship of the comb drive to deviate slightly from the ideal quadratic curve. The resulting position noise distribution is shown in figure 2.5. We calculated the standard deviation of the noise to be $\sigma_{\text{pos}} = 0.27\,\text{nm}$.

2.4.2. DISPLACEMENT NOISE MEASUREMENTS

Figure 2.6 shows the standard deviation of the position noise versus the number of averaged lines for the different devices. The standard deviation of the position noise

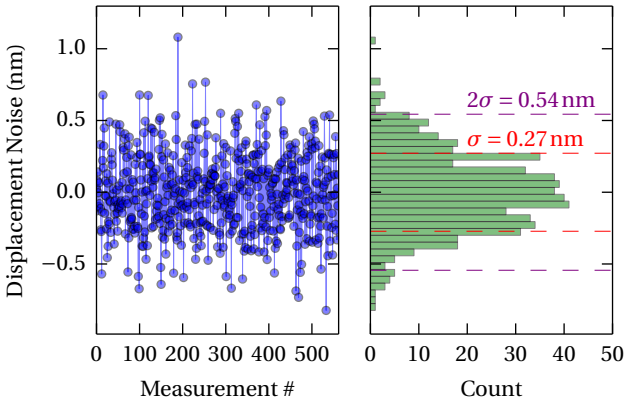

Figure 2.5.: The position noise of the nano-ram adhesion sensor measurement shown in figure 2.4, calculated by subtracting a 12$^{\text{th}}$ order polynomial trend line from the parabolic part of the displacement curve. The standard deviation of the noise is $\sigma_{\text{pos}} = 0.27\,\text{nm}$.

of the silicon tribometer for a single line is 2.51 nm and decreases with $\sqrt{\frac{1}{N_{\text{lines}}}}$ towards the lowest position noise we measured at $N_{\text{lines}} = 1577$, which is as low as 64 pm. The distribution of this measurement is shown in figure 2.7.

The standard deviation of the position noise of 0.27 nm that we calculated for the adhesion measurement (figure 2.5) is shown as a single point in figure 2.6 and lies well above the trendline of the Leiden MEMS tribometer. The position uncertainty of the measurements taken with the N-UNCD adhesion sensors follows the same $\sqrt{\frac{1}{N_{\text{lines}}}}$ trend as the silicon tribometer, but has a larger error for the same amount of summed lines. Both these results are in accordance with the observation that the intensity profiles of the diamond device and the nano-ram adhesion sensor have a worse optical contrast than the silicon tribometer.

2.5. CONCLUSION

We have achieved an in-plane displacement resolution of 64 pm by fitting a shifted spline function through the intensity profile of a silicon beam that was imaged with an optical microscope and a CCD camera. The resolution depends strongly on the signal-to-noise ratio of the image. The noise figure is dominated by photon shot noise which is the limiting factor for the precision of the measurement. The effect of photon shot noise can be decreased by increasing the intensity of the light source, increasing the contrast, averaging or binning multiple lines, or by using a camera with a larger full-well-depth.

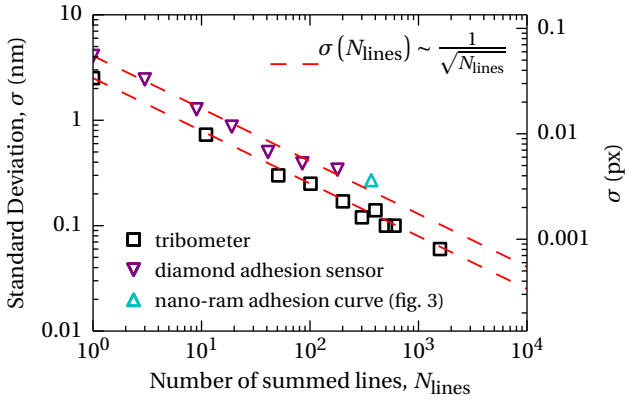

Figure 2.6.: Displacement error versus the number of summed lines (i.e. vertically binned pixels). The error decreases with a factor $\sqrt{\frac{1}{N_{\text{lines}}}}$.

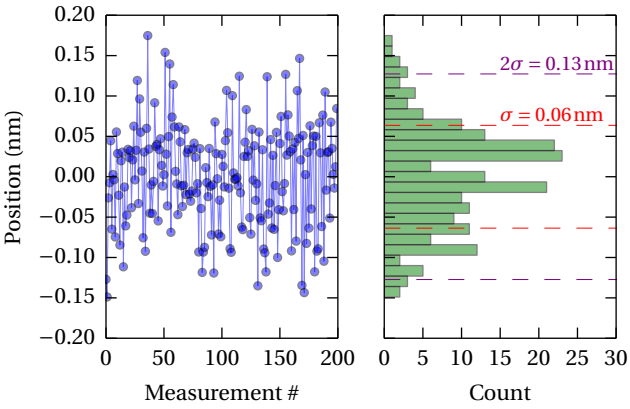

Figure 2.7.: Position noise measurement of the Leiden MEMS tribometer. The measured differential displacement of a stationary pair of silicon beams with $N_{\text{lines}} = 1577$ and a histogram that shows the distribution of the measured values in 25 bins. The standard deviation of the noise is $\sigma_{\text{pos}} = 64\,\text{pm}$.

Compared to other optical in-plane displacement detection techniques, the curve fitting method presented in this chapter offers the highest position resolution, although it was obtained using a large number of averaged image lines. It can be used to measure instantaneous 'jerky' motions of MEMS structures, something that is hard to accomplish with techniques that rely on spatio-temporal filtering. We have released our curve fitting procedure as an open source Python module [49] under the terms of the GNU General Public License. Images can be captured with any digital camera that fits onto a microscope, making this technique available to practically any laboratory.

3

REAL-TIME OPTICAL MEASUREMENTS AT HIGH SPEED

In chapter 2 we presented an optical technique for measuring displacements in MEMS devices. It enabled us to measure the voltage–displacement curve of a MEMS adhesion sensor with sub-nanometer resolution. However, the camera used in the experiment was not fast enough to capture the dynamics of the device. In this chapter, we replace the 2D image sensor used before by a 300 000 frames/s line-scan camera. The amount of light available for this measurement, and the raw resolution of the captured images are significantly lower than in our earlier measurements, which allows us to evaluate how our measurement technique performs under suboptimal conditions. We show the displacement of a MEMS tribometer as a function of time, and expose the dynamics of its adhesive contact.

3.1. INTRODUCTION

We have previously obtained excellent results with an optical technique with sub-nanometer resolutions (chapter 2). However, our measurements were nowhere near fast enough to capture transient phenomena as a function of time. Although we measured adhesion snap-in and snap-off, we have never actually observed the motions themselves: we only observed the loader being stuck to the slider. If, at some point, we find the moving part of our tribometer to be at A, and the next time we look for it, we find it at B, common sense dictates that it moved from A to B in the time between our observations, but we have no clue what this motion actually looks like. We do not know whether it is under-damped, over-damped, or completely non-linear.

A conventional and accurate technique for measuring fast displacements in MEMS as a function of time is laser doppler vibrometry. Although this technique is mostly used for out-of-plane displacement measurement, Polytec now also offers the MSA-100-3D, which is able to determine motions in three dimensions, with picometer accuracy[50]. However, laser doppler vibrometry is not well suited from tracking low-frequency displacements with a high resolution; it can only measure moving components because it relies on the optical doppler effect for its operation. It is therefore impossible to measure the displacement of quasi-stationary components this way.

Recently, Shroff and de Boer [51] have pioneered similar displacement detection technique as we have: displacements are calculated from a sequence of captured microscopic images by fitting a sinusoidal waveform to a grating feature on their MEMS device. They used a 2D high-speed camera to measure transient responses of stick–slip friction in MEMS, which yields an impressive in-plane resolution of ~2 nm at 200 000 fps. However, this requires the use of an expensive 2D high-speed camera in a similar price range as a laser doppler vibrometer.

In this chapter we will use a high-speed line-scan camera (which is relatively low-cost, compared to the camera used by Shroff and de Boer) to measure the contact bounce and snap-off step response of a MEMS tribometer, and investigate the merits of our curve-fitting technique when applied to ultra-high frame-rate microscopy.

3.2. EXPERIMENTS

The experiments in this chapter were carried out using a MEMS tribometer similar to the ones used for the adhesion and friction experiments described in chapters 4 to 6 (see figure 4.1). It consists of a ram that can be pushed against the sidewall of a slider by an electrostatic comb drive actuator array. The slider that can be moved as well in order be able to perform friction measurements. For the experiments in this chapter the slider actuators were not used. Electrical connections to the device we made using probes.

The actuator voltages were applied to the comb-drives of the adhesion sensor by the analog output of a National Instruments NI USB-6351 DAQ via a FLC Electronics A400 20× voltage amplifier. The DA-converter of the DAQ was operated using its internal hardware clock at an output sampling frequency of 1 MHz with 16 bit precision over

a scale of –1 V to 10 V. This gives a voltage step of 168 µV. The output voltage of the amplifier was monitored (but not recorded) using an Agilent 34405A digital multimeter. The negative lower limit of the NI-DAQ was necessary to allow for compensation of the offset of the amplifier, which was between 0.5 V to 1.0 V. The actuator comb-drives of the slider where kept at 0 V to prevent electrostatic forces between the ram and the counter surface.

In all experiments, the motion of the ram was recorded using a Motic PSM-1000 optical microscope and a Basler Sprint SPL2048-140km line-scan camera. The microscope was fitted with a ×20 long working distance objective. The sample under test was illuminated through the microscope objective by a Sutter HPX ultra bright white LED light source and a liquid light guide. The line-scan camera was operated in free run mode, at 165 klines/s. The clock of the NI-DAQ was not synchronized with the high-speed camera. Both the NI-DAQ and the line-scan camera were controlled from python. The acquired image data was saved to HDF5 files.

The sample was positioned such that both a moving beam and stationary beam were imaged by the line scan camera. From each individual captured line, the relative displacement of the moving beam was determined relative to the stationary beam using the curve-fit procedure described in chapter 2.

Two adhesion experiments were carried out using the setup described above:

1. A single, slow adhesion cycle, similar to the adhesion experiment shown in chapters 2 and 4
2. Repeated contact bounce–adhesion snap-off

The single, slow adhesion cycle was measured by performing a single slow voltage sweep from 0 V to 85 V and back to 0 V. The DAQ output voltage was updated directly by a running python script, so the timing of the steps was not accurately defined. This was done to approximate the workings of the LabVIEW software used in our previous works on MEMS adhesion measurements [52–54], in which the timing of the samples was also controlled by software.

For the repeated contact bounce–adhesion measurements, the ram was actuated with 100 cycles of an inverse sawtooth wave between 76 V and 85 V at 10 Hz (see figure 3.1). The steep part of the sawtooth wave causes the ram to smash into the counter surface, which causes contact bounce. The linear part of the sawtooth wave slowly pulls it back, causing it to snap off from the counter surface. The waveform was generated using the internal clock of the DAQ at a sample frequency of 1 MHz.

3.2.1. ENVIRONMENTAL CONDITIONS

The entire setup was placed inside an acoustically isolated Faraday cage on passive pneumatic supports, ensuring a basic mechanical and electrical decoupling from the environment. The measurement setup used here is very similar to the setup used for the experiments used in chapters 2, 4 and 6, although it offers only basic vibration damping, it

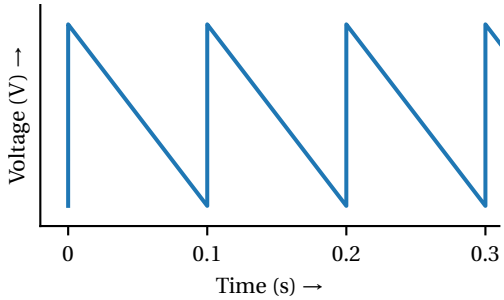

Figure 3.1.: Inverted sawtooth waveform.

did not have built-in temperature and humidity sensors, and the microscope's objectives where slightly dirty and out of alignment.[1].

The environmental conditions of the laboratory were kept constant at a temperature of 21 °C and a relative humidity of 53 $\%_{RH}$. However, during the experiments, the temperature inside the probestation was considerably higher than the controlled atmosphere of the laboratory due to the heat produced by the high-speed camera. The temperature of the camera heat sink was roughly 50 °C (barely touchable), and we estimate that the temperature inside the probestation was 35 ± 5 °C. The saturation vapor pressure of water can be calculated using the Antoine equation[62]: $P_s|_{21\,°C} = 2.487$ kPa and $P_s|_{35\,°C} = 5.609$ kPa. The vapor pressure in the laboratory is therefore $P_v = 53\,\%_{RH} \cdot P_s|_{21\,°C} = 1.313$ kPa. Assuming the vapor pressure inside the probestation is the same before and after the atmosphere has been heated, the resulting relative humidity at 35 ± 5 °C is: $\frac{P_v}{P_s|_{35\,°C}} = 23 \pm 6\,\%_{RH}$.

The light-source has the equivalent light-output of a 150 W xenon arc lamp. This heats up the adhesion sensor and it's immediate surroundings, which results in a noticeable disturbance of the air between the sample and the objective.

3.3. RESULTS: A SINGLE SLOW ADHESION CYCLE

The time–displacement graph of the single slow adhesion cycle is shown in figure 3.2.

The amount of nanometers per pixel was calibrated from this measurement by assuming that the gap width between the ram and the counter-surface is 2 µm. The amount of nanometers per pixel was calculated by dividing this gap width by the difference between the position of the ram at $V_{act} = 0$, and the mean displacement while it is in contact with the counter-surface between 5 s to 6.5 s. The nanometer-to-pixel ratio was determined to be 376 nm/px

Figure 3.2 shows that the ram approaches the counter-surface at a constant speed, until it makes contact. No clear snap-in is visible. When the actuator voltage is decreased again, the ram sticks to the counter-surface until it suddenly snaps-off at $t = \sim 6.7$ s. The inset

[1] This setup has been used in many of our other publications (see [44, 47, 52, 53, 55–61].

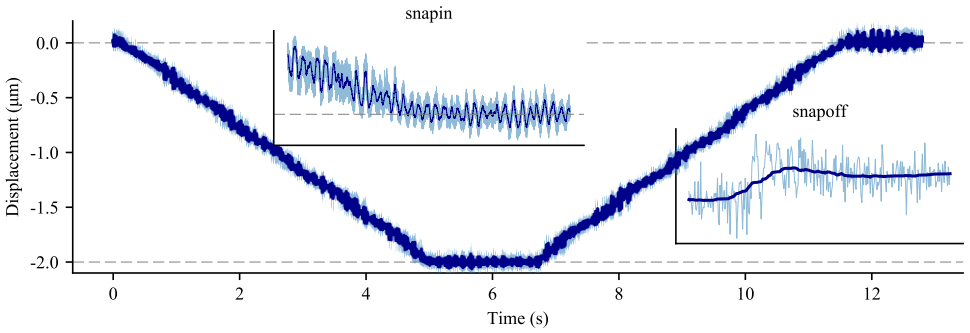

Figure 3.2.: A single, slow adhesion cycle. The displacement is measured optically at a sample rate of 165 kSamples/s.

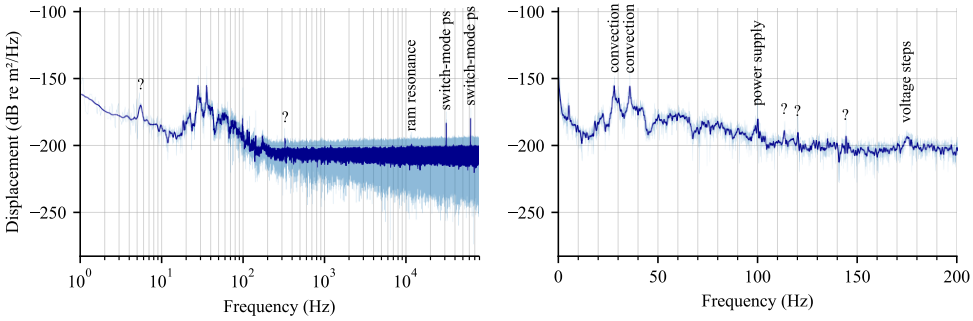

(a) (b)

Figure 3.3.: Frequency spectrum from the high-speed measurement of a single, slow adhesion cycle. The disturbance between 10 Hz and 100 Hz is caused by thermal fluctuations of the air between the microscope objective and the sample.

graph displays a closeup of the snap-off, which shows a brief oscillation. The snap-off length is 27 nm.

3.3.1. NOISE SPECTRUM ANALYSIS

Figure 3.3a shows the power spectral density of the measurement in dB using a logarithmic frequency axis. Figure 3.3b shows a closeup the lower part of the spectrum using a linear frequency axis. Several peaks are clearly in the spectrum. We have not managed to identify all of them, but we have explanations for a few, they are summarized in table 3.1.

The peak at 100 Hz is likely caused by electromagnetic disturbance from a rectified 100 Hz line signal. The physical source of this interference is most likely the cable that powers the line-scan camera, which carries a direct current of 0.5 A at 12 V, which is generated

by a non-switching transformer–rectifier. The broad peak between 170 Hz and 180 Hz matches the step rate of the actuator voltage. The broadness of the peak is explained by the fact that the actuation was not accurately timed by hardware, but was determined by the cycling rate of the python `for`-loop, used from which the voltage was written to the DAQ.

Table 3.1.: Summary of the identified peaks in the frequency spectrum shown in figure 3.3.

Frequency (Hz)	Origin
28.5	convection
36.1	convection
100.1	power supply
174.8	voltage steps
11 715.2	ram resonance
31 222.5	switch-mode power supply
62 488.9	switch-mode power supply

The small peak at 11.715 kHz is caused by resonance of the ram. The two high peaks at 31.222 kHz and 62.489 kHz are likely to be caused by switch mode power supplies in the vicinity of the measurement setup. These frequencies penetrate the cage of Faraday magnetically, or they may have bled from the USB cable that connects the National Instruments DAQ to the computer from which the experiment is controlled.

3.4. RESULTS: CONTACT BOUNCE AND SNAP-OFF

In this section we present the results of the high-speed displacement measurement and describe the methods we used to extract the contact bounce and snap-off dynamics from data. All data-analysis was done using jupyter notebook with an ipython backend. We relied heavily on the `pandas` library [63].

Figure 3.4 displays the measured displacement of the ram versus time, for the measurement in which the ram was actuated with a 10 Hz inverse sawtooth. Only two out of the total of one hundred waveform cycles are shown individually, because plotting all data does not result in an informative graph. Each measured cycle contains two events of interest: the contact bounce and the snap-off. The contact bounce event occurs after the actuator voltage is increased instantly from the offset value of 76 V to the sawtooth maximum of 85 V, and the ram smashes into the counter surface. The snap-off event occurs when the voltage is reduced, and the restoring spring force pulls the ram away from the counter-surface.

Although the contact bounce and snap-off responses are clearly visible in each individual cycle, the displacement noise is relatively high. In order to decrease the measurement noise we have to align all recorded events, and calculate their average.

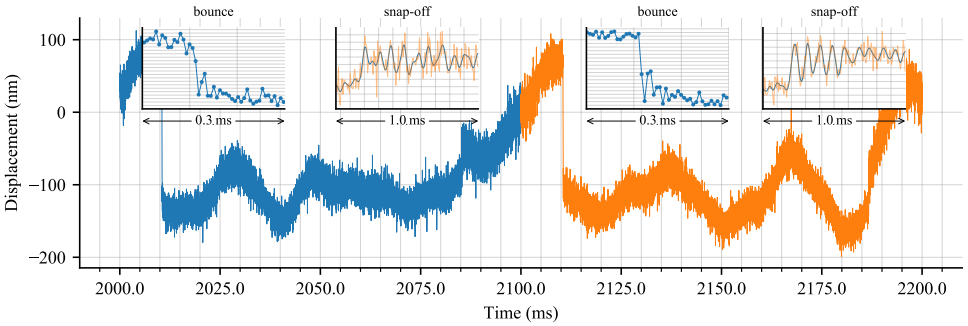

Figure 3.4.: The response of the ram when actuated with an inverse sawtooth wave. This Time–displacement plot shows two out of the total of 100 'smash-in/snap-off' cycles. The inset figures show closeup views of the moments when the ram makes or breaks contact with the counter surface.

Because we know that the sawtooth actuation frequency was exactly 10 Hz, the individual contact cycles can be isolated by simply splitting the measurement into sections of 100 ms. However, this does not mean that the contact bounce and snap-off responses are automatically aligned.

3.4.1. SNAP-OFF RESPONSE

By aligning all snap-off events, we can average the step responses. Because a single snap-off event occurs in every one of the 100 cycles, which reduces the displacement noise by a factor 10. The resulting average snap-off displacement is shown in figure 3.5. The decreasing ramp of the actuation waveform is clearly visible in figure 3.5a, as is the under-damped nature of the ram. A close-up of the underdamped response is shown in figure 3.5b, in which we corrected the displacement values for the ramp.

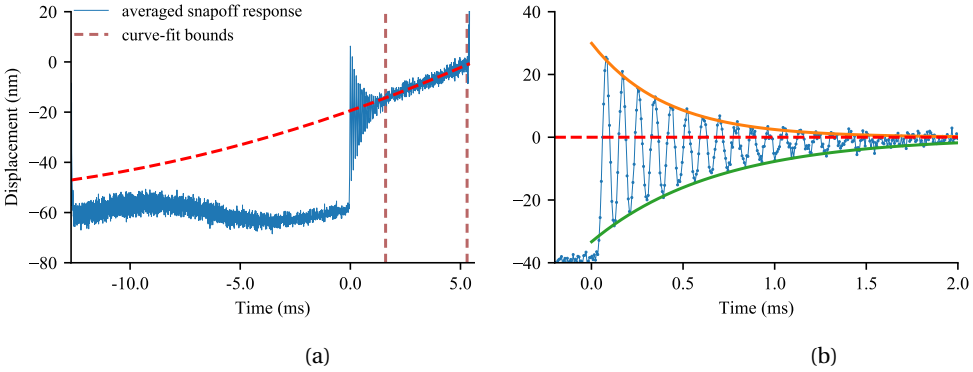

Figure 3.5.: Snap-off motion (100 inverse sawtooth cycle average).

Table 3.2.: The damping parameters of the underdamped adhesion snap-off response shown in figure 3.5b. The time constant τ was found by manually fitting $d = A \cdot e^{\frac{-t}{\tau}}$ to the upper and lower bounds of the underdamped snap-off motion. The damping ratio and the quality factor where determined from τ and f_{res} using equations (3.1) and (3.2).

	upper bound	lower bound
Amplitude, A	30	31
Time constant, τ (s)	700×10^{-6}	400×10^{-6}
Quality factor, Q	15	26
Damping ratio, ζ	34×10^{-3}	19×10^{-3}

The fundamental resonance frequency of the snap-off response was obtained from the Fourier transform of the averaged snap-off response, and was found to be $f_{res} = 11.7\,\text{kHz}$. This value matches the position of a small, narrow peak in the frequency spectrum of the single cycle displacement measurement shown in figure 3.3a.

DAMPING

We determined the characteristic time constant τ of the loader from the snap-off response, by manually fitting an exponential function of the form $d = A \cdot e^{\frac{-t}{\tau}}$ to the upper bound of snap-off resonance envelope. In order to fit the exponential functions to the envelope, we first corrected the displacement values for the ramp of the sawtooth by subtracting a second order polynomial from the displacement curve. The final value of the resonance now appears to decay to a constant displacement of zero. The damping ratio ζ can be calculated from τ and f_{res} using equation (3.1):

$$\zeta = \frac{1}{\sqrt{1 + (2\pi f_{res})^2 \cdot \tau^2}}. \tag{3.1}$$

The quality factor Q is related to the damping ratio by equation (3.2):

$$Q = \frac{1}{2\zeta} \tag{3.2}$$

Ideally, the upper and lower envelope bounds of the snap-off response should be exactly symmetrical around zero. However, the envelopes are slightly asymmetrical because of the low frequency drift clearly visible in figure 3.5a. The calculated values the damping parameters of both the upper and lower envelope bounds are given in table table 3.2.

3.4.2. CONTACT BOUNCE RESPONSE

The frequency of the contact bounce is much higher than the resonance frequency of the ram, because it is determined partly by the elasticity of the contact, which is much stiffer than the compliant supports of the ram. The bounce events displayed in the inset graphs in figure 3.4, show that only about 3 samples are available per bounce motion. This is because the bounce frequency is close to the line-scan rate of 165 klines/s. If we were to simply average all measured bounce responses, as we have done successfully with the snap-off responses, the displacement noise might decrease, but the amount of samples per bounce motion would still be too close to the Nyquist frequency to produce a clear signal. Moreover, because the exact time of impact varies slightly from cycle to cycle, the bounce responses all have a random sub-sample misalignment. Averaging all measured responses will reduce the signal intensity exactly as much as it reduces the noise.

However, we can use the random variations between the times at which the ram first makes contact with the counter-surface to our advantage by using a technique called temporal dithering.

Dithering in general is a technique used to increase the number of effective quantization levels of any analog-to-digital conversion process, by adding noise to the analog input signal, and averaging multiple digitized output signals. Dithering is usually applied to increase the number of quantization levels of an AD-converter. This is accomplished by adding white noise to the analog signal that is being quantized, such that a single input value will result in different digital values when it is sampled repeatedly. By oversampling and averaging N of these dithered samples, the quantization noise is reduced by a factor $\sqrt{N}$, but the sample frequency is reduced by a factor N. The amount of dithering that can be used is therefore determined by the highest input frequency that is to be captured by the AD-converter.

Instead of using dithering to increase the amount of voltage quantization levels, it can also be used to increase the effective sample frequency, in which case it is called temporal dithering.[2] Temporal dithering works by adding a random, known time-delay τ to a repeating input signal $x(t)$ of length T. For every i^{th} repetition of the input signal, the signal is delayed by a known time delay τ_i, with $\tau_i < \frac{1}{f_{\text{sample}}}$. After capturing N sample sequences of $x_i(t-\tau_i)$, the 'actual time' can be calculated for each sample, by shifting it by the corresponding time-delay τ_i. In our case, the signal $x_i(t)$ is the bounce response, which we have measured $N = 100$ times. We did not add a known sub-samplerate delay to each of them ourselves, but instead we used the random timing delays caused by the thermal motion of the ram. In order to apply temporal dithering to increase the effective sample frequency of the bounce response, we had to determine these time-delay values from the measurements before we can compensate for them.

[2] In order to increase the measurement bandwidth by temporal dithering, it is necessary that that the time used to acquire a single sample is shorter than the time between samples. This is not the case in our measurements, where the exposure time is equal to the time between samples. So although we increase the effective sample frequency to obtain a smoother signal, the maximum signal frequency that we can measure is still determined by the line scan frequency.

The most 'real' time point at which to align the bounce responses is the first point of contact. However, this point is relatively hard to find because it the real motion is hard to distinguish from the noise. A more convenient feature to identify is the relatively long approach curve, which we accomplish using the following procedure:

1. Filter all measured displacement data with a 4^{th}-order low-pass Butterworth filter with a cutoff frequency of 14 kHz.
2. Create a spline-based interpolation function $s_i(t)$ for each filtered bounce response x_i using scipy's `UnivariateSpline` class.
3. Find $t_{\text{offset},i}$, at which $s_i(t)$ has its steepest negative slope by solving $0 = \left.\frac{\mathrm{d}^2 s_i(t)}{\mathrm{d}t^2}\right|_{t=t_{\text{offset},i}}$ while $0 < \left.\frac{\mathrm{d}s_i(t)}{\mathrm{d}t}\right|_{t=t_{\text{offset},i}}$.

A single oversampled snap-in response was then obtained by combining all individual signals, and compensating their time values for the found offset values $\tau_{\text{offset},i}$. The oversampled signal can now be de-noised by applying a filter, or by calculating a rolling average.

Figure 3.6 shows the individual data points of the oversampled signal, as well as the de-noised contact bounce response, calculated from a 333 ns rolling average. Its shows that the ram bounces six times in ~100 µs before it settles, which corresponds to a bounce frequency of ~60 kHz.

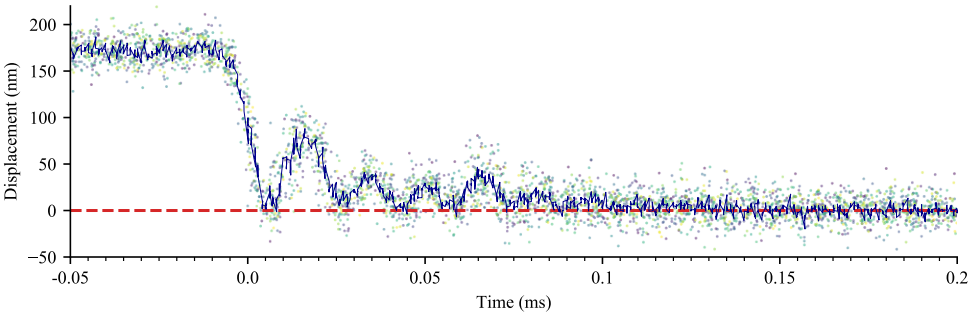

Figure 3.6.: Contact bounce motion of the ram against the counter-surface. The scattered data points are all of the 100 measured bounce motions that have been aligned at the steepest part of the approach curve with sub-sample resolution. The blue line represents a rolling median of the scattered data points using a 333 ns rectangular window.

3.5. DISCUSSION AND CONCLUSION

We have successfully measured the contact bounce and adhesion snap-off of two contacting silicon MEMS sidewalls in real-time, using a high speed line-scan camera, and

by using our displacement measurement technique to extract displacement from the captured optical line-scan images.

The total measurement noise was higher than the noise figure of just the optical measurement method, because of some 100 Hz power supply noise, and most importantly: low frequency thermal fluctuations of the air between the sample and the objective. However, these fluctuations have a much lower specific frequency than the dynamic phenomena under test necessitating the use of a high-speed camera and an ultra-bright light source in the first place. By applying a low-pass filter, the low frequency external disturbance can be filtered out safely.

3.5.1. NOISE FIGURE COMPARISONS

Because there always is a trade-off between high resolution and a high frame rate, it is useful to express the noise level of a measurement setup (including the properties of the sample) as a metric that is independent of the frame-rate. Our 64 pm measurements were acquired with an exposure time of 152 ms, or a frame rate of 3.3 Hz, which yields a noise figure of 35.3 pm/$\sqrt{\text{Hz}}$

In addition to these 'low-noise, much light' measurements, we also applied our measurement system to extract displacements from images obtained under less ideal circumstances, by a high-speed line-scan camera, at a high frame rate of 165 klines/s . After applying a band-bass filter to attenuate external noise sources, the effective RMS displacement noise of these high-speed measurements was 10 nm in a bandwidth of 1 kHz to 78 kHz, which corresponds to a noise figure of 36 pm/$\sqrt{\text{Hz}}$: very close to the noise figure of 35.3 pm/$\sqrt{\text{Hz}}$ of the low speed measurements. This proves once more that the shot noise of the light is responsible for the noise floor in these experiments.

Proof that it pays off to optimize the geometry of the detection of the MEMS device under test, can be found in an excellent paper by Shroff and de Boer [51]. They describe a high-speed friction measurement using a MEMS tribometer, in which the displacements are analyzed by fitting a sine wave function to intensity profile of grating instead of a single beam. The grating consists of 14 beams, which lowers the noise by a factor $\sqrt{14} \approx 3.7$. In addition, the grating beams are twice as wide and their edges appear to be much less rounded than the ones in our tribometer. If this increases their brightness roughly by a factor ~3, this further reduces the noise by at least a factor 2. Using our measurement setup, this would yield a total noise figure of 5.4 pm/$\sqrt{\text{Hz}}$. Indeed, Shroff and de Boer report an in-plane displacement resolution of ~2 nm at 200 000 Hz, which corresponds to an effective noise figure between 3.4 pm/$\sqrt{\text{Hz}}$ and 5.6 pm/$\sqrt{\text{Hz}}$.

3.5.2. CONTACT BOUNCE

We successfully measured the contact bounce motion of the ram, when it is smashed into the counter-surface. We observed 5 clear bounces at 50 kHz before the contact stabilized. The bounce frequency is very close to the Nyquist frequency of 78.122 kHz, which means that for each of the 100 captured bounce responses, only ~3 samples were captured per

bounce. Moreover, the exact moment of impact was not exactly synchronized between measurements, so simply averaging all captured responses did not yield a better displacement noise resolution. However, the presence of this random time-offset between cycles provided us with an opportunity to apply temporal dithering. By sub-sample aligning all measured bounce responses on the steepest part of the low-pass filtered approach curve, and calculating a rolling average with a constant-time window of 333 ns, we increased the effective sample frequency to 500 kHz, while reducing the effective displacement noise.

3.5.3. ADHESION SNAP-OFF

We successfully measured the underdamped motion of the ram when it is pulled off the counter surface. The resonance frequency of the ram was determined from the adhesion snap-off response and was found to have a value of $f_{\text{res}} = 11.715\,\text{kHz}$. At the 'lowest point' of the first oscillation of the snap-off response, the ram approached the counter surface to a distance of 10 nm. Any non-contact forces between the ram and the counter surface, like the van der Waals force, distort the harmonic oscillation, and might cause the lower bound of the envelope to have a longer characteristic time constant. However, in this data set, the low frequency noise component makes it impossible to determine whether or not there is an additional surface force acting on the loader during snap-off.

Monte Carlo simulations by van Spengen [17] show that the adhesion force is not dominated by capillary condensation when the relative humidity of the air is below 40 %, and the roughness of the contacting surfaces is above 10 nm. The roughness of the sidewalls of our tribometer is 13 ± 3 nm (see table 6.1 and [64]) and the relative humidity inside the probestation is between $24 \pm 7\,\%_{\text{RH}}$, which means that our device performed just as the theory predicts.

It would be of great value to repeat the experiments presented in this chapter under carefully monitored atmospheric conditions. By placing the device under test in an atmospheric chamber as was used in chapters 2, 4 and 6, and by using a MEMS tribometer with *in situ* heated contacting surfaces, it would be possible to measure the dynamics of the strange capillary effects that cause the erratic variability of the adhesion and friction forces described by Gkouzou *et al.* [53, 65].

II

ADHESION AND FRICTION IN MEMS

4

THE RUN-IN AND DRIFT OF ADHESION IN SILICON MEMS

In the previous chapters we developed a technique to measure forces and displacements with sub-nanometer and sub-nanonewton resolution (chapter 2). We now apply this knowledge to characterize the evolution of the adhesion force between two silicon surfaces that are repeatedly brought into contact.

This chapter shows the results of an empirical study in which we investigated the run-in behavior of several nominally identical copies of a MEMS adhesion sensor. The devices were tested under similar conditions with slight variations in contact force and relative humidity. However, we will see that, due to device-to-device surface variability, the run-in behavior observed differs significantly from device to device.

This chapter has been accepted for publication as a standalone journal paper [66]. Some editorial changes where added for inclusion in this thesis.

4.1. INTRODUCTION

The contact mechanics of MEMS is a topic of increasing interest. For the major a part of the MEMS devices currently on the market, contact mechanics plays no role, simply because the devices are designed such that no moving components are required to touch each other. However, even in these devices some parts may occasionally come into contact when they are subjected to impact accelerations. For devices like MEMS switches, latches and mirrors, where components are required to come into contact, the study of contact mechanics and in particular the study of adhesion is of primary importance.

The phenomenon of adhesion has been understood and mitigated quite well on the macroscale for a long time and significant advances have been made on atomic scale adhesion [67]. However, our understanding of so-called 'mesoscale' contact mechanics: the domain where the number of contact points, or asperities between two contacting surfaces is larger than one (atomic scale) but not 'close to infinity' (macroscale), is lagging behind.

Much progress has been made in the development of anti-stiction coatings [68] and novel methods of lubrication have been discovered [69]. We believe that an important reason why MEMS devices with contacting surfaces are still under-represented, is the lack of fundamental knowledge about what actually goes on at the interface of a mesoscale multi-asperity contact.

The reason for this knowledge gap is threefold. First, it is relatively difficult to create a physical model of a realistic mesoscale multi-asperity contact. This is because the working distances of the mechanisms involved in generating the forces between the contacts, are of the same order of magnitude as the roughness of the contacting surfaces. The behavior of contacting surfaces with exactly the same roughness statistics can differ by orders of magnitude, simply because at the actual contact points, the surfaces are physically different [17, 70].

Second, due to the stochastic nature of mesoscale contact mechanics, highly variable results are found under otherwise equal circumstances, which makes it hard to execute repeatable experiments. In addition, most real MEMS surfaces contain a number of unknown contaminants that will influence the result.

Third, although mesoscale contact forces are large compared to the other forces in a typical microsystem, they are still very small in an absolute sense, and are therefore hard to measure with sufficient precision. Until very recently, AFMs were the only instruments capable of measuring such tiny forces [67], and direct measurements of contact forces in MEMS devices typically suffered from a low signal to noise ratio [22].

However, our new optical technique based on curve fitting allows displacement measurements with deep sub-nanometer resolution (see chapter 2). The merits of the technique have already been demonstrated by measuring adhesion forces in MEMS devices made entirely out of diamond [52]. We have also previously presented a single adhesion experiment on silicon MEMS [54], in which we observed surprising run-in behavior of the adhesion force between two sidewalls that were repeatedly brought into contact.

4.2. THEORY: HOW TO DETERMINE THE ADHESION FORCE FROM DISPLACEMENT

Figure 4.1 shows a scanning electron microscope (SEM) micrograph of the type of MEMS adhesion sensor that we have used in this chapter. The device consist of a 'battering ram' that is suspended by folded-flexure support springs, and can be moved forwards and backwards by comb-drive actuators. When the ram moves forward by 2 µm, it makes contact with a 'counter-surface' to which it will temporarily adhere.

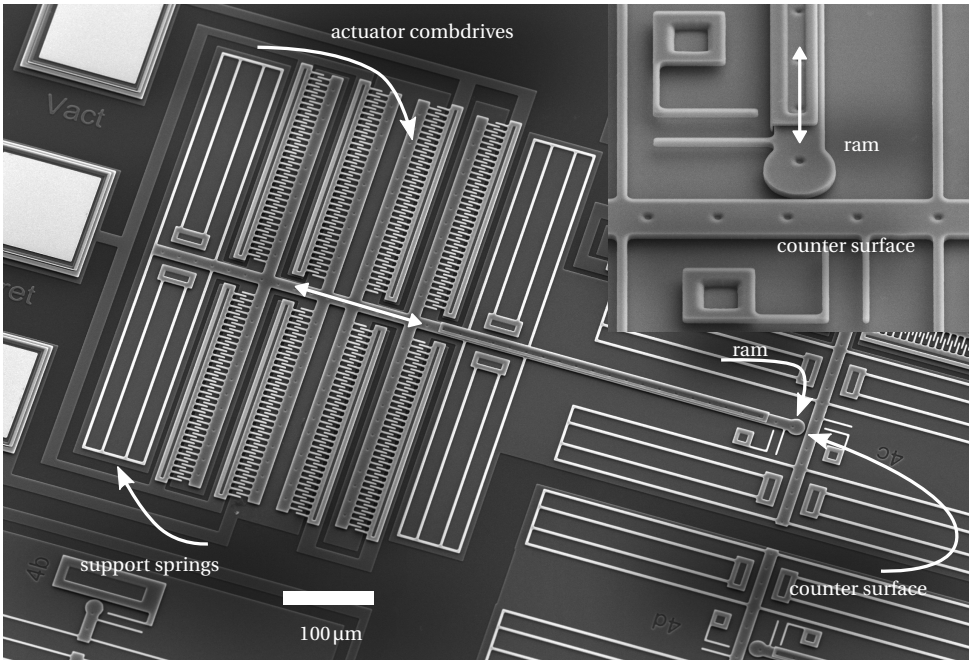

Figure 4.1.: Scanning electron microscope (SEM) micrograph of the MEMS adhesion sensor used in the experiments.

Equation (4.1) shows the force balance of all the forces that act on the adhesion sensor (neglecting air damping),

$$F_{\text{act}} + F_{\text{spring}}(x) + F_{\text{adh}}(x) + F_{\text{contact}} = m \cdot \frac{\mathrm{d}^2 x}{\mathrm{d}t^2} \tag{4.1}$$

where F_{act} (positive) is the force generated by the comb-drive, F_{spring} (negative) is the restoring spring force exerted by the beam springs in which the ram is suspended, F_{adh} (positive) is the adhesion force between the ram and the counter-surface, F_{contact} (negative) is the force exerted by the counter-surface on the ram and m is the mass of the ram.

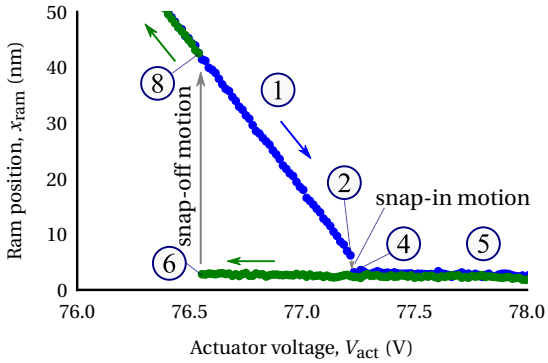

Figure 4.2.: The voltage displacement curve of a single contact cycle, zoomed in on the adhesion hysteresis loop. The important points are marked with numbers 1 to 8 and correspond to the numbers in figure 4.3.

This equation is valid at any value of F_{act}. We can write for F_{spring} and $F_{contact}$:

$$F_{spring} = k_{spring} \cdot x_{ram} \tag{4.2}$$

$$F_{contact} = -k_{contact} \cdot d_{contact} \qquad \text{if } x_{ram} \geq x_{cs} \tag{4.3}$$

where $d_{contact}$ is the elastic deformation of the contact, x_{ram} is the position of the head of the ram and x_{cs} is the position of the counter-surface.

The actuator force F_{act} is the only variable in equation (4.1) that can be controlled directly, by applying a voltage difference V_{act} between the comb-drive actuator fingers.

Figure 4.3 illustrates the events that occur during a single 'contact cycle', by which we mean a forth and back motion of the ram in which it makes and breaks contact with the counter surface.

Before the ram makes contact with the counter surface (1), $F_{adh} = 0$ and $F_{contact} = 0$ and an increase in F_{act} will cause the ram to accelerate and displace. At $x = x_{eq}$, where the restoring spring force $k_{spring} = -F_{act}$, the ram will show a damped oscillation around its equilibrium position. When the voltage is increased so much that x_{ram} is close to the attractive van der Waals, electrostatic and capillary forces between the ram and the counter-surface come into play (2). Their contributions are aggregated in F_{adh}. Typically, F_{adh} depends strongly on the gap distance d_{gap} in a non-linear fashion, so as soon as F_{adh} becomes non-zero while the ram approaches the counter-surface, a stable equilibrium position no longer exists and the ram is pulled into the counter-surface (3). At this point, the reaction force $F_{contact}$ will become non-zero to compensate the force with which F_{adh} pulls the ram to the surface (4). Increasing F_{act} even further will not cause a change in F_{adh}, but the contact will slightly deform due to the non-zero value of $k_{contact}$ (5).

When the voltage is now lowered to the value at which snap-in occurred, the ram will not immediately pull-off from the counter surface, because F_{adh} is still non-zero. When fur-

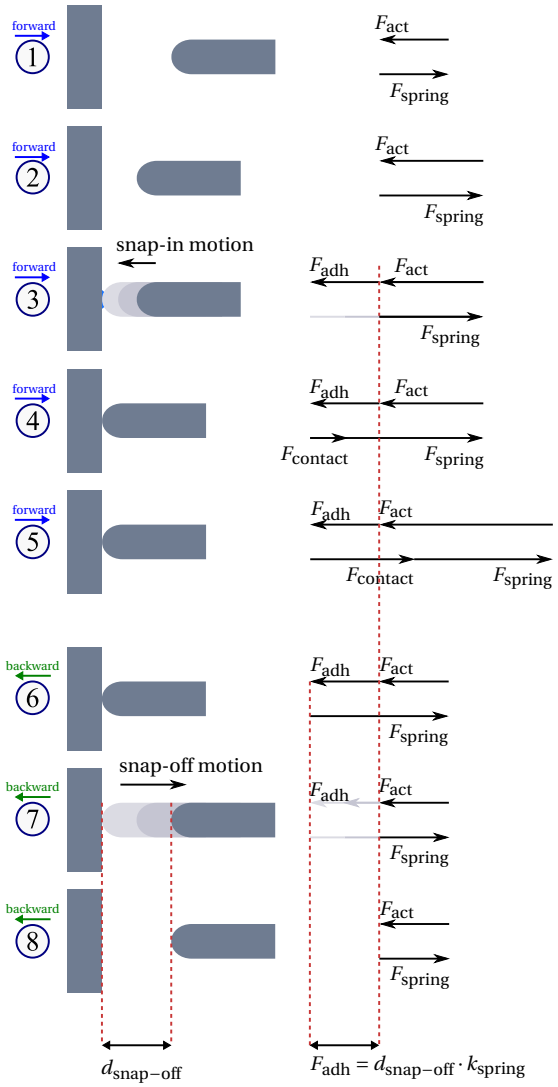

Figure 4.3.: The different phases of a contact cycle. The numbers correspond to the annotations in the graph of figure 4.2. (1) free motion, (2) just before snap-in, (3) snap-in motion, (4) contact right after snap-in, (5) increase contact force, (6) decrease contact force, just before snap-off, (7) snap-off motion, (8) right after snap-off. Note that steps (3) and (7) are not present in figure 4.2, because it only shows stationary positions.

ther decreasing the voltage, at some point the adhesion force will be exactly compensated by the restoring spring force such that $F_{act} + F_{adh} = -k_{spring} \cdot x_{cs}$ and $F_{contact} = 0$, but the ram is still touching the counter-surface (6). An infinitesimally small further decrease in F_{act} causes F_{adh} to become zero, which results in non-zero net force that accelerates the ram back towards its equilibrium position such that $F_{act} = -F_{spring}(x_{eq})$ (7). We can now obtain an expression for F_{adh} that is independent of F_{act}.

just before snap-off:

$$F_{act} + F_{adh} = -k_{spring} \cdot x_{cs} \tag{4.4}$$

$$F_{adh} = -k_{spring} \cdot x_{cs} - F_{act} \tag{4.5}$$

right after snap-off

$$F_{act} = -k_{spring} \cdot x_{eq} \tag{4.6}$$

equating:

$$F_{adh} = k_{spring} \cdot (x_{cs} - x_{eq}) \tag{4.7}$$

$$= k_{spring} \cdot d_{snap-off} \tag{4.8}$$

Where $d_{snap-off}$ is the snap-off displacement length (8). The spring constant of the moving ram can be found by measuring the resonance frequencies of two devices with the same value of k_{spring}, but different values for the device's effective moving mass m_{eff}. The adhesion force can then be determined from the snap-off displacement by multiplying it with the spring constant. This means that we have successfully shifted the problem of measuring a force to measuring a displacement, for which we have an excellent, high-resolution measurement solution.

4.3. EXPERIMENTS

4.3.1. ADHESION SENSOR

In all the measurements discussed in this chapter we used a polycrystalline silicon MEMS adhesion sensor as shown in figure 4.1. It was fabricated the PolyMUMMPS™[71] multi-user MEMS process by MEMScap inc. Figure 4.3 shows the gap distance between the ram and the counter-surface as a function of the voltage between the comb-drive actuator fingers. Using standard cantilever beam approximations [72], we have analytically calculated the spring constant of the battering ram suspension to be $k_{spring} = 2.5 \pm 0.2\,\mathrm{N/m}$. We measure the displacement of the ram by using an optical displacement measurement technique based on curve-fitting (see chapter 2), and experimentally determine the adhesion forces from the observed snap-off distance, as explained in section 4.2.

The adhesion sensors were wire bonded to a ceramic dual-in-line package (DIP) after having been stored in a gel-pack for a short period of time. Before the experiments, the devices had been stored for about a year in the package in which they were shipped to us by the foundry.

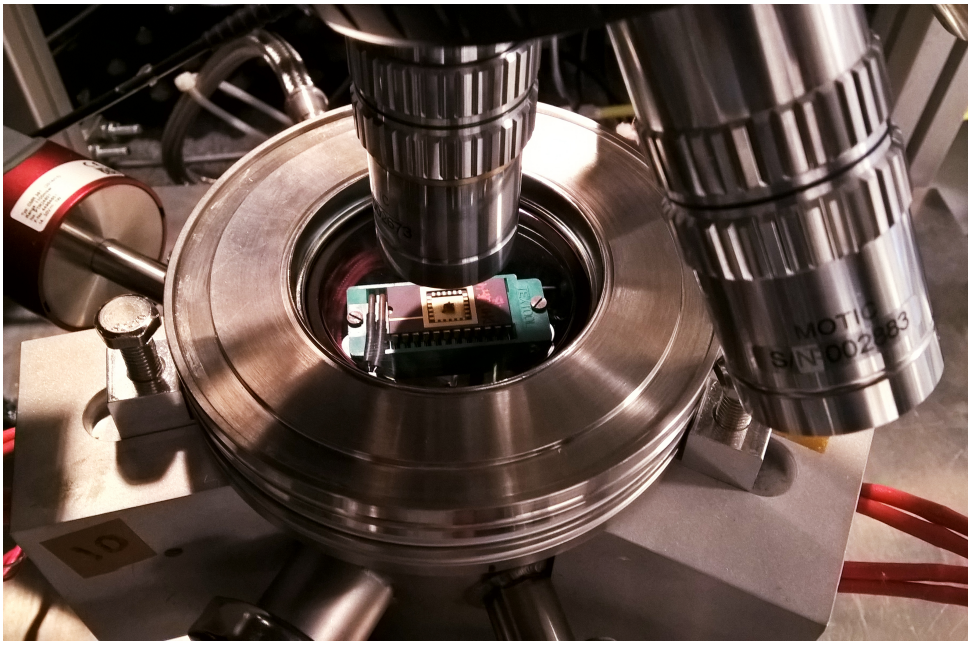

Figure 4.4.: A close-up view of the environmental chamber with a wire bonded adhesion sensor mounted in the socket.

4.3.2. MEASUREMENT SETUP

All adhesion experiments were carried out in a measurement setup that was specifically made for conducting these high-precision force measurements with MEMS devices. It consists of an IDS uEye 3370CP CMOS camera in line with a Motic PSM-1000 optical microscope, mounted above a small environmental and vacuum chamber. Inside the chamber, the DIL-packaged MEMS adhesion sensors are placed into a socket which provides electrical connections to the outside world. The chamber can be closed with a lid that contains a glass view port, which allows optical access from the microscope to the sample. The walls of the chamber are temperature controlled, and can be heated to 110 °C to perform a dehumidifying 'bake-out'. The chamber is fitted with gas in- and outlets, and can be evacuated down to ~1 mbar by a oil-free, membrane-type vacuum pump. To create a dry and inert atmosphere it can be flushed with pure Argon after bake-out and pumping. The atmospheric conditions close to the sample are monitored using a Honeywell HIH4000 humidity sensor and a Pt100 temperature sensor, of which the output is logged every second. The entire setup is suspended in bungee cords inside an acoustic isolation booth. The booth itself is placed on top of an stiff optical table with active pneumatic supports. This construction that we developed ensures maximum mechanical decoupling from the outside world.

Table 4.1.: Summary of the six adhesion experiments that were carried out, sorted by relative humidity of the atmosphere.

Name	Resolution[2]		Humidity	Contact force[1]
	(nm)	(nN)	($\%_{RH}$)	(μN)
B	0.35	0.88 ± 0.07	26 ± 5	3.1 ± 0.2
H	0.31	0.78 ± 0.06	10 ± 5	1.9 ± 0.1
G	0.20	0.50 ± 0.04	10 ± 5	2.2 ± 0.2
J_c	0.24	0.60 ± 0.05	2 ± 5	1.7 ± 0.1
D	0.60	1.50 ± 0.12	0 ± 5	2.8 ± 0.2
J_d	0.23	0.58 ± 0.05	0 ± 5	1.0 ± 0.1

[1] The contact forces listed here are the maximum forces exerted on the contacts by the comb-drive actuators.
[2] The force resolution is calculated from the displacement resolution by multiplying it with k_{spring} =2.5 ± 0.2 N/m.

4.3.3. ADHESION MEASUREMENTS

The adhesion sensor was illuminated through the microscope objective by a liquid light-guide coupled Sutter HPX-L5 90 W LED light source, which has the equivalent light output of a 150 W xenon arc lamp. The optical path of the microscope consisted of a long working distance 20× magnification objective with a numerical aperture of 0.5, an additional 2× magnification lens built into the microscope, and an adjustable diaphragm. The internal diaphragm of the microscope was closed to it's minimum aperture to block any stray light scattered back from the chamber view port. Images were captured with exposure times of around 1 ms per image.

Six adhesion experiments were carried out, under different low-humidity atmospheric conditions. They are summarized in table 4.1. Each adhesion experiment has been conducted using the same procedure. The device was placed in the socket inside the chamber. The ram was moved forwards to make contact with the counter-surface and press against it, and then retracted again. This was achieved by sweeping V_{act} from 70 V to 85 V and back in 2000 discrete steps. After each step an image of the device support springs was acquired from which the displacement was calculated using the curve-fitting method described in [54].

Three million of these contact cycles were executed in total for every device. However, because an accurate measurement of a complete contact cycle takes ~ 30 s, recording all three million cycles this way would take about three years. Therefore, only 50 sets of 20 consecutive cycles were actually recorded. The contact cycles in between the measurement sets were executed at a higher rate of 100 Hz with only 10 voltage steps per cycle. The amount of intermediate cycles between measurement sets was increased exponentially in such a way that the total amount of contact cycles was close to three

million, and the resulting data points are spaced equidistantly when plotted against the logarithm of the total number of elapsed cycles.

4.3.4. ENVIRONMENTAL CONDITIONS

For the experiments carried out in a very dry atmosphere (0 $\%_{RH}$, 0 $\%_{RH}$ and 2 $\%_{RH}$), the chamber was dehydrated by baking it out at 110 °C for about 16 hours while it was being evacuated continuously. After the chamber had cooled down and its walls had reached a stable temperature of 25 °C, the vacuum pump was switched off, and the chamber was filled with 99.99 % pure argon gas.

For the experiments carried out in a wetter, but still fairly dry atmosphere (10 $\%_{RH}$, 10 $\%_{RH}$ and 26 $\%_{RH}$), the chamber was left to 'breathe' for a couple of minutes to equilibrate the chamber atmosphere with the surroundings. The lid was then closed to keep the atmospheric conditions constant throughout the experiment. However, because the chamber temperature was maintained at 25 °C and the laboratory ambient temperature was 21 °C, the temperature of the gas inside the chamber slowly increased to match the chamber wall temperature which caused a corresponding decrease of the relative humidity. In addition, it turned out that the chamber walls acted as a strong 'getter' for water, especially after it had been kept at 0 $\%_{RH}$ for longer stretches of time. The time it took for the relative humidity to become stable turned out to be about a day, much longer than we initially expected. For that reason, the relative humidity was not completely stable in some of the experiments. For the same reason it was not practically possible to obtain high levels of relative humidity with this setup.

4.4. RESULTS

Each experiment yielded a total number of 1000 contact cycles, which amounts to a total of 6000 contact cycles, each consisting of 2000 pictures. We do not show all the raw results here, but we discuss some peculiar details in appendix 4.A.

Figure 4.5 shows the adhesion force against the total number of elapsed contact cycles for all measurements.

The width of the region is a measure for the variability of the adhesion force from contact-to-contact. The colored regions in the graph give a qualitative view of the distribution of the measured adhesion forces in the experiment. The darker region represents the 25 % to 75 % percentile interval, the dark center line is the mean value, and the lighter colored region indicates the total range of measured adhesion forces. The variability is also shown separately in figure 4.6, where the 25 % to 75 % percentile interval of the cycle-to-cycle adhesion force values is plotted against the total number of cycles.

All adhesion trend lines show a slowly varying drift over the total range of 3 million cycles. The lines corresponding to the samples measured under relatively dry conditions: sample J_c, G, H, J_d and D, show a slight increase in adhesion after 10^4 contact cycles. The trend of sample J_d shows a gradual decrease in adhesion after 10^5 contact cycles. The sample

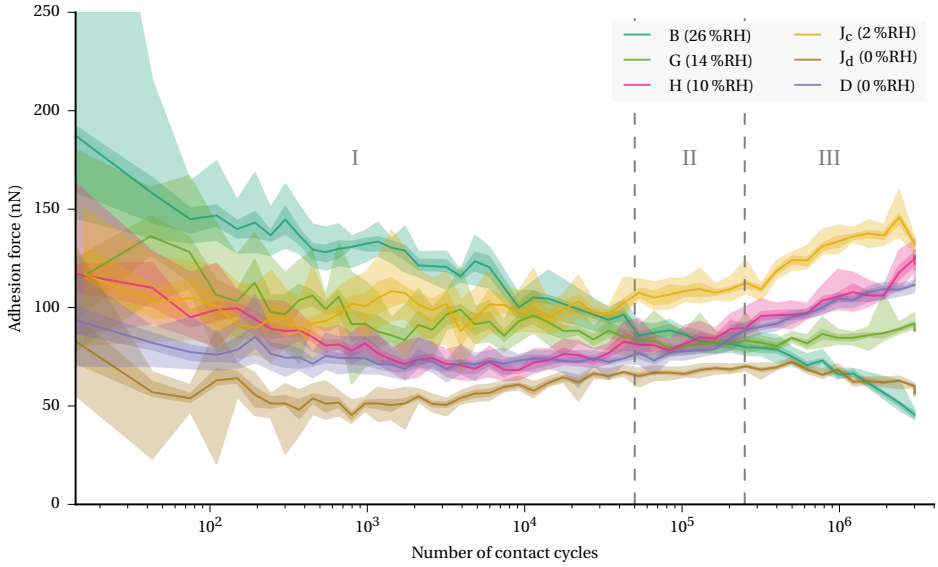

Figure 4.5.: The adhesion force plotted against the total number of contacts for all measured devices. The mean relative humidities during the experiments are indicated in the legend. The colored bands indicate the minimum value, the 25 % and 75 % percentiles, and the maximum value. The solid line indicates the mean.

that was measured under wet conditions, B shows a different trend: the adhesion force decreases almost monotonously.

In all experiments, the cycle-to-cycle variability of the adhesion force is large at the start of the experiment, but decreases rapidly as a function of the number of elapsed contact cycles.

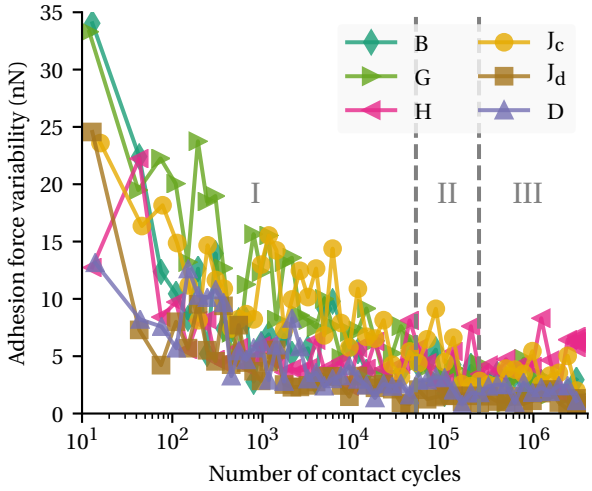

Figure 4.6.: The variability of the adhesion force within each measurement set of 20 consecutive cycles, plotted against the total number of contacts for all measured devices. In all cases the variability decreases with an increasing number of elapsed contacts.

4.5. DISCUSSION

The most striking feature of this set of experimental data is that device-to-device variation due to surface roughness and differences in local sidewall contamination result in strong differences. So strong in fact, that they preclude the possibility to see any overall quantitative similarity of the adhesion force evolution. However, there are certain trends that occur in every experiment. We observe three regimes.

At the start of each experiment, adhesion forces show a large cycle-to-cycle variability. The measured adhesion forces of each individual sample fall within a range of about ±10 nN around their mean value, but the adhesion forces from all experiments combined show a spread that is ~ 5 times larger: from 50 nN to 250 nN. As the number of elapsed contact cycles increases, we clearly see that the adhesion variability of each individual device decreases by about a factor 3. This reduction is caused by flattening of the highest asperities. This behavior is characteristic of regime I.

Table 4.2.: Overview of the three regimes of distinct adhesion behavior observed. The regime names are indicated in all graphs in which the x-axis represents the number of contact cycles.

Regime	Cycles		Description
	From	Until	
I	1	50×10^3	Initial run-in
II	50×10^3	250×10^3	Adhesion stable
III[1]	250×10^3	3×10^6	Adhesion drift

[1] The upper cycle limit of regime III was not experimentally determined, but was dictated by the total number of cycles in the experiment.

All adhesion curves seem to converge into a narrow range of 65 nN to 115 nN between 50×10^3 contact cycles to 250×10^3 contact cycles (regime II). This convergence can be the indication of a physical process that makes the sidewall surfaces appear fairly similar after the initial run-in. After 250×10^3 cycles the curves start to diverge again (regime III).

Because the adhesion run-in is a process that slows down exponentially as more contact cycles have elapsed, all the graphs that we have shown in the results section have a logarithmic horizontal axis. Figure 4.7 shows the first half of the data that was shown in figure 4.5 on a linear scale. The details of the initial run-in have become obscured, but the general trend is shown in completely different light: after a run-in of 50 000 cycles, the adhesion force is stable for the next 200 000 cycles.

4.6. AN EMPIRICAL MODEL TO DESCRIBE THE ADHESION FORCE DRIFT

The fact that the measured data are fairly similar for the different humidities proves that if the humidity is low enough not to cause large-scale capillary bridges, its' effect is not pronounced. In the following we therefore treat the measurement data as a single set with no differences between the devices other than regular statistical variation. We can extrapolate the data in figure 4.5 to predict the expected adhesion drift for longer-term operation of the devices. To obtain reliability predictive power from the measured data we can take several routes. As the MEMS system is too complex for direct physical modeling, a new empirical model is needed. Here we present two of these models, both with their strong points and limitations, as presented below.

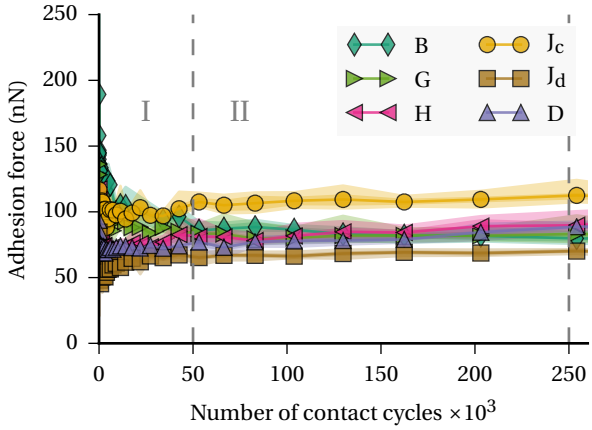

Figure 4.7.: The adhesion force versus the first 250 000 cycles on a linear scale. This shows the first half of the graph in figure 4.5 in a different light. Although the run-in happens logarithmically and does not actually stabilize, an initial run-in of 50 000 cycles stabilizes the adhesion behavior during the next 200 000 cycles.

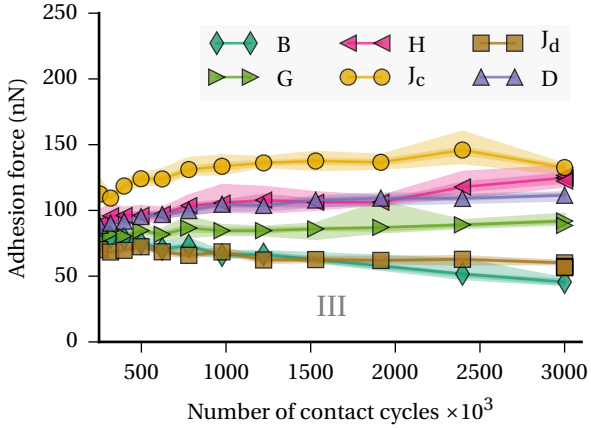

Figure 4.8.: The adhesion force values in regime III versus the number of elapsed cycles on a linear scale from 250×10^3 to 3×10^6 contact cycles. In this regime the curves start to diverge again from the stable values of regime II.

Table 4.3.: Determination of the standard deviation of F_{start} and F_{drift} for the measured data of figure 4.5 in Regions II and III.

Sample	F_{start} (nN)	F_{drift} (nN/$\log_{10} n$)	ΔF_{rw} (nN/$\sqrt{n}$)
B	105.1	–20.6	-34.7×10^{-3}
G	96.1	–2.7	1.6×10^{-3}
H	72.1	22.2	29.5×10^{-3}
J_c	100.5	18.3	32.2×10^{-3}
J_d	57.7	0.3	-1.88×10^{-3}
D	74.1	17.2	29.2×10^{-3}
mean	84.3	5.77	8.78×10^{-3}
std. dev.	18.9	16.5	26.5×10^{-3}

4.6.1. THE SIMPLE LOG(N) FIT MODEL

For the simplest model, we us the experimentally observed fact that on the semi-logarithmic plot in figure 4.9 the adhesion long-term drift is roughly linear in Region II and III. The corresponding first order model starts by noting that the adhesion $F_{adh}(n)$ in a single experiment in such a case can be written according to the following equation:

$$F_{adh}(n) = F_{start} + F_{drift} \cdot \log(n) - F_{drift} \cdot \log(n_{start}) \tag{4.9}$$

In this equation n is the number of cycles that the experiment is running in total, and n_{start} =10 000 cycles: roughly the cycle number from which point most curves plot roughly linear. F_{start} is the adhesion measured at n_{start} cycles and F_{drift} is a fit parameter that defines the average slope of the measured curve in region II and III. Both F_{start} and F_{drift} can be obtained by curve fitting equation (4.9) to the measured data in region II and III combined. If we perform this curve fitting procedure for all measured curves we can calculate the mean and standard deviation of F_{start} and F_{drift} of the measurement. For the data of figure 4.5 these are given in table 4.3.

We define the $\bar{x}$ operator as giving the mean of x, and the $|x|$ operator as giving the average deviation of x. The predicted one standard deviation boundaries on the adhesion force for large n give the predicted adhesion with its most probable drift, for which we use the notation $\{F_{adh}(n)\}$. For this model we get as the prediction for the average drift adhesion boundaries as a function of the number of cycles:

$$\{F_{adh}(n)\} = \overline{F_{start}} \pm \left(|F_{start}| + \overline{F_{drift}} \cdot \log(n) - \overline{F_{drift}} \cdot \log(n_{start}) \right). \tag{4.10}$$

The prediction of equation (4.10) is that the adhesion drift goes with a comforting $\log(n)$ and will not grow very large with higher numbers of cycles for reasonable values of

n. The predictive power of this model of course depends on the underlying validity of equation (4.9). With a second model we show that this assumption need not necessarily be true.

4.6.2. THE RANDOM WALK MODEL

For the second model the adhesion shown in figure 4.5 in region II and III is interpreted as showing a 'random walk' type of behavior. This choice is made because of the erratic drift of F_{adh} that sometimes even changes sign. A simple random walk of a variable Z is defined as $Z_n = \sum_{j=1}^{n} Z_j$, with $Z_j = 1$ or $Z_j = -1$ with equal probability, and n the number of steps. The expectation value of Z_n itself is zero: the possibilities of the walk are symmetrical around 0. However, the expectation value E of the average deviation from zero of Z_n is $E(|Z_n|) \approx \sqrt{\frac{2n}{\pi}}$ for large n, with the $|x|$ operator again defined as giving the average deviation of x.

For large n the $\sqrt{n}$ factor of the average deviation of the standard random walk has a higher second derivative than the $\log(n)$ relation of equation (4.9). Hence the deviations of F_{adh} for high n are expected to be larger in the case of the random walk than those in the $\log(n)$ model of equation (4.9). It is true that as the number of cycles increases, the variation per step is seen to decrease slightly in the measurements (figure 4.6) unlike the step size in the simple random walk described above. However, the change is not quite large enough to cause a significant change in the shape of the $\sqrt{n}$ function behavior; for large n it represents just a scaling factor. Assuming underlying random walk statistics for the adhesion experiment, the equivalent fit function of equation (4.9) becomes:

$$F_{\text{adh}}(n) = F_{\text{start}} + \Delta F_{\text{rw}} \cdot \sqrt{n} - \Delta F_{\text{rw}} \cdot \sqrt{n_{\text{start}}}, \tag{4.11}$$

in which the fit parameter ΔF_{rw} absorbs the factor $\sqrt{\frac{2}{\pi}}$ and is the random walk equivalent of F_{drift} in equation (4.9). The fit parameters are given in table 4.3. For the random walk model we get as the prediction for the average adhesion plus drift as a function of the number of cycles:

$$\{F_{\text{adh}}(n)\} = \overline{F_{\text{start}}} \pm \left(\|F_{\text{start}}\| + \overline{\Delta F_{\text{rw}}} \cdot \sqrt{n} - \overline{\Delta F_{\text{rw}}} \cdot \sqrt{n_{\text{start}}} \right). \tag{4.12}$$

4.6.3. DISCUSSION

In figure 4.9 we show a comparison of the two model predictions and the measured data. Both models describe the measured data quite well. The initial 'stability' of the adhesive force in Region II and the subsequent diverging adhesive force in Region III is a prominent feature of the random walk model, but is absent in the $\log(n)$ model. This may favor the random walk model over the $\log(n)$ model.

At the end of Region III the slopes of the curves of the two models differ considerably. If the adhesion drift is dominated by random walk statistics, the expected drift will be much higher than if it is governed by the $\log(n)$ model. A long-term test up to a much

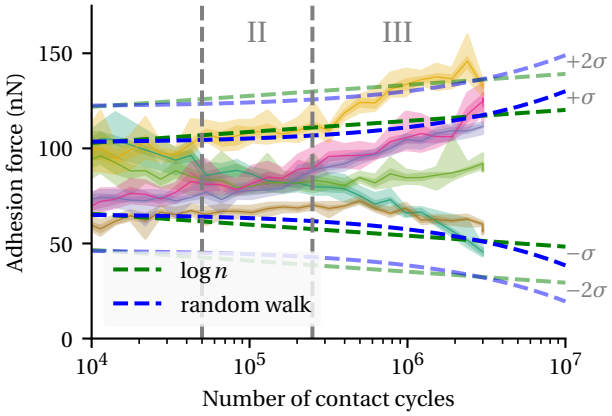

Figure 4.9.: Measured adhesive forces and predicted average deviation of the adhesive force for the $\log(n)$ model in equation (4.9) and the random walk model in equation (4.12).

higher number of cycles, preferably with more devices, is recommended to experimentally distinguish between the two models. This is important to be able to predict the real-life adhesion drift that can be expected during log-term operation of MEMS devices with contacting surfaces.

4.7. CONCLUSION

Thanks to the sub-nanonewton force resolution of our measurement technique, we have been able to observe the adhesion force between polycrystalline silicon MEMS sidewalls with unprecedented detail. The results in this chapter clearly demonstrate the differences in the contact mechanics of devices that are in every way identical, apart from the fact that they are not actually the same device. Small variations in surface roughness and hence in maximum normal contact force and local capillary condensation may play a major role in determining the strength and evolution of the adhesive force in these contacts. More experiments should be conducted in order to shed light on what exactly causes all the different effects that we observe. For the first time however, we actually have obtained a quantitative insight in how MEMS contacts evolve over a large number of contact cycles under low force conditions. Although the cycle-to-cycle variability decreases after $\sim 10^2$ cycles, the gradual change of the adhesion force as a result of run-in does not stabilize, even after 3 million cycles. This drift of the adhesion force during millions of cycles is comparable in magnitude to the initial run-in drift. Silicon MEMS devices that rely on the presence of a stable and repeatable adhesion force will therefore not work reliably over many cycles. However, if the intended lifetime of the device is limited, a stable adhesion

force can be achieved by running-in the contacting surfaces for roughly 10 % of their intended lifetime, and keeping the total number of cycles under 260×10^3.

4.A. GRADUAL PULLBACK AND CONTACT DEFORMATION

Due to the sub-nanometer resolution of our measurements we have observed some interesting effects that do not affect the main story and conclusion of this chapter, but deserve some publicity nonetheless: inelastic contact deformation (ICD) and gradual pullback.

After the ram is snaps into the counter surface and F_{act} (and therefore $F_{contact}$) is increased, the contact will always deform somewhat, due to the non-zero compliance of both the contact itself and the counter-surface suspension. In the case of elastic contact deformation, the displacement of the ram is independent of time and history, and the forward and backward voltage-displacement curves will overlap. In the case of inelastic contact deformation, the contact will deform permanently (at least within the time-frame of the measurement) when F_{act} is increased, and as a result the forward and backward voltage-displacement curves will not overlap.

Gradual pullback is measured when the ram does not snap-off from the counter surface in one discrete jump, but gradually retracts several nanometers before it snaps-off. In some cases, this 'gradual pullback length' appears to match the amount of ICD. Both ICD and gradual pullback can be present after any number of contact cycles, as is shown in figures 4.10 to 4.12.

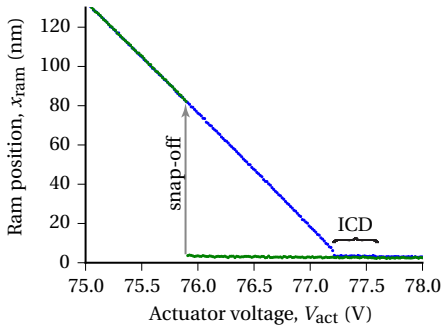

Figure 4.10.: The voltage-displacement curve of the first cycle of experiment G, zoomed in around the voltage region in which contact is made and broken (the maximum voltage in this measurement is 85 V). A small amount of inelastic contact deformation is visible just after snap-off, and an equally small amount of gradual pullback can be discerned just before snap-off.

Figure 4.10 shows the voltage-displacement curve of the first measured cycle in experiment G. It is one of the smoothest curves in all of the experiments, with a displacement noise of only 0.21 nm RMS. However, a tiny small amount of inelastic contact deformation (ICD) and gradual pullback can still be discerned.

Figure 4.11 shows the voltage displacement curve of the 445th curve of experiment D. In addition some elastic contact deformation, both ICD and gradual pullback are visible.

The contact does not deform immediately after the ram makes contact with the counter surface but only after V_{act} has been increased by an additional ~ 7 V. In this measurement, 'gradual' pullback does not happen gradually, but happens in one discrete jump to the same displacement at which the ram and counter surface first made contact, before the contact was deformed.

This behavior can be explained by the assumption that the initial contacting surfaces have two large asperities that first make contact tip-to-tip, but with a slight misalignment. After a certain increase in force, the asperities start to slide sideways, until they settle into a more stable contact. When F_{act} is decreased, the ram will first move back to the initial contact position before snapping off.

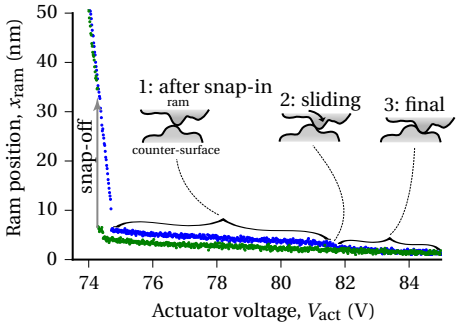

Figure 4.11.: The voltage-displacement curve of the 445th cycle of experiment D, zoomed in on the voltage range in which the ram and counter surface are in contact. The contact remains stable for a while (1) until 81.5 V, where the ram slides a bit further (2) and settles itself into a more stable position (3). The ram snaps-off in two discrete steps. The length of the first jump matches the amount contact deformation.

Figure 4.12 shows the voltage displacement curve of the last cycle of experiment D. Both gradual pullback and ICD are clearly visible, but look very different compared to figure 4.11. The contact deforms at a much lower force than before and gradual pullback happens very smoothly over a distance of ~ 6 nm, almost twice the amount of inelastic contact deformation. The decrease of the force required to push the ram into it's favored position (situation (3) in figure 4.11) is likely caused by a smoothing of the sliding asperity, and a decrease of the local friction force. We currently have no solid explanation for the origin of the smooth and long gradual pullback, but we believe it to be caused by the *in situ* tribo-synthesis of a viscous compound. Crushed together by the contact force, hydrocarbon contaminants may have combined with water and SiO_2 debris, forming a nm-thick silicone-like substance on the surface.

Figure 4.13 show the gradual pullback length versus the number of elapsed contact cycles for all the experiments discussed in this chapter. The plotted values are the median values of the gradual pullback lengths in each measurement set of consecutive cycles. In experiments D and J_d the gradual pullback effect appears quite suddenly, after 10^2 to 10^3 cycles. In experiment G the effect also appears suddenly, but only after ~ 10^5 cycles. In

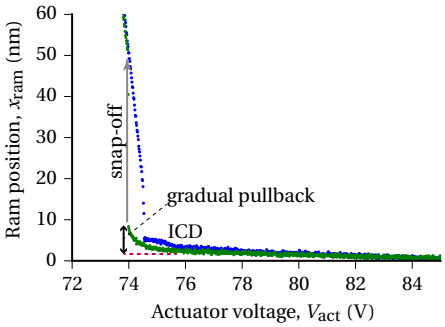

Figure 4.12.: The voltage-displacement curve the last cycle of experiment D. While the ram pushes into the counter surface. A significant amount of inelastic contact deformation (ICD) can be seen, as well as a smooth gradual pullback before snap-off.

experiments H and J_d, the gradual pullback length increases more gradually, but suddenly becomes much higher and somewhat erratic between 10^4 to 10^6 cycles. Experiment B, with the highest relative humidity of 26 $\%_{RH}$, shows no gradual pullback across the entire range of contact cycles.

Gradual pullback was notably absent in the experiment with B which was performed at 26 $\%_{RH}$. The dramatic gradual pullback effect that we observed in previous work [54] at 40 ± 10 $\%_{RH}$ was completely absent. Taking into account that the devices used in the experiments of the current chapter were much newer than the devices used in [54] and hence much less contaminated, it appears that the device's contamination history plays a more important role than relative humidity at these low humidity levels, possibly except in the case of experiment B (26 $\%_{RH}$).

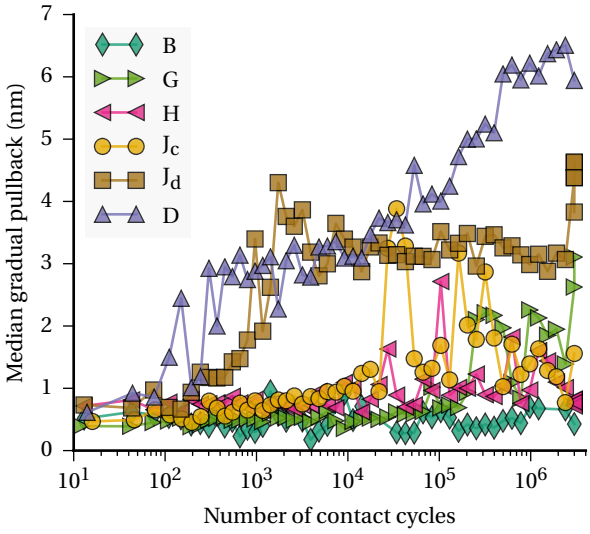

Figure 4.13.: The gradual pullback length versus the total number of elapsed cycles. The data points represent the median of each set of 20 consecutive measurement cycles.

5

ATOMIC SCALE ADHESION PHENOMENA IN MEMS

In the previous chapter we presented the results of the measurement of the evolution of the adhesion force between two MEMS sidewalls in repeated contact. We found that when a contact is broken, the snap-off is not always instantaneous, but may happen gradually. In this chapter we study this effect as it occurs in a MEMS device with contaminated surfaces. The contact shows viscoelastic deformation, hinting at the presence of a tribo-synthesized rubber-like compound on the surface.

This chapter was published as a standalone conference paper [54]. Some editorial changes were added for including it in this thesis.

5.1. INTRODUCTION

A major cause of the unreliability of MEMS devices with contacting surfaces is adhesion [73]. This is the case not only because adhesion is much stronger than in macro scale systems, but also because it is highly variable and changes with the amount of contact cycles[74]. Especially the last issue has a major impact on the long-term reliability of the devices. It is therefore important that is effect is studied in detail to elucidate the exact mechanisms that cause it. We have developed an optical setup with a sub-nm displacement and sub-nN force resolution, sufficiently high to follow atomic-scale changes occurring during repeated contact between the MEMS surfaces.

In this work we will describe two similar experiments to measure the so-called 'run-in' behavior of adhesion between two contacting sidewalls: the evolution of the adhesion force as a function of the number of cycles. These experiments are hence a perfect showcase for the capabilities of this optical measurement method.

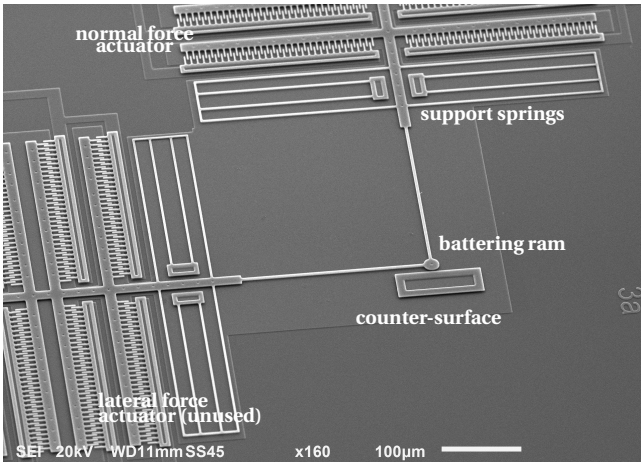

Figure 5.1.: SEM micrograph of the MEMS tribometer. We only used the normal direction comb-drives for the adhesion experiments.

We measure the adhesion force between the sidewalls of two identical silicon MEMS tribometers (figure 5.1). The devices have a comb-drive actuator array that pushes a 'ram' against a 'counter-surface'. A second comb-drive actuator array allows the ram to be pulled sideways while it is in contact with the counter-surface, to allow the study of sliding friction. However, in this chapter we only use the first, normal-force comb-drive array. The ram is suspended by beam springs of which the combined spring constant is $k_{\text{spring}} \approx 2\,\text{N/m}$.

When the voltage on the comb-drives is increased, the ram will move forward until it makes contact with the counter-surface. A further increase of the actuator voltage will not cause any motion, but will push the ram against the counter-surface with a larger force. If there were no adhesion between the sidewalls of the ram and the counter-surface, the

position of the ram at any voltage would be exactly the same on the way back as it was on the way forward, and the voltage displacement curve would look like the 'ideal' curve shown in red in figure 5.2. When adhesion forces are present, a snap-in displacement will show up in the forward-motion of the ram, and a snap-off motion will show up in the backward motion of the ram. We will refer to a graph like this as a 'contact cycle'.

The total adhesion force is calculated by multiplying the snap-off distance with the spring constant k_{spring}. The contact force that is exerted by the ram on the counter-surface can be found by extrapolating the parabolic voltage-displacement curve to the highest value of the actuator voltage, subtracting it from the contact position and multiplying it by k_{spring}.

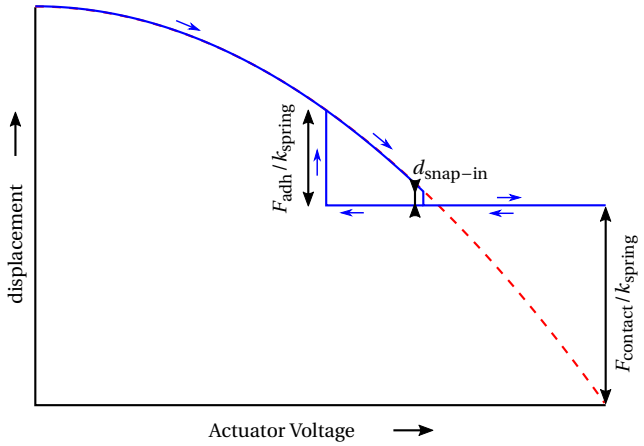

Figure 5.2.: An 'ideal' voltage-displacement curve of the ram as it would look when there are no adhesion or contact forces (red, dashed). When there are adhesion forces, a snap-in can be observed just before the ram should ideally make contact with the counter-surface and a snap-off can be observed when the ram sticks to the counter-surface and is pulled free by the restoring spring forces.

5.2. EXPERIMENTAL

The MEMS tribometers that we used where fabricated in the MEMSCAP PolyMUMPS commercial multi-user MEMS process. Two devices were used that we will refer to as 'device A' and 'device B'. They are identical in design and were fabricated in the same fabrication batch in 2011 on different wafers. Device A was mounted in a ceramic dual in-line package (DIP) in 2013 and had since then been stored on conductive carbon foam inside a plastic container. Two months before this experiment took place, the device was heated to 120 °C at 3 mbar for several hours in an unrelated experiment. Device B had been stored on the relatively clean MEMSCAP drumhead, on which it was shipped by MEMSCAP to our laboratory and was mounted in a ceramic DIP about a week before the

measurement took place. Put in simpler terms: device A is heavily contaminated on the atomic scale, device B is relatively clean.

Our measurement setup consists of an optical microscope fitted with a CMOS machine vision camera. It is mounted above a small environmental chamber that contains zero insertion force (ZIF) socket in which the device under test is placed. To isolate the system from external mechanical vibrations, the entire assembly is suspended in bungee-cords inside an acoustic isolation booth on top of a vibration isolated table with active pneumatic supports. The environment has a controlled relative humidity of 55 %. The chamber was not closed, but the temperature of its walls was kept at 25 °C.

The displacement of the ram is measured with a technique that employs a basic optical microscope and camera to detect in-plane displacements with sub-nanometer resolution (see chapter 2). The region of interest of the camera is centered on a pair of beams of which one will move together with the ram and the other one is stationary. By fitting an analytical function to the intensity profiles of these beams and extracting the horizontal shift, the position of the ram is measured with a position-resolution of 0.5 nm.

5.2.1. MEASUREMENT PARAMETERS

For each recorded voltage-displacement curve, the actuator voltage of the ram was swept in 3000 discrete steps from 65 V to 78 V for device A and from 60 V to 78 V for device B. The maximum contact force was calculated to be ~0.8 µN for device A and ~2.0 µN for device B. At every step an image was captured from which the ram displacement was determined using the displacement measurement technique described in chapter 2. Because recording a single contact cycle this way takes about 50 s, it is not practically feasible to record millions of contact cycles. Instead we recorded 50 sets of 20 consecutive contact cycles. Between these sets an exponentially increasing number of unrecorded cycles was performed a much higher rate of 100 Hz, such that the total number of contact cycles was close to 3 million. One complete experiment took about 22 hours.

5.3. RESULTS

Figure 5.3a shows a typical contact cycle of which 50 × 20 sets were recorded for each device. From each curve we extracted 3 quantities: the 'snap-in length', the 'instantaneous snap-off length', and the 'gradual pullback length'. The snap-in length is the distance that the ram jumps when it makes contact with the counter-surface when it approaches the counter-surface. The instantaneous snap-off length is the distance that ram jumps when it is first pulled free from the counter-surface. The gradual pullback, which is zero in figure 5.3a, but clearly visible in figure 5.3b, is the distance in which the ram is pulled free from the counter-surface in a gradual and occasionally stepwise manner. A fourth quantity, the 'total adhesion length' can be calculated by summing the gradual pullback and the instantaneous snap-off. It corresponds to the difference between the last point where the ram was in full contact with the counter-surface and the point where it has been pulled free completely.

In figure 5.4 and figure 5.5 we have plotted the measured values of these four quantities versus the total number of elapsed cycles. The lines and the error bars represent the mean and the standard deviation of a set of 20 consecutive cycles. Note that the error bars are not a measure for measurement uncertainty, but for variability of the adhesion from cycle to cycle.

5.3.1. CONTAMINATED DEVICE A

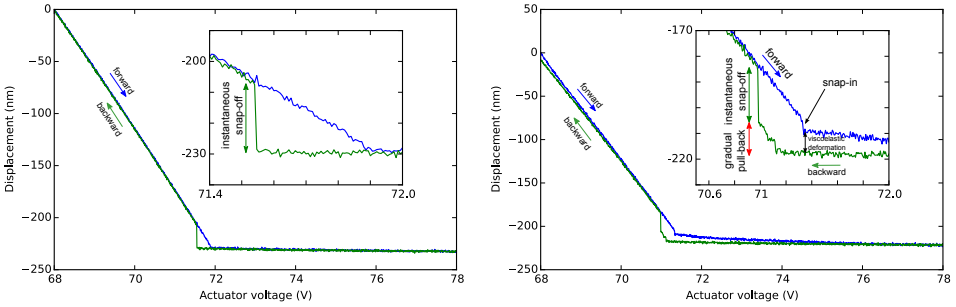

(a) (b)

Figure 5.3.: Two contact cycles recorded from device A. (a) The first measured contact cycle of region I. First the ram approaches the counter-surface, at 71.9 V it snaps into the counter surface. The force is further increased to 786 nN at 78 V. When the force is decreased, the ram sticks to the counter surface until it suddenly snaps off at 71.55 V. (b) The first measured contact cycle of region IV, after 1 914 518 cycles. The contact deforms while the ram pushes against the counter-surface. On the way back, the contact moves back only slowly, indicating the presence of a species on the surface with a long viscoelastic relaxation time. Around 71.1 V the ram starts to pull back from the counter-surface in a step-like way, until it snaps off at 70.95 V.

The adhesion of contaminated device A passes through four regions of distinct behavior that are indicated in figure 5.4 with roman literals I–IV. Throughout region I, all measured contact cycles look similar to the one shown in figure 5.3a: the ram snaps off from the counter-surface in one big jump and the instantaneous snap-off is equal to the adhesion length.

After 300 cycles (region II) the total adhesion drops, and becomes significantly less variable. The drop in total adhesion coincides with the appearance of gradual pullback in the backwards motion curve. This behavior is observed in all contact cycles that follow. Interestingly, the variability of the gradual pullback and the instantaneous snap-off do not get smaller, but the total snap-off (the sum of their values) does, indicating that the two are correlated. Throughout region II, the total adhesion gradually increases from 38 nN to 56 nN.

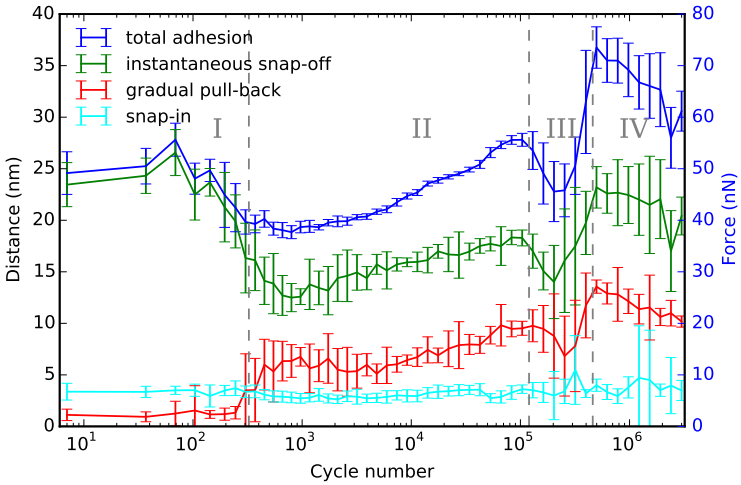

Figure 5.4.: The adhesion force evolution versus the number of contact cycles of for contaminated device A. The adhesion develops in four distinct stages of which the transition boundaries correlate to a change in shape of the adhesion curves.

After 10^5 cycles (region III) the mean total adhesion drops from 56 nN to 46 nN and then rises to 74 nN. Throughout region III, the variabilities of the gradual pullback and the instantaneous snap-off increase by almost a factor 10. From the start of region III, the variability of the total adhesion is much higher than it was in region II, indicating that the correlation between the gradual pullback and the instantaneous snap-off has disappeared.

Figure 5.3b shows the first cycle of the set of measurements that was taken after 1 914 517 contact cycles. After the ram has snapped-in, the contact deforms when the ram pushes into the counter-surface and stays deformed when force is decreased. This viscoelastic behavior first occurs at the start of region III and gradually increases throughout regions III and IV. This phenomenon is most pronounced in the first measured cycle of a set of 20. It appears to relate to the low acquisition speed of the measurement compared to the 100 Hz contact cycles before it, which suggests that this is a dynamic effect related to the relaxation of a rubber-like compound on the surface.

5.3.2. CLEAN DEVICE B

All of the recorded adhesion curves of device B look similar to the one shown in figure 5.3a: there is no significant gradual pullback so the total adhesion is always equal to the instantaneous snap-off length. Throughout the experiment the total adhesion decreases gradually from 260 nN to 140 nN. The variability of the total adhesion in region I varies between 10 nN and 20 nN, but instantaneously decreases to between 4 nN and 6 nN after

780 cycles (region II) and stays in that regime until about 300 000 cycles have occurred (region III). Thereafter, the variability increases to above 10 nN and the mean total adhesion drops by about 20 nN. From 2 million cycles onwards (region IV), the variability drops to around 4 nN and the mean total adhesion decreases monotonously.

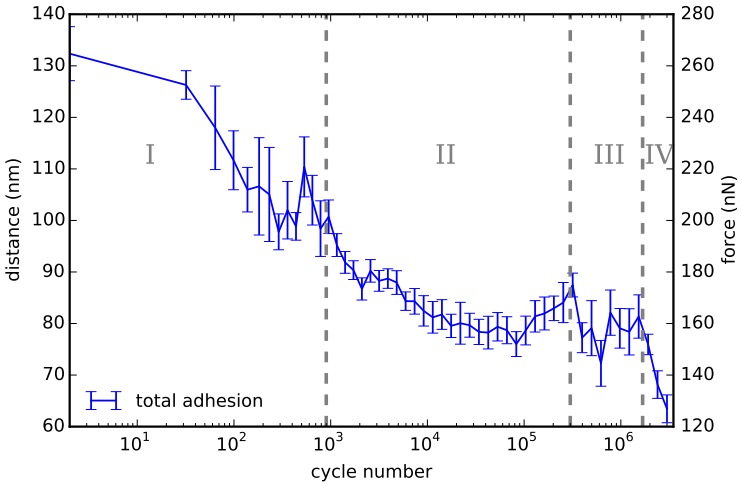

Figure 5.5.: The adhesion force evolution versus the number of contact cycles of for clean device B.

5.4. DISCUSSION

The magnitude of the adhesion force in the cleaner device B is about five times as large as the adhesion force in the more contaminated device A. This is likely to be caused by the presence of a larger number of hydrophobic hydrocarbon contaminants on the surface of device A. The evolution of the mean magnitude of the adhesion force as a function of the number of elapsed contact cycles develops very differently for the two devices. In the case of device A, the magnitude of the adhesion force rises and falls alternately with a larger number of elapsed cycles, while for device B, the adhesion force is almost monotonously decreasing over the entire range of elapsed cycles. The different regions that occur in the evolution of the adhesion for device A are correlated with the appearance of gradual pullback and viscoelastic deformation in the adhesion loops, but for device B, the adhesion consist only of instantaneous snap-off and no such correlation exists.

Despite these differences there are also a number of similarities. For both devices, the adhesion force has a large variability throughout region I, but becomes significantly less variable at the onset of region II. This may be an indication that in region I the surface is continuously being modified because of the repeated contact. Asperities break and form, third bodies come into play and covalent bonds are continuously being made and broken.

After a while the surface topology will have stabilized and all of the dangling bonds will have been passivated [22], so the adhesion force is now mainly dependent on capillary forces. The magnitude of the adhesion force is about five times as large in the cleaner device B than in the dirtier device A. This is likely to be caused by the presence of a larger number of hydrophobic hydrocarbon contaminants on the surface of device A.

In both devices the variability increases significantly after about $\sim 10^5$ contact cycles. In device A this appears to be caused by the onset of tribochemical reactions, indicated by the viscoelastic contact deformation that appears in the voltage-displacement graphs. Although no such behavior is observed in device B, it is not unlikely that the same physics is at work. Since the device will not be entirely free of hydrocarbons, tribochemical reactions are still a possibility.

5.4.1. CONCLUSION

Before the development of our optical displacement technique, it was hard to carry out adhesion run-in experiments with the resolution achieved in this chapter. The ability to measure single contact cycles with nanometer accuracy is required for understanding the physics behind the evolving adhesive contact, which is a major concern for MEMS device reliability. In this study we have compared two grossly different versions of the same device (clean and contaminated) and we have observed large differences as well as similarities in their behavior during a multiple-cycle measurement. Not just the total snap-off length and total adhesion force are important indicators for the underlying processes, but also snap-in length, gradual pullback and even viscoelastic contact deformation are important and can be well observed with our optical measurement technique. We have found that besides the mean value of these parameters, their cycle-to-cycle variability is an equally important metric to observe, because it carries information about the different stages in the evolution of the adhesion during a multi-cycle measurement.

We conclude from this work that the history of a device has a major influence on its contact mechanics. Gradual pullback and even viscoelastic contacts are likely to be common phenomena in MEMS devices, that have not been observed before due to the limited resolution of the measurement techniques that were available until now. The adhesion force of each individual device varies by a factor four over a total range of 3 million cycles, while the adhesion difference between the devices varies by a factor seven. It remains to be seen whether the adhesion will not vary even more with a larger number of cycles. This presents a major concern for the reliability of MEMS, especially when the surfaces are contaminated, or become contaminated during their operational lifetime by outgassing of their package.

6

MESO-SCALE FRICTION

In chapters 4 and 5 we studied contact adhesion by measuring the displacements normal to the surface. In this chapter we use our optical displacement detection technique to measure the lateral displacements of two components in sliding contact to study friction. We experimentally address a fundamental aspect of friction in MEMS, and of meso-scale friction in general: the fact that it has not been well understood until now how energy is dissipated exactly in a meso-scale sliding contact. We observe two separate energy dissipation mechanisms of comparable magnitude: one related to the microscale surface roughness, and one related to the nanoscale tribological properties of the asperities.

This chapter was published as a standalone journal paper [75] and corrigendum [76]. Some editorial changes were added for including them in this thesis.

6.1. INTRODUCTION

The field of macro-scale tribology – the study of friction, wear, and lubrication – has long since been occupied with the acquisition of tabular data on lubricants, friction coefficients and wear rates, under a large number of circumstances. This is extremely valuable information when designing a macro-scale mechanical system like an engine, or a mars rover. There are phenomenological models [3–7] which predict the behavior of macroscale friction forces to a certain extend, but still no physical models exist that are capable of predicting the tabulated values from first principles.

At the atomic scale, the bottom end of the size spectrum, the situation is rather different. Great advances have been made in our understanding of atomic scale friction due to the invention of friction force microscope (FFM), which has led to the discovery of phenomena like atomic stick–slip[77], superlubricity [20, 21], and substrate induced ice formation at room temperature [18]. The Prandtl–Tomlinson model [2] predicts the tip motion of an FFM with reasonable accuracy. This is possible because an FFM has only a single point of contact, or asperity, whereas in a macro-scale system, the total number of asperities approaches infinity.

Unfortunately, neither the wealth of empirical data available for the macro-scale nor the 'simplicity' of the atomic scale directly solves the challenges that arise when operating somewhere in between these scale regimes: at the meso-scale. At this scale, the contact area of two touching components is typically of the same order of magnitude as the surface roughness features, which means that the contact mechanics can differ greatly from place to place on the very same surface [17]. Tabulating generic empirical data for engineering purposes is therefore nearly impossible. Because the number of asperities is larger that one, but too small to be considered infinite, both the analytical and empirical models are invalid at the meso-scale.

The primary man-made occupants of the meso-scale are MEMS: tiny mechanical devices, fabricated using the same processes that are used for producing microelectronics. Many MEMS devices have found their ways into our daily lives, such as airbag sensors, the inertial sensors and microphones of smartphones, and inkjet printer heads. However, because of the small size of these devices, the surface-to-volume ratio of their moving components is much larger than in a macro-scale system. This causes surface interaction forces to dominate most other forces in the system. MEMS devices that rely on touching or sliding components for their operation are therefore highly unreliable. The MEMS community has dealt with this fact mostly by designing and fabricating only devices without sliding components.

Important steps have already been taken towards a solution. Self-assembled monolayers [78, 79], hard coatings [56], and especially vapor-phase lubrication [69] have been shown to work well for silicon MEMS devices, and hard materials like silicon carbide [80] and diamond [47] have been used as a replacement for silicon as the devices' structural material.

Despite these practical advances however, our understanding of the physical processes that govern the contact mechanics in MEMS is still in a poor state. This is in part because

it is still difficult to measure contact forces in MEMS with a high resolution.

Friction measurements in MEMS are usually performed using MEMS tribometers [44, 81, 82]. These are MEMS devices which have been built specifically to measure friction forces between two contacting surfaces of the tribometer itself. Friction forces are usually determined indirectly from the measured displacements of the sliding components of the tribometer. Many types of tribometers exist today, enabling friction and wear measurements under many different circumstances.

The data that results from micro-scale friction measurements is highly stochastic in nature. Details in the measurement data often correspond to singular events that may or may not occur by chance. The data is therefore often shown either in its raw form in order to show and discuss these details, or condensed into a single metric like the coefficient-of-friction, to compare the measurement to others quantitatively.

In this chapter we show a new method for analyzing and visualizing the statistics of stick–slip friction and the evolution of the friction force. As a demonstration, we measure the evolution of the friction force between two sidewalls of a polycrystalline silicon MEMS tribometer with nanonewton resolution during millions of sliding cycles. We will present the measurement data in the form of a new type of friction loop, and with a hexagonal bin plot that represents all two million data points in a single graph. By automatically detecting slip events, we are able to chart the statistics of the stick–slip behavior, extract the maximum static friction force at each contact position and calculate the variability of the static friction force within a single loop. An important result of the new data analysis method is that we are able to determine the real amount of energy dissipation, which turns out to be split into two different contributions: a semi-static contribution, related non-stick–slip sliding and pre-sliding tangential deflections [83], and a dynamic contribution, related to the dissipation of inertial forces during slip motions.

6.2. EXPERIMENTS

The friction experiments were performed with a MEMS tribometer as shown in figure 6.1. The design is based on the Leiden MEMS tribometer [44]. It consists of a normal loader called the loader and a sliding slider. Both the loader and the slider are suspended by folded flexure support springs which act as parallel guides. Each can be moved by a separate electrostatic comb-drive actuator [84]. Friction between the sidewalls of the loader and the slider is generated by moving the slider back and forth, while pushing the loader against it. This is depicted schematically in figure 6.2. The important mechanical characteristics of the tribometer have been summarized in table 6.1.

The device was placed in an environmental chamber, inside which the atmosphere was kept at a temperature of $25 \pm 5\,^{\circ}\mathrm{C}$ and the relative humidity was kept below 5 %. The chamber was fitted with a glass viewport to allow optical access to a Motic PSM-1000 optical microscope mounted above it. The friction sensor was illuminated through the microscope objective by a liquid light-guide coupled Sutter HPX-L5 90 W LED light source, which has the equivalent light output of a 150 W xenon arc lamp. Images were captured

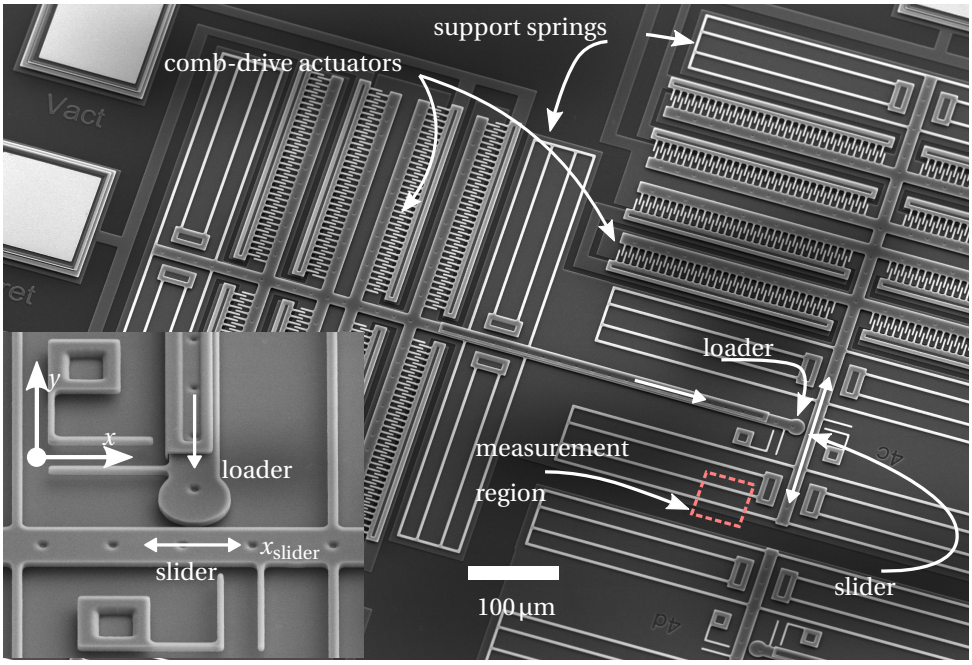

Figure 6.1.: Scanning electron microscope (SEM) micrograph of the MEMS tribometer used in this study. The inset shows a close-up of the loader and the sliding slider. The red-dashed rectangle indicates the area on which the optical microscope was focused to track the position of the slider, x_{slider}.

Table 6.1.: Summary of the geometrical and mechanical properties of the MEMS tribometer shown in figure 6.1.The spring constants were calculated analytically using standard cantilever beam approximations [72]. The sidewall roughness was obtained from an AFM measurement by van Spengen et al. [64], on a device that was fabricated using the same technology [71].

Tribometer property	Value
Suspended structure thickness	2.0 µm
Loader tip radius	10.0 µm
Young's modulus of poly-silicon [71]	158 ± 10 GPa
Loader suspension spring constant, $k_{y,L}$	2.6 ± 0.2 N/m
Slider suspension spring constant, k_s	3.9 ± 0.2 N/m
Sidewall RMS surface roughness [64]	13 ± 3 nm

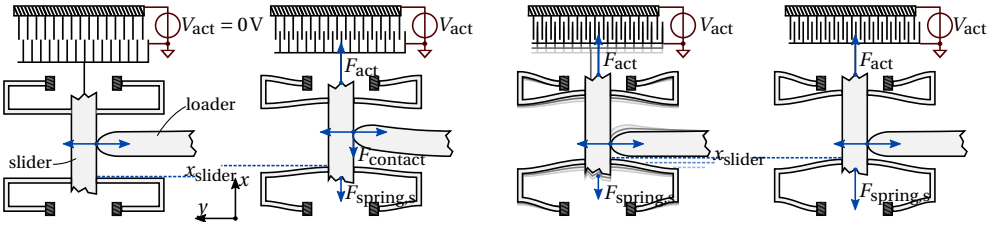

Figure 6.2.: Operation principle of the MEMS tribometer shown in figure 6.1, during the measurement of stick–slip friction (image not to scale, displacements are exaggerated). The blue arrows indicate the forces acting on the slider. The position of the slider is given by x_{slider}. a: Equilibrium, no lateral contact force. b: The comb drive actuator generates a force that pulls on the slider to which the loader is currently stuck. c: the lateral contact force keeping the loader stuck to the slider exceeds the maximum friction force. The loader slips back to its neutral position and the slider moves to a new equilibrium position. d: New equilibrium position, no lateral contact force.

by a IDS uEye 3370CP CMOS camera, mounted on top of the microscope. The entire setup was suspended in bungee cords inside an acoustic isolation chamber mounted on active pneumatic supports, in order to isolate the device from external mechanical and acoustical disturbances.

Throughout the entire experiment, a voltage of 85.0 V was applied to the comb-drive actuators of the loader, which pushes the loader against the slider with a force of 669 ± 51 nN. This force was determined from the voltage–displacement relationship of the loader using the method explained in our previous work on adhesion measurements [54]. Note that the normal force value given here refers only to the externally applied force. Because of adhesion, the actual normal force at that contact is somewhat higher and varies during the experiment.

In order to measure the friction force during a single reciprocating sliding motion, the actuator voltage of the slider actuator was increased from 0 V to 60 V in 1000 steps and back again, while an optical microscope image of the moving slider and a fixed reference was captured at each step. The voltage step size decreases with the square-root of the voltage, to compensate for the quadratic relation between the actuator voltage and the displacement of the slider. This way, the slider moved from 0 nm to 740 nm and back in 2000 equal steps of 0.74 nm. Measuring a single cycle this way takes 36 s. The position of the slider relative to the substrate was determined from the captured images at each voltage step with a resolution of 0.2 nm, using the curve-fitting technique explained in chapter 2.

The entire experiment consisted of two parts. First, 200 consecutive sliding cycles were recorded in order to observe how the pristine surface changes during the first few cycles at a low velocity. Second, the sliding cycles were recorded in blocks of 20 consecutive cycles,

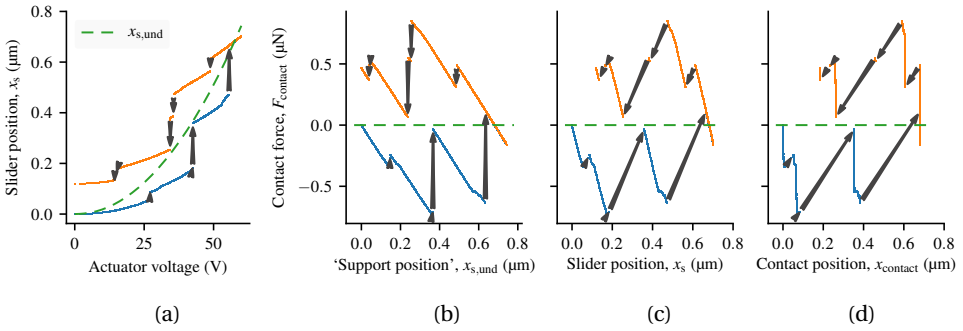

Figure 6.3.: Transformation of the raw displacement measurement data a, to an FFM-style friction loop b, to a MEMS-style friction loop c, to a 'physical' friction loop d. The arrows indicate slip motions. The slopes of the stick-parts of the friction loops in b and c depend on the spring constants of the measurement system, and correct interpretation of their horizontal axes requires knowledge of the measurement system components, which makes them less intuitive to interpret than the friction loop in d.

in between which an exponentially increasing number of sliding cycles was performed at an average velocity of 50 µm/s. The total number of sliding cycles was 2 249 827.

6.3. RESULTS

The resulting dataset consists of 1000 sliding cycles of 2000 measurement records each. Each record contains the voltage applied to the slider comb-drive actuators, and the measured slider displacement x_{slider} relative to the substrate. In section 6.3.1, we show how to transform these raw values into the lateral force at the contact, $F_{contact}$, and the position at which the loader touches the slider, $x_{contact}$. We then study the evolution of the friction force and its distribution across the sliding track qualitatively: by analyzing the individual friction loops in section 6.3.2, and by introducing a new visualization method that displays many aspects of all recorded friction loops in a single plot in section 6.3.3. In section 6.3.4 we show how to identify individual slip events and we discuss their statistics. Finally, in section 6.3.5 we use this information to distinguish between two types of frictional energy dissipation.

6.3.1. CALCULATION OF THE FORCE AND CONTACT POSITION FROM THE RAW DATA

Figure 6.3a shows an example of a single measured friction cycle in its rawest form: the measured slider position x_{slider} versus the applied actuator voltage. The dashed green line indicates the 'undisturbed motion' $x_{s,und}$: the displacement of the slider when it is not in contact with the loader. The blue data points correspond to the measured slider

positions during the forward sliding motion, and the orange data points correspond to the measurement slider positions during the backward sliding motion. At the continuous parts of the lines, the slider is stuck to the loader. The reason that stick-sections are not perfectly horizontal, is that the slider can still move while being stuck, due to the finite bending stiffness of the loader. The arrows connecting the discontinuities indicate slip events. These are too fast for our measurement system to capture. The data points and the arrows together constitute a hysteresis loop commonly referred to as a friction loop. Because the force of friction always acts in the direction opposite to the motion of the slider, $x_{\text{slider}} \leq x_{\text{s,und}}$ during the forward motion, and $x_{\text{slider}} \geq x_{\text{s,und}}$ during the backward motion.

To transform the voltage–displacement curve of figure 6.3a to a force–displacement curve, we first need to obtain a mathematical relationship between the measured displacement x_{slider}, the actuator voltage V_{act} and the contact force F_{contact}. A schematic representation of the operation of the tribometer is shown in figure 6.2. The black arrows indicate the forces acting on the slider. The force balance of all forces acting in the x-direction (the vertical direction in figure 6.2) is given by:

$$\Sigma F_x = -F_{\text{act}} + F_{\text{contact}} + F_{\text{spring,s}} = m \cdot \frac{\mathrm{d}^2 x}{\mathrm{d}t^2}, \tag{6.1}$$

where F_{act} is the force exerted by the slider's actuator comb drives, F_{contact} is the contact exerted on the slider by the loader, and $F_{\text{spring,s}}$ is the restoring spring force of the slider support springs.

When the device is at rest, $\frac{\mathrm{d}^2 x}{\mathrm{d}t^2} = 0$, so we can write for the actuator force F_{act}:

$$F_{\text{act}} = F_{\text{contact}} + F_{\text{spring,s}} \tag{6.2}$$

$$= F_{\text{contact}} + k_{\text{s}} \cdot x_{\text{slider}}, \tag{6.3}$$

where k_{s} is the spring constant of the slider support springs.

We do not actually have to know the value of F_{act} to obtain F_{contact}. Instead, we can calculate F_{contact} for every value of V_{act} from the difference between the actual displacement of the slider x_{slider}, and the undisturbed displacement of the slider, $x_{\text{s,und}}$. When $F_{\text{contact}} = 0$, $x_{\text{slider}} = x_{\text{s,und}}$ by definition. So:

$$F_{\text{act}} = k_{\text{s}} \cdot x_{\text{s,und}} \qquad \text{for } F_{\text{contact}} = 0 \tag{6.4}$$

substitute (6.3) for F_{act}:

$$k_{\text{s}} \cdot x_{\text{slider}} + F_{\text{contact}} = k_{\text{s}} \cdot x_{\text{s,und}} \tag{6.5}$$

rearrange the terms:

$$F_{\text{contact}} = k_{\text{s}} \cdot \left(x_{\text{s,und}} - x_{\text{slider}} \right). \tag{6.6}$$

We use equation (6.6) to calculate the contact force from our measured values of x_{slider}.

In AFM-based friction force microscopy, the contact force is usually plotted versus the cantilever support position. This quantity is very similar to our 'undisturbed motion' and

can be explained using exactly the same wording as used above: it represents the position at which the cantilever tip would have been, if the contact force had been zero. Because friction force microscopy is older than MEMS tribology, MEMS friction loops are often plotted the FFM way, which is shown in figure 6.3b. The slope of the stick-parts of the plot depends on the spring constants of the system. Figure 6.4 shows a mechanical lumped element model that describes the situation in which the loader is stuck to the slider for $F_{act} \neq 0$ (Figure 6.2b). From the lumped element model we know the relation between the slider displacement, x_{slider}, the actuator force, F_{act}, the spring constant of the slider's support springs, k_s, and the spring constant that corresponds to the lateral bending mode of the loader, k_L:

$$x_{slider} = F_{act} \cdot \frac{1}{k_L + k_s} \tag{6.7}$$

substitute (6.4) for F_{act}, and (6.6) for x_{slider}

$$x_{s,und} - \frac{F_{contact}}{k_s} \equiv x_{s,und} \cdot \frac{k_s}{k_L + k_s} \tag{6.8}$$

rearrange the terms:

$$F_{contact} \equiv x_{s,und} \cdot \frac{k_L \cdot k_s}{k_L + k_s} \tag{6.9}$$

finally differentiate with respect to $x_{s,und}$:

$$\frac{\partial F_{contact}}{\partial x_{s,und}} = \frac{k_L \cdot k_s}{k_L + k_s} \tag{6.10}$$

This means that the shape of the friction loops depends strongly on the geometry of the measurement system, which makes them hard to interpret.

A more 'pure' way of plotting MEMS friction loops would be to place the measured slider position x_{slider} on the horizontal axis, as is shown in figure 6.3c. The slope of the stick-parts of the plot now only depends on k_L, which we can prove by substituting (6.3) for

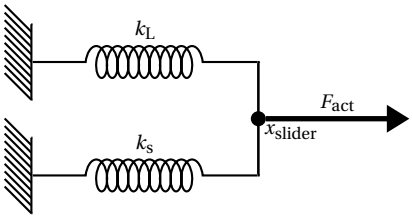

Figure 6.4.: Mechanical lumped element model of the slider and loader of the MEMS tribometer shown in figure 6.1. It shows the equivalent lateral springs constants and forces acting on the slider while the loader is stuck to the slider due to static friction. This model corresponds to the state of the tribometer as shown in figure 6.2b. When the loader is stuck against the slider, it acts as an additional spring in parallel to the folded flexure suspension.

F_{act} in (6.7):

$$x_{slider} = (F_{contact} + k_s \cdot x_{slider}) \cdot \frac{1}{k_L + k_s} \tag{6.11}$$

simplifying:

$$F_{contact} = x_{slider} \cdot (k_L + \cancel{k_s}) - \cancel{k_s \cdot x_{slider}} \tag{6.12}$$

and differentiating with respect to x_{slider}:

$$\frac{\partial F_{contact}}{\partial x_{slider}} = k_L \tag{6.13}$$

This means that k_L can now be calculated from the linear slopes of the friction loops, which allows for a third type of friction loop to be plotted: the force versus the actual contact position $x_{contact}$, where $x_{contact}$ is calculated from x_{slider} and k_L using:

$$x_{contact} = x_{slider} - \frac{F_{contact}}{k_L}. \tag{6.14}$$

This type of friction loop is shown in figure 6.3d. We will use it throughout the rest of this chapter because it offers several important advantages over an FFM-style friction loop. First, its interpretation requires no knowledge of the geometry and components of the measurement system. Second, but more importantly, the surface area under any continuous section of the graph directly corresponds to the energy that was dissipated at that specific contact range. In an FFM-style friction loop on the other hand, the surface area under any section of the graph corresponds to the potential energy stored in or gained from the support springs. Although it is possible to extract the dissipated energy at every contact position from an FFM-style loop indirectly, doing so is much less intuitive.

6.3.2. RAW FRICTION LOOPS

Several measured friction loops of the experiment are shown in figure 6.5. As promised, we have plotted the lateral contact force $F_{contact}$ on the vertical axis versus the contact position $x_{contact}$ on the horizontal axis.

Stick–slip motion measurements, such as this one, produce friction loops that consist of two contributions: continuous 'stick parts', where the slider is stuck to the loader, and discontinuous 'slip parts', where the slider slips.

The black arrows are drawn between the start and end points of slip events. A slip event occurs when the actuator force F_{act} becomes greater than the static friction force, the contact is broken, and the slider moves to a new position where it gets stuck. Note that we do not have any measurements while the slider is slipping, because our measurement method is to slow to capture the slider while it is in motion. At every measurement point, the slider is stationary.

During the first few cycles, the slider is stuck most of the time. As more cycles elapse, the friction force decreases slightly, and a higher number of slip events occur. After 2 million cycles, the surface has become smooth, and the friction loops are almost continuous.

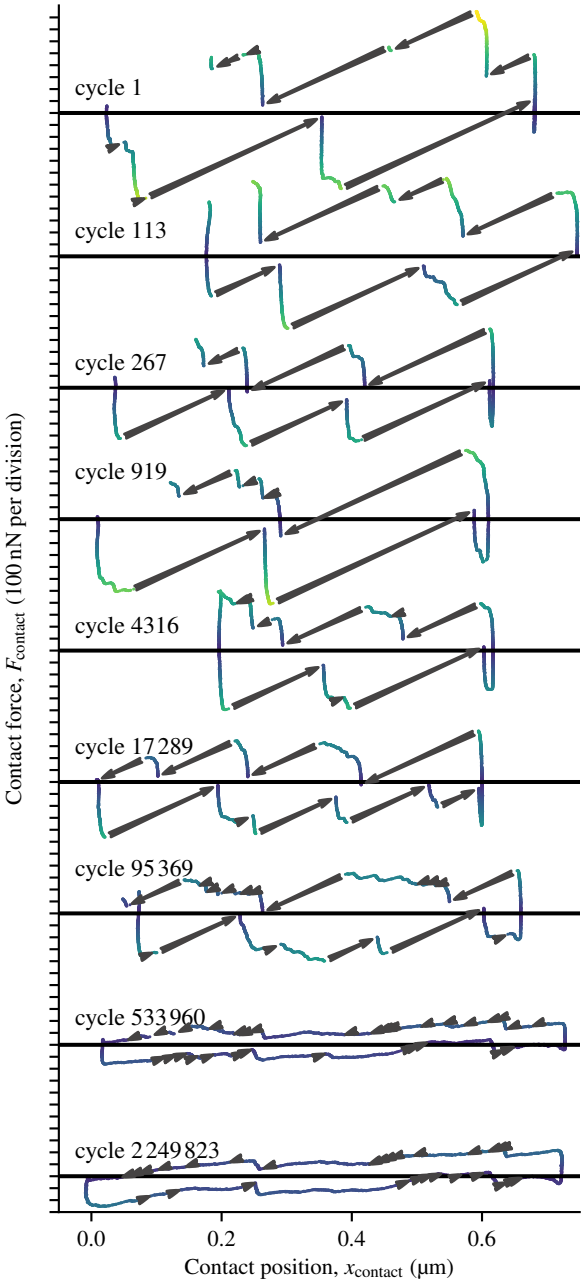

Figure 6.5.: A number of friction loops recorded after an increasing number of contact cycles (first cycle on top). The arrows indicate slip motion events. The friction loops are displayed by plotting the lateral force versus the contact position $x_{contact}$. The color of the data points is proportional to the magnitude of the friction force, and corresponds to the color scale used in figure 6.6.

6.3.3. HEXAGONAL BIN PLOTS

Studying graphical representations of all 2000 recorded friction loops is highly informative, because it allows us to follow how the positions at which the slider sticks change from cycle to cycle. Unfortunately, printed formats only allows for a few friction loops to be displayed.

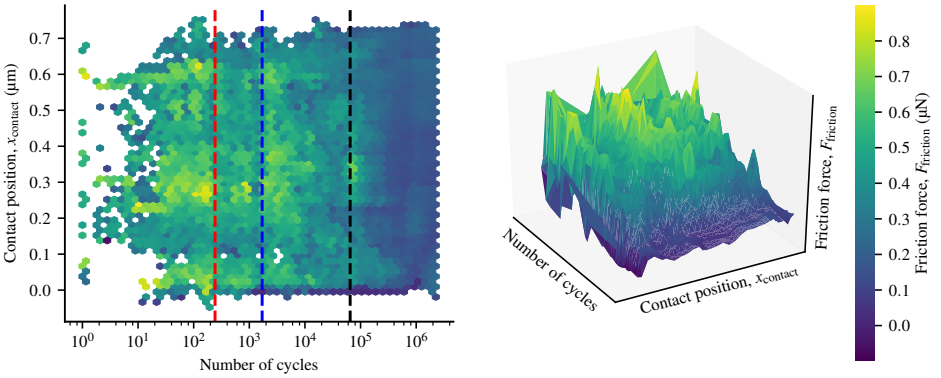

Figure 6.6.: Hexagonal bin plot of the maximum friction force measured at every contact position of all friction loops. The color of each bin corresponds to the maximum value of F_{friction}. The 3D surface plot has been constructed from the bin values and positions. We have used matplotlib's [85] perceptually uniform colormap 'viridis'.

However, many details of the friction loop shape can be conveyed by using an hexagonal bin plot [86, 87] as shown in figure 6.6. The graph shows the slider position x_{contact} on the vertical axis versus the number of elapsed cycles n_{cycles} on the horizontal axis.

The hexagonal bin plot is constructed in the following way. First, the graph area is divided into a honeycomb lattice of hexagonal bins, on top of which all 1.8 million measurement records of $\{n_{\text{cycles}}, x_{\text{contact}}, F_{\text{friction}}\}$ are scattered. For each bin, a single scalar value is now calculated from the data points inside it. This value determines the color of the bin. In principle it can be any metric that describes the data it contains, such as the mean, minimum, or maximum value, or even simply the value count. In this case, the bin color corresponds to the maximum value of F_{friction}. The plot can be understood as a collection of all measured friction loops 'viewed from the top'. It main strength is that it shows the evolution of the friction force magnitude, and its distribution across the surface in a single plot.

In the first part of the experiment, in which 200 cycles were measured consecutively, there are three dominant stick locations, at 0 nm, 250 nm and 600 nm. During the first 10 cycles, the slider mostly sticks close to the last two locations, but from 20 cycles onward the slider occasionally sticks at other locations as well. Immediately after the start of the second part of the experiment, in which fast, unmeasured cycles are executed between

the measurements, the dominant stick locations are smoothened across the entire motion range. After 1700 cycles, the overall stick force suddenly increases across the entire surface. The force gradually decreases again until 65 000 cycles have elapsed and a new friction force maximum occurs. From this point onward, the friction loops become very smooth and almost continuous.

We have marked the boundaries of the regions in our experiment in every graph in this chapter using vertical dashed lines. Their meaning is summarized in table 6.2.

Table 6.2.: Overview of all cycle numbers that mark a significant change in the experimental results. All of these cycle number are illustrated in the plots in this chapter using colored dashed lines.

line	cycles	event
- - - -	200	The experiment mode changes from slow to fast
- - - -	1700	Overall increase in stick force
- - - -	65 000	Start of overall smoothening of friction loops

6.3.4. STICK–SLIP STATISTICS

Slip events show up in the friction loops as discrete jumps, where the contact position increases more than the constant step size of the undisturbed motion. We automatically labeled pairs of data-records $\{p_n, p_{n+1}\}$ as stick–slip pairs when the following conditions are true simultaneously:

$$D \cdot (x_{\text{contact},n+1} - x_{\text{contact},n}) > 2 \cdot \Delta x_{\text{und}} \tag{6.15}$$

$$-D \cdot (F_{\text{contact,n+1}} - F_{\text{contact,n}}) > 2 \cdot k_{\text{s}} \cdot \Delta x_{\text{und}} \tag{6.16}$$

where $D = 1$ if the actuator voltage increases (forward sliding direction) and $D = -1$ if the actuator voltage decreases (backward sliding direction). $\Delta x_{\text{und}} = 0.74\,\text{nm}$ is the constant displacement step size as measured in the undisturbed motion curves. This allowed us to give each 'point of stick' (the continuous parts of the friction loops) and each stick–slip point pair (the arrows) a unique label, analyze their individual properties and study how their statistics develop as a function of the number of elapsed cycles.

When using a simple thresholding algorithm to detect steps in data, as we are doing here, the smallest detectable step is determined by the noise level of the data. In our case, the RMS displacement noise is and exceptionally low $\sigma_x = 0.2\,\text{nm}$. As a rule of thumb, a safe detection threshold is often taken as $6\sigma = 1.2\,\text{nm}$. This is less than twice the minimum displacement step of $2 \cdot \Delta x_{\text{und}} = 1.48\,\text{nm}$ which we are trying to detect, so our thresholding algorithm will yield reliable results for this dataset. For more noisy data this simple approach will not work, and a more robust step detection algorithm should be used, such as the one discussed by Yao and Li [88].

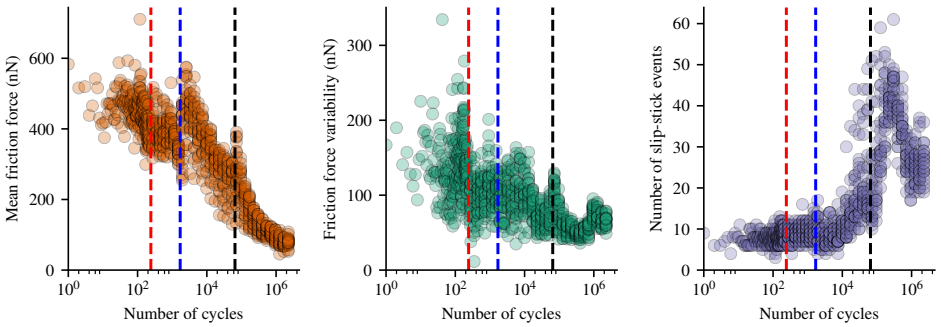

(a) (b) (c)

Figure 6.7.: Scalar quantifiers obtained from the individual friction loops plotted versus the total number of elapsed cycles. a: The mean friction force per cycle, b: the standard deviation of the measured friction forces per cycle, and c: the total number of slip events per cycle.

The maximum absolute value of the lateral force at each point of stick is the static friction force at that specific location. Figure 6.7 shows the mean of the friction forces measured per cycle, their variability, and the total number of slip events in each measured cycle.

Figure 6.8 shows evolution and spread of the coefficient of (static) friction $\mu_{f,s}$. Each data point is obtained by dividing the maximum lateral force before a slip occurs by the externally applied normal pushing force of $F_N = 669 \pm 51$ nN. During the first $\sim 10^5$ cycles, the mean coefficient of friction per cycle varied roughly in the range between the values of the static and dynamic coefficients-of-friction for glass–glass contacts of 0.94 and 0.4 respectively. After $\sim 10^5$ cycles the coefficient of friction decreased down to 0.12. The variability of the friction coefficient follows the same trend as the mean friction force shown in figure 6.7b.

6.3.5. SEMI-STATICALLY AND DYNAMICALLY DISSIPATED ENERGY

Our friction loops consist of two contributions: continuous 'stick parts', where the slider is stuck to the loader, and discontinuous 'slip parts', where the slider slips from one stick part to the next. When we calculate the dissipated energy from a friction loop, we have to treat these two contributions separately. We will refer to the energy dissipated while the slider is stuck as the semi-statically dissipated energy, and to the energy dissipated during the slip events as the dynamically dissipated energy.

We choose the term 'semi-static' because it refers to the parts of the measurement where the slider is stationary, and no inertia is involved. However, every dissipation process is inherently dynamic, not static, which is why we have added the 'semi'-prefix. The physical mechanisms by which semi-static dissipation occurs, may involve e.g. small contact deformations and plastic yield of the contacting surfaces.

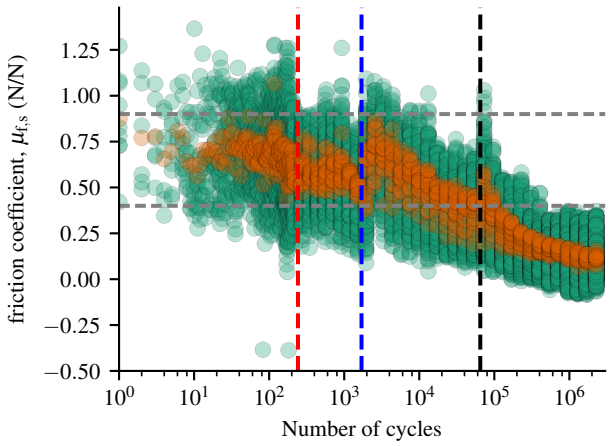

Figure 6.8.: The coefficient of static friction: the maximum friction force before a slip occurred divided by the externally applied normal force. To provide a macro-scale frame of reference for the magnitude of these values, the horizontal dashed light gray lines indicate the empirical values of the static (0.94) and dynamic (0.4) coefficients-of-friction for bulk glass–glass contacts [89].

The term 'dynamic' refers to the fact that the underlying dissipation mechanisms are related to the dynamic behavior of the slider. While the slider is slipping, it may slide viscously and break weaker asperities along its path. When it finally gets stuck again, it will dissipate the remainder of its kinetic energy on impact.

The calculation of both energy contributions is illustrated in figure 6.9a. We obtain the semi-statically dissipated energy by integrating F_{friction} with respect to x_{contact} between the start and end of a single stick part:

$$E_{\text{static}} = \int_{x_{\text{start}}}^{x_{\text{end}}} F_{\text{friction}} \, \mathrm{d}x_{\text{contact}} \,, \tag{6.17}$$

where E_{static} is the semi-statically dissipated energy.

The dynamically dissipated energy cannot be found by a similar integration method, because we do not have any position measurements during the slip motion itself. We only know where the slider starts slipping, and were it gets stuck again. However, the energy dissipated in a slip motion must be exactly equal to the decrease in potential energy stored in the slider support springs, regardless of exactly when and by which mechanism the energy is converted to heat. This means that we can calculate the energy dissipated in a single slip event from the difference between the spring energy E_{spring} just before, and immediately after the slip motion. The energy stored in the springs at every measured force is given by

$$E_{\text{spring}} = \frac{1}{2}\left(\frac{1}{k_{\text{ram}}} + \frac{1}{k_{\text{s}}}\right) {F_{\text{friction}}}^2, \tag{6.18}$$

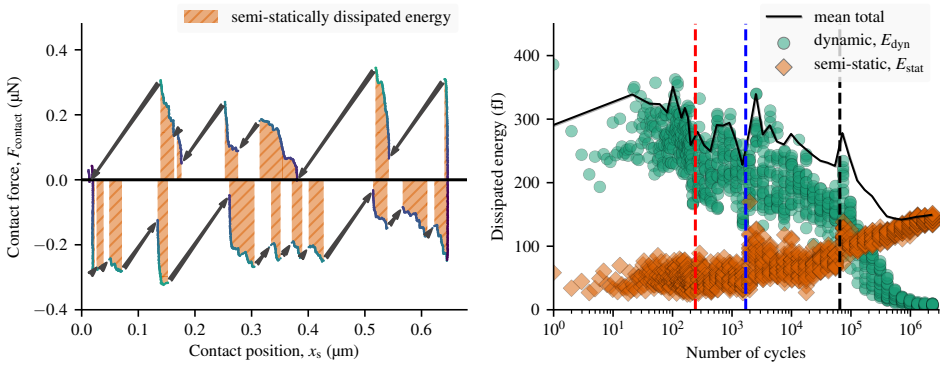

(a) (b)

Figure 6.9.: a: Illustration of how the semi-statically dissipated energy and the dynamically dissipated energy are obtained from a friction loop. The semi-statically dissipated energy is the surface area below the continuous 'stick parts' of the friction loop. The dynamic energy is the surface area of the right-angled triangle defined by the slip arrows. This friction loop was recorded after 53818 sliding cycles. It was selected because its semi-statically dissipated energy roughly equals its dynamically dissipated energy. b: The dissipated energy versus the number of elapsed sliding cycles. The dynamic energy is the energy dissipated in slip motion events. The semi-statically dissipated energy is the energy dissipates while the loader is stuck but the contact yields somewhat. At low cycle numbers most energy is dissipated in the large slip events (see figure 6.5). At very high cycle numbers, the friction loops have become very smooth, and almost all energy is dissipated semi-statically.

so the dynamic energy is:

$$E_{\text{dynamic}} = E_{\text{spring}}|_{x_{\text{before}}} - E_{\text{spring}}|_{x_{\text{after}}} \tag{6.19}$$

where E_{dynamic} is the dynamically dissipated energy of the slip motion.

Note that the dynamic energy is not equal to the surface area below the arrows in the friction loop.[1]

Figure 6.9b shows the semi-statically dissipated energy and the dynamically dissipated energy of each cycle, as well as the mean of their sum, versus the total number of elapsed cycles. In the first part of the experiment, most energy is dissipated dynamically, with a large variability. After the experimental mode is changed at 200 elapsed cycles, the dynamic energy decreases but the semi-static energy remains constant. After 1700 cycles, the dynamic part of the dissipated energy decreases, while the semi-static energy starts to increase monotonically. After 65 000 cycles, the dynamically dissipated energy quickly decreases to zero. The semi-static energy however, keeps increases monotonically, until it finally starts to flatten off after one million cycles.

6.4. DISCUSSION

Our visualizations of the individual friction loops in figure 6.6, the aggregated quantities shown in figure 6.7 and the dissipated energy, together paint an indirect, yet lively picture of the events that occurred at the contact.

6.4.1. PHYSICAL INTERPRETATION OF THE RESULTS

During the first part of the experiment the slider moves over the surface in several large jumps. The locations at which the slider sticks do not change much. After the experiment changes, high speed sliding motions are executed between the measured cycles, and the surface changes instantly. This is because the inertia of the moving slider is now large enough to break the highest interlocking asperities, which has a noticeable effect on the magnitude of the friction force (Figure 6.7a), the dynamically dissipated energy, and the friction coefficient. Because these surface changes happen during the fast cycles that are not measured, the surface remains relatively stable during the recorded measurement blocks where the slider inertia does not play a role and the available forces are not large enough to modify the contact significantly. This is confirmed by an sharp decrease of the force variability (Figure 6.7b) after the measurement type changes.

After 1700 cycles, the breakup of a large third body or asperity significantly increases the mean friction force and the friction coefficient, which causes a sharp increase in the amount of semi-statically dissipated energy. From this point onward, the total number

[1] We got this wrong initially, and stated that the dynamically dissipated energy should be equal to the surface area of the right-angled triangles defined by the slip arrows, excluding the square between the lowest part of the arrow and the x-axis. We rectified this mistake in a published corrigendum [76].

of slip events gradually increases while the friction force, friction coefficient and the dissipated energy decrease monotonically.

Around 65 000 cycles we observe the formation and destruction of an obstacle near the center of the sliding track, which is indicated by a peak in the mean friction force, the coefficient of friction, the force variability, and the total dissipated energy. A remarkable transition in friction behavior follows. The amount of slip events almost triples, yet the dynamically dissipated energy quickly approaches zero. The semi-statically dissipated energy, which had been rising steadily since the start of the experiment, becomes the dominant energy dissipation mode.

The friction loops are now almost completely smooth, which indicates that the previously dominant stick–slip behavior has changed to normal sliding. However, the shape of the friction loops has become highly asymmetric. For both directions of motion, the friction force gradually decreases when x_{contact} is near the edge of the sliding track. In some cases it even becomes negative, indicating that at certain positions, the slider is being dragged along rather than being held back. Our hypothesis for explaining this behavior, is that a small amount of viscous slurry is formed at the contact, which consists of the pulverized remains of SiO_2 debris, carbon contaminants, and a small amount of adsorbed water. A small excess of the slurry at the far ends of the sliding track will pull on the slider by capillary action, which accounts for the observed negative friction forces. The excess of slurry increases capillary adhesion, which in turn increases the local static friction force. This accounts for the fact that the slider sticks at the far ends of the sliding track after the direction of motion is reversed. The slurry will also introduce some visco-elastic behavior along the length of the sliding track, and may in part be responsible for the smooth sliding behavior during the final stages of the experiment.

The steady rise of the semi-static energy after 1700 cycles, may be caused by a gradual increase of the contact area due to flattening. This would increase the adhesion forces acting between the contacting surfaces, which in turn increases the friction force, as well as the amount of dissipated energy.

6.5. CONCLUSION

We have successfully measured the evolution of the static friction force between two contacting silicon MEMS sidewalls with a resolution of 0.6 nN. By compensating for the in-plane bending spring constant of the loader, we were able to obtain the friction force as a function of the real point of contact rather than the equivalent of the cantilever support position of an FFM measurement. This results in a more intuitive type of friction loop, because it does not require any knowledge of the measurement system with which the data was acquired.

Hexagonal bin plots are an effective visualization method for studying the evolution of the friction force in a reciprocating sliding motion as a function of any variable. Figure 6.6 gives a clear qualitative description of how the shape of the friction loop changes as a function of the total number of elapsed friction cycles.

The identification of individual slip events allowed us to split each friction loop into sections of stick and sections of slip, and we obtained two distinct mechanisms by which energy is dissipated. The semi-statically dissipated energy is related to the deformation of the contact by a variety of physical mechanisms, before actual sliding occurs. The dynamically dissipated energy is related to the slider dynamics during the micro-scale slip motions and to the impact when the slider gets stuck again.

We have measured the variability and drift of the static friction coefficient (Figure 6.8), the mean static friction force (Figure 6.7a-b), and the number of slip events (Figure 6.7c) as a function of the total number of elapsed cycles. The coefficient of friction is not an adequate metric by itself to describe the characteristics of friction in MEMS, because of its large variability with each friction cycle.

After a large number of sliding cycles the friction loop shapes remain the same. The semi-statically dissipated energy gradually increases throughout the experiment and levels off after one million cycles, indicating that the 'run-in' of the surfaces is complete. The dynamically dissipated energy is more variable than the semi-statically dissipated energy and decreases throughout the experiment, and eventually becomes zero when the stick–slip behavior of the contact has changed to continuous sliding.

The simultaneous existence of these two energy contributions in the same order of magnitude appears to be unique to the meso-scale, and to its characteristic multi-asperity contact. It would be of great value to study how these energies behave in meso-scale and atomic scale friction force microscopy measurements under well controlled circumstances. The ability to disentangle the dissipated energy into two physically different contributions will enable more accurate conclusions to be drawn from all friction loop measurements.

III

Conclusion

"In every branch of knowledge the progress is proportional to the amount of facts on which to build, and therefore to the facility of obtaining data."

(James Clerck Maxwell [90])

7

CONCLUSIONS AND DISCUSSION

This thesis has presented a method for measuring friction and adhesion in MEMS. In part I we have demonstrated an optical measurement technique for measuring sub-nanometer displacements and sub-nanonewton forces in MEMS. In part II we applied this technique to measure adhesion forces and friction forces between the etched sidewalls of MEMS tribometers with an unprecedented resolution. These are the main conclusions:

- Optical microscopy can be used to measure adhesion and friction forces between MEMS sidewalls with sub-atomic position resolution.
- The adhesion force between polycrystalline silicon MEMS sidewalls does not stabilize, even after millions of repeated contacts.
- The energy dissipated due to friction can be separated into two independent contributions: the semi-statically dissipated energy, and the dynamically dissipated energy.
- Hexagonal bin plots are an effective way to visualize the evolution of the friction force.

We will now discuss these in more detail, and show that we have achieved our main goal: to develop and test a method for measuring atomic-scale contact mechanical phenomena in MEMS, and meso-scale systems in general.

7.1. OPTICAL DISPLACEMENT MEASUREMENTS

In chapter 2 we demonstrated a measurement technique based on optical microscopy and curve-fitting. We have achieved an in-plane displacement resolution of 64 pm by fitting a shifted spline function through the intensity profile of a silicon beam that was imaged with an optical microscope and a CCD camera. The displacement noise is dominated by photon shot noise which is the limiting factor for the resolution of the measurement. The effect of photon shot noise can be decreased by increasing the intensity of the light source,

increasing the contrast, averaging or binning multiple lines, or by averaging multiple images.

If the width of the image of the moving feature is much larger than the width of a single camera pixel, the amount of displacement noise depends only on the total amount of light received, and on the image contrast [45]. The lower limit of the resolution is determined exclusively by the intended frame rate of the measurement. The requirements for the resolution and frame rate of a displacement measurement are determined by the application. Whether or not the intended combination of resolution and frame rate can be achieved with a given measurement setup is determined by a number of factors related to the hardware used:

- The maximum frame rate of the camera. This is determined by the read-out frequency of the sensor and by the speed of the camera interface.
- The pixel width of the camera's imaging sensor. Larger pixels capture more light than smaller ones in the same amount of time.
- The amount of reflected light picked up by the microscope and transmitted to the camera. This is determined only the numerical aperture of the microscope objectives and by the brightness of the light source.
- The amount of stray light picked up by the microscope and transmitted to the camera. This is determined by the depth of field of the microscope objective, which in turn depends on the objective's magnification and on its numerical aperture. The larger the numerical aperture of the objective and the larger the magnification, the smaller the depth of field.

The noise figure of our measurement setup was found to be $35.3\,\mathrm{pm}/\sqrt{\mathrm{Hz}}$ for the slow measurements performed with a CCD camera, and $36\,\mathrm{pm}/\sqrt{\mathrm{Hz}}$ when performed with a high-speed line scan camera. This proves once more that the shot noise of the light is responsible for the noise floor in these experiments, not the properties of the camera.

When building a new measurement setup, this list above can be translated loosely into "buy the most expensive hardware", which is more or less valid for the microscope. When it comes to selecting a camera, however, paying extra for more pixels on the same sensor area does not result in a higher displacement measurement resolution. Large pixels and a fast readout are always to be preferred to a high pixel density.

The measurement resolution can be further improved by optimizing the following properties of the MEMS device under test:

- The brightness of the moving features. This is determined by their width, and by the reflectivity of the material they are made of. Every single feature should be a few times larger than ~0.5 µm: the tiniest feature size resolvable with visible light. By imaging a pattern of N identical features, the eventual resolution is increased by a factor $\sqrt{N}$.

- The contrast of the moving features compared to the background. This is determined by the reflectivity of the surface below the moving feature, and by the out of plane distance of the feature's surface to the substrate below it.

In all of the work presented in this thesis, we have used MEMS tribometers based on the Leiden MEMS tribometer [91], without adjusting their designs to improve the measurement resolution according to the recommendations listed above. We typically only imaged a single beam of the parallel guide suspension of the tribometer, instead of a grating structure optimized for use as tracking target in optical measurements.

7.2. ADHESION IN MEMS

Because of the sub-nanonewton force resolution of our measurement technique, we were able to observe the adhesion force between polycrystalline silicon MEMS sidewalls with unprecedented detail. For the first time, we obtained a quantitative insight in how MEMS contacts evolve over a large number of contact cycles under low force and low humidity conditions. The results in chapter 4 clearly show the large variations in the contact mechanics of 'identical' MEMS devices. Local variations in surface roughness the resulting variations of the local contact pressure and capillary condensation play a major role in determining the strength and evolution of the adhesive force in these contacts.

Although the cycle-to-cycle variability of the adhesion force decreases after ~ 100 cycles, the gradual change of the adhesion force as a result of run-in does not stabilize, even after 3 million cycles. This drift of the adhesion force during millions of cycles is comparable in magnitude to the initial drift during run-in. It is therefore possible to predict the long-term behavior of the adhesive contacts in MEMS devices, based on an experiment considerably shorter than the intended life-span of the device.

At higher levels of relative humidity ($> 50\,\%_{RH}$), the behavior of the adhesion force will be dominated by capillary condensation, at which point the conclusions of this work are less relevant. Gkouzou *et al.* [53] demonstrated that the adhesion force will vary even more than it already does at low humidity, and that the amount of variability depends strongly on temperature in a non-linear fashion.

The adhesion measurements presented in appendix 4.A and chapter 5 show that after a large number of contacts, snap-in and snap-off are not always purely instantaneous. In our measurements, this results in non-zero displacements during contact. We called this effect Inelastic Contact Deformation (ICD), because the forward and backward displacement curves do not overlap. We identified three different reasons why ICD may occur:

- Lateral sliding. in case contact is made on the slope of an asperity, the contact will slide sideways and settle into a more stable position when the normal force is increased. Before snap-off occurs, the contact will slide back to its initial position before snap-off occurs.

- Forming and breaking of covalent bonds. The force required to break a single bond between two SiO_2 molecules is in the order of ~2.9 nN [22]. The lowest force resolution we have achieved in our adhesion experiments was 0.5 nN, which is well below the force required to separate a single covalent bond between two SiO_2 molecules. However, this value depends on the angle under which a force is applied to it and the total number of covalent bonds between the contacting surfaces varies. The breaking of covalent bonds does not show up as a single instantaneous step of fixed size, but as a gradual pullback before snap-off. Indeed, we have observed gradual pullback in all long-running adhesion experiments. In each case, the magnitude and variability of the effect increase rapidly, after ~10^5 cycles. This is consistent with the fact that the surfaces first need to undergo a certain amount of stress and damage, before vacancies for covalent bonds are created. The formation of chemical bonds does not result in deformations of the contact after snap-in.
- Viscoelastic deformation. this effect was present only in two experiments, and it only occurs after ~10^6 contact cycles; well after the phase of forming and breaking of covalent bonds. After snap-in, the contact deforms monotonously with the increasing normal force by as much as 15 nm, but only after the contact has had 15 ± 5 s to 'relax'. The effect is much less pronounced between subsequent contacts that occur within seconds from each other. This dependence on a relaxation time, proves that the effect is dynamic. We speculate it to be caused by the *in situ* tribo-synthesis of a viscous, silicone-like compound that may form on the surface due to chemical reactions between hydrocarbon contaminants, adsorbed water and SiO_2 wear debris.

We will discuss several additional experiments required to confirm these hypotheses in chapter 8.

7.3. FRICTION IN MEMS

We have successfully measured the evolution of the static friction force due to wear between two contacting silicon MEMS sidewalls. The achieved resolution was 0.6 nN. By compensating for the in-plane bending spring constant of the loader, we were able to obtain the friction force as a function of the real point of contact rather than the equivalent of the cantilever support position of an FFM measurement. This produces a friction loop of which the interpretation is more straightforward.

Hexagonal bin-plots are an effective means to visualize the evolution of the friction force at every point of contact during a friction experiment of many repeating sliding motions. Figure 6.6 gives a clear qualitative description of how the shape of the friction loop changes as a function of the total number of elapsed friction cycles.

We have measured the variability and drift of the static friction coefficient (Figure 6.8), the mean static friction force (Figure 6.7a-b), and the number of slip events (Figure 6.7c) as a function of the total number of elapsed cycles. The coefficient of friction is not an

adequate metric by itself to describe the characteristics of friction in MEMS, because of its large variability with each friction cycle.

The identification of individual slip events allowed us to split each friction loop into sections of stick and sections of slip, and we obtained two distinct mechanisms by which energy is dissipated. The semi-statically dissipated energy is related to the deformation of the contact by a variety of physical mechanisms, before actual sliding occurs. The dynamically dissipated energy is related to the slider dynamics during the micro-scale slip motions and to the impact when the slider gets stuck again.

After a large number of sliding cycles the friction loop shapes remain the same. The semi-statically dissipated energy gradually increases throughout the experiment and levels off after one million cycles, indicating that the 'run-in' of the surfaces is complete. The dynamically dissipated energy is more variable than the semi-statically dissipated energy. It decreases throughout the experiment, and eventually approaches zero when the stick–slip behavior of the contact has changed to continuous sliding.

The ability to disentangle the dissipated energy into two physically different contributions will enable more accurate conclusions to be drawn from all friction loop measurements. Friction data obtained by FFM is typically displayed as the lateral force versus the position of the cantilever support, because the position of the tip is not measured directly. However, the position of the tip can be calculated from the support position using

$$x_{\text{tip}} = x_{\text{support}} - \frac{F}{k_{\text{torsion}}}, \tag{7.1}$$

where k_{torsion} is the effective linear spring constant of the FFM cantilever at the tip in N/m. The value of k_{torsion} can be calculated from the slopes of the stick-parts of the measured friction loops, or from the length of tip and the torsional stiffness of the cantilever.

In this work we have separated the dissipated energy into two contributions. However, we are yet to understand which forces exactly contribute the most to energy dissipation. In some cases it is clear that the friction or adhesion force is dominated by capillary effects, but this is mostly based on a rough qualitative assessment: if the force is high, it is dominated by capillary effects, if it is 'low', it is dominated by Van der Waals. In both cases, there will also be a contribution of covalent bonds between the asperities of the contacting surfaces.

For all measurements we reported on, a good experimental setup, combined with clever post-processing is required to unearth the information present in the dataset. The work presented in this thesis shows that it pays to go much further in terms of computational analysis of the measured data than is usually done in the field of MEMS. Further development of the methods presented in this thesis will lead to a better fundamental understanding of the contact mechanics of MEMS, and of meso-scale systems in general.

8

FUTURE WORK

In section 7.1 we have formulated a set of guidelines to maximize the resolution and framerate for in-plane optical displacement measurements based on curve fitting. We will now recommend several improvements to the measurement system in order to realize its full potential. We will also describe several new friction and adhesion experiments, designed to answer research questions that remain open.

The atomic scale detail of our measurement results raises many fundamental questions about the behavior of meso-scale contacts. The reason why it is so hard to run an experiment with repeatable results, is that we still only have a vague idea of the variables that influence the measurements. For example, contamination of the surfaces is likely to play an important role. In order to do a repeatable experiment, one obvious solution is to clean the surfaces with an oxygen plasma. However valuable, in a real MEMS device, the surface is not likely to stay clean for very long, so the results once more have a very limited predictive power for real world meso-scale contacts.

It is possible to repeat the experiments discussed in this thesis here under more carefully controlled atmospheric conditions and temperatures. In order to obtain results of statistical significance, they should be repeated under identical conditions with multiple devices per experimental parameter. This could provide valuable information for the design and reliability analysis of MEMS devices. However, because the surface roughness and microstructure of the contacting surfaces, it is doubtful how repeatable the obtained results are for experiments run under the same atmospheric conditions, but with devices produced in a different microfabrication process. These experiments are therefore better left to commercial MEMS foundries, in order to provide their clients with data on the tribological behavior of their MEMS devices. In order to further the fundamental research on meso-scale contact mechanics, a different approach should be taken, accepting that no experiment will result in a generic outcome that applies to every MEMS device, every time, and to embrace the unpredictability of the experimental results, rather than to fight it.

Instead, experiments should be designed such that as much information is known about the environment, the surfaces, and the microstructure of the devices under test as possible.

For example, it would be highly valuable to include an IR-spectrometer, or a Raman spectrometer in the microscope setup, such that the changes of the surface texture and chemical composition can be measured *in situ*, while an adhesion or friction experiment is running.

8.1. MORE EXPERIMENTS

In order to confirm that the viscoelastic behavior observed in the adhesion and friction measurement indeed has the same physical origin, a similar friction experiment could be set up, interspersing the sliding cycles with adhesion measurement along the sliding track. In order to deliver a final proof for the existence of the viscoelastic compound, the worn surfaces should be further analyzed using high resolution Scanning Electron Microscope (SEM) and Transmission Electron Microscopy (TEM) measurements performed shortly after the adhesion or friction experiments. It might even be worth it to execute a long running adhesion or friction experiment inside the chamber of a SEM, so the physical changes to the surfaces can be monitored *in situ*. However, because a SEM can only operate under vacuum conditions, the results are likely to differ from results obtained at atmospheric pressure.

8.2. IMPROVEMENTS TO THE OPTICAL DISPLACEMENT MEASUREMENT SYSTEM

Besides expanding the capabilities for *in situ* monitoring of additional variables as described above, there a many ways to improve the optical displacement measurement technique itself, which will enable many new experiments.

8.2.1. SIMULTANEOUS MEASUREMENT OF DIFFERENT REGIONS

To obtain a more accurate picture of what exactly happens in the tribometer during a friction measurement, especially when measured at high speed, it would be of great value to be able to monitor the displacements of both the slider and the loader, and each in two directions. This requires a modification of the acquisition software, which should allow for multiple regions of interest to be recorded simultaneously. This improvement would enable the aforementioned measurement scenario, in which adhesion curves are acquired in between friction measurements to provide information about the evolution of the local adhesion force. This experiment does not strictly require simultaneous measurement of the slider and the loader displacements.

When the displacements of the slider and the loader are measured simultaneously however, the loader is essentially turned into an AFM. For every position of the slider, the orthogonal loader displacement carries information about the combined height of the contacting surfaces. Although no traditional 2D surface plot can be obtained, the loader displacement provides a direct measure for the evolution of the surface roughness.

8.2.2. REAL-TIME ANALYSIS OF MEASUREMENT DATA

The software that currently controls the acquisition of images used as input for our displacement detection algorithm should be extended to allow real-time analysis of the image data. The curve-fit algorithm is able to process about 1000 images per second, which is already faster than the low speed friction measurements we have presented in chapter 6. Calculating the displacements directly after the image has been acquired saves a lot of time currently spent in post-processing the data. It would also enable real time calculation of the noise figure, which would simplify configuring an experiment. Most importantly though, it allows stick–slip and adhesion snap-off events to be detected in real-time which opens up an enormous amount of possibilities.

Instead of measuring repeated adhesion snap-in and snap-off by actuating the loader with a repeating waveform, the flow of the experiment would become much more dynamic. For example: the actuator voltage is slowly increased, with the smallest possible step size. When snap-in is detected, the experiment is immediately paused for a fixed amount of time, $T_{\text{snap-in}}$, allowing the contact to stabilize. Then the applied normal force is increased at a rate of $\dot{F}_{\text{push}}$ to the maximum pushing force F_{max} and the contact is allowed to relax for $T_{F_{\text{max}}}$. Then, the normal force is decreased at a rate of $\dot{F}_{\text{relax}}$ to the value where snap-in occurred, and is then further decreased at a different rate $\dot{F}_{\text{pull}}$ until snap-off is detected. The experiment is then paused for a fixed amount of time to allow the contact to stabilize, and the cycle repeats.

This measurement unlocks no less than 6 new experimental variables that can be controlled independently. In addition, the cycle rate will become much faster, and much less data will need to be stored per cycle, because storage of the approach and retract curves is no longer needed.

8.2.3. SINGLE PICOMETER PER SQRT-HERTZ

It should be possible to develop a MEMS tribometer capable of providing a displacement noise figure of $1\,\text{pm}/\sqrt{\text{Hz}}$, which is equivalent to a resolution of 0.2 nm at 100 000 fps. This will enable the measurement of friction loops and adhesion curves of similar quality as the measurements shown in chapter 6, while capturing the stick–slip dynamics of the slider and loader as a function of time. A first step could be to optimize the current design of the tribometers, by using larger, repetitive structures for measuring displacements. More radical changes might be necessary, such as coating the surface with metal to make it more reflective, or even by completely etching away the substrate from underneath the detection features to obtain a darker background.

Assuming that these measures will improve the contrast by a factor of 10, and that a grating of 60 parallel beams is used to measure displacements, this decreases our current noise figure of $35.3\,\text{pm}/\sqrt{\text{Hz}}$ to $1/\sqrt{600} \times 35.3\,\text{pm}/\sqrt{\text{Hz}} \approx 1\,\text{pm}\sqrt{\text{Hz}}$.

8.2.4. DYNAMIC DATA STORAGE AND PARALLEL PROCESSING

The combination of 1 pm/$\sqrt{\text{Hz}}$ resolution and measuring in real-time, with automated dynamic control logic would yield the ultimate measurement system for meso-scale contact mechanics. It will become possible to measure the evolution of friction and adhesion forces for billions of consecutive cycles without the need to periodically perform sets of unrecorded cycles at a higher rate to decrease the total measurement time. However, the data sets produced by these experiments will be truly enormous. Imagine a similar friction experiment as the friction experiment of chapter 6, but at a fixed sliding rate of 10 Hz, while recording the displacements of both the slider and the loader at 100 000 fps. Assuming the width of the observed regions of interest of the loader and the slider is 500 pixels, this would produce $10^5 \times 500 \times 2 = 10^8$ intensity profiles per second, or 100 MB/s assuming a rather meager 8-bit resolution. For an experiment of one million sliding cycles, this would require 10 TB of storage, which easily exceeds the capacity of a single hard drive at the time of writing.

Managing and analyzing data sets stored in a distributed database is non-trivial, and it is in fact an active field of research by itself. However, when the displacement analysis is carried out while the experiment runs, the raw data can be discarded, or streamed to a magnetic tape archive. Assuming only the displacement data is kept, this would require only 10 GB of storage, which is much more reasonable.

Because displacement results are available in real time, a decision of whether or not the data is interesting enough to keep, can be taken automatically by a simple algorithm. For each measured friction loop, the data can be run through a running average filter and sub-sampled to a few thousand data points. This yields a similar friction loop as shown in chapter 6, but with a much higher resolution. For the stick sections of the loop, the high-speed information can be discarded, but for the slip sections of the loop it should be kept. The result will be a tidy dataset of force–displacement curves with numbered sections, and a supplementary dataset of time–displacement curves for every single occurrence of stick–slip motion.

REFERENCES

[1] A. G. Layard. *Discoveries in the Ruins of Nineveh and Babylon, I and II*. 1853.

[2] L. Prandtl. "A Conceptual Model to the Kinetic Theory of Solid Bodies". In: *Zeitschrift für angewandte mathematik und mechanik* (1928).

[3] Y. Bar-Sinai, R. Spatschek, E. A. Brener, and E. Bouchbinder. "On the velocity-strengthening behavior of dry friction". In: *Journal of Geophysical Research: Solid Earth* 119.3 (Mar. 2014), pp. 1738–1748. DOI: 10.1002/2013jb010586.

[4] J. H. Dieterich and B. D. Kilgore. "Direct observation of frictional contacts: New insights for state-dependent properties". In: *Pure and Applied Geophysics PAGEOPH* 143.1-3 (1994), pp. 283–302. DOI: 10.1007/bf00874332.

[5] F. Heslot, T. Baumberger, B. Perrin, B. Caroli, and C. Caroli. "Creep, stick-slip, and dry-friction dynamics: Experiments and a heuristic model". In: *Phys. Rev. E* 49.6 (June 1994), pp. 4973–4988. DOI: 10.1103/physreve.49.4973.

[6] J. R. Rice and A. L. Ruina. "Stability of Steady Frictional Slipping". In: *J. Appl. Mech.* 50.2 (1983), p. 343. DOI: 10.1115/1.3167042.

[7] A. Ruina. "Slip instability and state variable friction laws". In: *Journal of Geophysical Research: Solid Earth* 88.B12 (Dec. 1983), pp. 10359–10370. DOI: 10.1029/jb088ib12p10359.

[8] G. E. Moore. "Cramming more components onto integrated circuits". In: *Electronics* 38.8 (1965), p. 114. DOI: 10.1109/N-SSC.2006.4785860.

[9] H. H. P. Garza, M. K. Ghatkesar, and U. Staufer. "Combined AFM—nanopipette cartridge system for actively dispensing femtolitre droplets". In: *Journal of Micro-Bio Robotics* 8.1 (Jan. 2013), pp. 33–40. DOI: 10.1007/s12213-013-0064-6.

[10] F. Tabak, E. Disseldorp, G. Wortel, A. Katan, M. Hesselberth, T. Oosterkamp, J. Frenken, and W. van Spengen. "MEMS-based fast scanning probe microscopes". In: *Ultramicroscopy* 110.6 (May 2010), pp. 599–604. DOI: 10.1016/j.ultramic.2010.02.018.

[11] N. Tas, J. Wissink, L. Sander, T. Lammerink, and M. Elwenspoek. "Modeling, design and testing of the electrostatic shuffle motor". In: *Sensors and Actuators A: Physical* 70.1-2 (Oct. 1998), pp. 171–178. DOI: 10.1016/s0924-4247(98)00129-0.

[12] J. Groenesteijn, H. Droogendijk, R. J. Wiegerink, T. S. J. Lammerink, J. C. Lötters, R. G. P. Sanders, and G. J. M. Krijnen. "Parametric amplification in a micro Coriolis mass flow sensor". In: *Journal of Applied Physics* 115.19 (May 2014), p. 194503. DOI: 10.1063/1.4876741.

[13] T. J. Peters and M. Tichem. “On-chip positionable photonic waveguides for chip-to-chip optical interconnects”. In: *SPIE Proceedings*. Vol. 9891. Silicon Photonics and Photonic Integrated Circuits V. 2016, 98911S–10. DOI: 10.1117/12.2222512.

[14] H. B. Profijt, C. Pigot, G. Reyne, R. M. Grechishkin, and O. Cugat. “Stable diamagnetic self-levitation of a micro-magnet by improvement of its magnetic gradients”. English. In: *J. Magn. Magn. Mater.* 321.4 (2009), pp. 259–262. ISSN: 0304-8853. DOI: 10.1016/j.jmmm.2008.08.115.

[15] J. Kokorian, J. B. C. Engelen, J. de Vries, H. Nazeer, L. A. Woldering, and L. Abelmann. “Ultra-flat bismuth films for diamagnetic levitation by template-stripping”. In: *Thin Solid Films* 550.0 (Jan. 2014), pp. 298–304. ISSN: 0040-6090. DOI: 10.1016/j.tsf.2013.11.074.

[16] H. Chetouani, C. Jeandey, V. Haguet, H. Rostaing, C. Dieppedale, and G. Reyne. “Diamagnetic Levitation With Permanent Magnets for Contactless Guiding and Trapping of Microdroplets and Particles in Air and Liquids”. In: *IEEE Transactions on Magnetics* 42.10 (Oct. 2006), pp. 3557–3559. DOI: 10.1109/tmag.2006.880921.

[17] W. M. van Spengen. “A physical model to describe the distribution of adhesion strength in MEMS, or why one MEMS device sticks and another ‘identical’ one does not”. In: *J. Micromech. Microeng.* 25.12 (2015), p. 125012. DOI: 10.1088/0960-1317/25/12/125012.

[18] K. B. Jinesh and J. W. M. Frenken. “Capillary condensation in atomic scale friction: How water acts like a glue”. In: *Phys. Rev. Lett.* 96 (2006), p. 166103. ISSN: 00319007 (ISSN). DOI: 10.1103/PhysRevLett.96.166103.

[19] K. B. Jinesh and J. W. M. Frenken. “Experimental Evidence for Ice Formation at Room Temperature”. In: *Physical Review Letters* 101.3 (July 2008). DOI: 10.1103/physrevlett.101.036101.

[20] M. Dienwiebel, G. S. Verhoeven, N. Pradeep, J. W. M. Frenken, J. A. Heimberg, and H. W. Zandbergen. “Superlubricity of graphite”. In: *Phys. Rev. Lett.* 92.12 (2004), pp. 126101–1. ISSN: 00319007 (ISSN). DOI: 10.1103/PhysRevLett.92.126101.

[21] A. Socoliuc, R. Bennewitz, E. Gnecco, and E. Meyer. “Transition from stick-slip to continuous sliding in atomic friction: entering a new regime of ultralow friction”. In: *Phys. Rev. Lett.* 92.13 (2004), p. 134301. DOI: 10.1103/PhysRevLett.92.134301.

[22] W. M. van Spengen. “Hints of atomic scale phenomena in adhesion and friction measurements with MEMS devices”. In: *Tribology* 4.3 (2010), pp. 115–120. ISSN: 17515831 (ISSN). DOI: 10.1179/175158310X12678019274165.

[23] J. Kokorian, F. Buja, and W. M. van Spengen. “In-plane displacement detection with picometer accuracy on a conventional microscope”. In: *J. Microelectromech. Syst.* 24.3 (2015), pp. 618–625. DOI: 10.1109/JMEMS.2014.2335153.

[24] W. Kuehnel and S. Sherman. “A surface micromachined silicon accelerometer with on-chip detection circuitry”. In: *Sens Actuators A Phys* 45.1 (1994), pp. 7–16. ISSN: 09244247 (ISSN). DOI: 10.1016/0924-4247(94)00815-9.

[25] E. M. Lawrence, K. E. Speller, and D. Yu. “MEMS characterization using Laser Doppler Vibrometry”. In: vol. 4980. 2003, pp. 51–62. DOI: 10.1117/12.478195.

[26] S. Ellingsrud and G. O. Rosvold. “Analysis of a data-based TV-holography system used to measure small vibration amplitudes”. In: *J. Opt. Soc. Am. A* 9.2 (1992), pp. 237–251. DOI: 10.1364/JOSAA.9.000237.

[27] S. H. Wang, C. Quan, C. J. Tay, I. Reading, and Z. P. Fang. “Deformation measurement of MEMS components using optical interferometry”. In: *Meas. Sci. Technol.* 14.7 (2003), pp. 909–915. ISSN: 09570233 (ISSN). DOI: 10.1088/0957-0233/14/7/303.

[28] M. R. Hart, R. A. Conant, K. Y. Lau, and R. S. Muller. “Stroboscopic interferometer system for dynamic MEMS characterization”. In: *J. Microelectromech. Syst.* 9.4 (2000), pp. 409–418. ISSN: 10577157 (ISSN). DOI: 10.1109/84.896761.

[29] A. Bosseboeuf and S. Petitgrand. “Characterization of the static and dynamic behaviour of M(O)EMS by optical techniques: Status and trends”. In: *J Micromech Microengineering* 13.4 (2003), S23–S33. ISSN: 09601317 (ISSN). DOI: 10.1088/0960-1317/13/4/304.

[30] G. F. LaVigne and S. L. Miller. “A performance analysis system for MEMS using Automated Imaging Methods”. In: *Proceedings of IEEE International Testing Conference*. 1998, pp. 442–447. DOI: 10.1109/TEST.1998.743184.

[31] B. Serio, J. J. Hunsinger, and B. Cretin. “In-plane measurements of microelectromechanical systems vibrations with nanometer resolution using the correlation of synchronous images”. In: *Rev. Sci. Instrum.* 75.10 I (2004), pp. 3335–3341. ISSN: 00346748 (ISSN). DOI: 10.1063/1.1791337.

[32] A. Ya’akobovitz, S. Krylov, and Y. Hanein. “Nanoscale displacement measurement of electrostatically actuated micro-devices using optical microscopy and digital image correlation”. In: *Sens Actuators A Phys* 162.1 (2010), pp. 1–7. ISSN: 09244247 (ISSN). DOI: 10.1016/j.sna.2010.05.014.

[33] C. Q. Davis and D. M. Freeman. “Using a light microscope to measure motions with nanometer accuracy”. In: *Opt. Eng.* 37.4 (1998), pp. 1299–1304. ISSN: 00913286 (ISSN). DOI: 10.1117/1.601967.

[34] T. Guo, H. Chang, J. Chen, X. Fu, and X. Hu. “Micro-motion analyzer used for dynamic MEMS characterization”. In: *Opt. Lasers Eng.* 47.3-4 (2009), pp. 512–517. ISSN: 01438166 (ISSN). DOI: 10.1016/j.optlaseng.2008.09.006.

[35] A. Hafiane, S. Petitgrand, O. Gigan, S. Bouchafa, and A. Bosseboeuf. “Study of subpixel image processing algorithms for MEMS in-plane vibration measurements by stroboscopic microscopy”. In: *Microsystems Engineering: Metrology and Inspection III*. Ed. by G. C. Vol. 5145. Munich, 2003, pp. 169–179. DOI: 10.1117/12.500141.

[36] S. Petitgrand and A. Bosseboeuf. “Simultaneous mapping of out-of-plane and in-plane vibrations of MEMS with (sub)nanometer resolution”. In: *J Micromech Microengineering* 14.9 (2004), S97–S101. ISSN: 09601317 (ISSN). DOI: 10.1088/0960-1317/14/9/017.

[37] B. Kleinemeier. “Measurement of CCD interpolation functions in the subpixel precision range”. In: *Proc SPIE Int Soc Opt Eng.* Vol. 1010. 1988, pp. 158–165. DOI: 10.1117/12.949242.

[38] C. Q. Davis and D. M. Freeman. "Statistics of subpixel registration algorithms based on spatiotemporal gradients or block matching". In: *Opt. Eng.* 37.4 (1998), pp. 1290–1298. ISSN: 00913286 (ISSN). DOI: 10.1117/1.601966.

[39] C. Yamahata, E. Sarajlic, G. J. M. Krijnen, and M. A. M. Gijs. "Subnanometer translation of microelectromechanical systems measured by discrete fourier analysis of CCD images". In: *J. Microelectromech. Syst.* 19.5 (2010), pp. 1273–1275. ISSN: 10577157 (ISSN). DOI: 10.1109/JMEMS.2010.2067445.

[40] D. J. Burns and H. F. Helbig. "System for automatic electrical and optical characterization of microelectromechanical devices". In: *J. Microelectromech. Syst.* 8.4 (1999), pp. 473–482. ISSN: 10577157 (ISSN). DOI: 10.1109/84.809063.

[41] H. Yu, G. Zhou, S. Kumar Sinha, and F. S. Chau. "Scanning grating based in-plane movement sensing". In: *J Micromech Microengineering* 20.8 (2010), p. 085007. ISSN: 09601317 (ISSN). DOI: 10.1088/0960-1317/20/8/085007.

[42] A. Hachicha and S. Simon. "Subpixel edge detection for precise measurements by a vision system." In: *Proc SPIE Int Soc Opt Eng.* Vol. 1010. IBM Paris Scientific Center, 3, Place vendome, 75001 Paris, France, 1988, pp. 148–157. DOI: 10.1117/12.949239.

[43] W. M. van Spengen and J. B. Roca. "On the noise limit of stress and temperature measurements with micro-Raman spectroscopy". In: *J. Raman Spectrosc.* 44.7 (2013), pp. 1039–1044. ISSN: 03770486 (ISSN). DOI: 10.1002/jrs.4314.

[44] W. M. van Spengen and J. W. M. Frenken. "The Leiden MEMS tribometer: Real time dynamic friction loop measurements with an on-chip tribometer". In: *Tribol. Lett.* 28.2 (2007), pp. 149–156. ISSN: 10238883 (ISSN). DOI: 10.1007/s11249-007-9259-0.

[45] W. M. van Spengen. "The accuracy of parameter estimation by curve fitting in the presence of noise". In: *J. Appl. Phys.* 111.5 (2012), p. 054908. ISSN: 00218979 (ISSN). DOI: 10.1063/1.3688298.

[46] W. M. van Spengen, G. H. C. J. Wijts, V. Turq, and J. W. M. Frenken. "Microscale friction reduction by normal force modulation in MEMS". In: *J. Adhes. Sci. Technol.* 24.15-16 (2010), pp. 2669–2680. ISSN: 01694243 (ISSN). DOI: 10.1163/016942410X508226.

[47] F. Buja, A. V. Sumant, J. Kokorian, and W. M. van Spengen. "Electrically Conducting Ultrananocrystalline Diamond for the Development of a Next Generation of Micro-Actuators". In: *Sens. Actuators, A* 214.0 (2014), pp. 259–266. ISSN: 0924-4247. DOI: 10.1016/j.sna.2014.04.042.

[48] J. Kokorian, F. Buja, U. Staufer, and W. M. van Spengen. "An optical in-plane displacement measurement technique with sub-nanometer accuracy based on curve-fitting". In: *2014 IEEE 27th International Conference on Micro Electro Mechanical Systems (MEMS)*. 2014, pp. 580–583. DOI: 10.1109/MEMSYS.2014.6765707.

[49] J. Kokorian. *ODMAnalysis*. URL: github.com/jkokorian/ODMAnalysis.

[50] M. Giesen, R. Kowarsch, W. Ochs, M. Winter, and C. Rembe. "Optical vibration analysis of MEMS devices with pm-resolution in x, y, and z directions". In: *Optical Measurement Systems for Industrial Inspection VIII*. Ed. by P. H. Lehmann, W. Osten, and A. Albertazzi. SPIE, May 2013. DOI: 10.1117/12.2019342.

[51] S. S. Shroff and M. P. de Boer. “Full Assessment of Micromachine Friction Within the Rate–State Framework: Experiments”. In: *Tribol. Lett.* 63.3 (July 2016). DOI: 10.1007/s11249-016-0718-3.

[52] F. Buja, J. Kokorian, A. V. Sumant, and W. M. van Spengen. “Studies on measuring surface adhesion between sidewalls in boron doped ultrananocrystalline diamond based microelectromechanical devices”. In: *Diamond Relat. Mater.* 55.0 (May 2015), pp. 22–31. ISSN: 0925-9635. DOI: 10.1016/j.diamond.2015.02.008.

[53] A. Gkouzou, J. Kokorian, G. C. A. M. Janssen, and W. M. van Spengen. “Controlling adhesion between multi-asperity contacting surfaces in MEMS devices by local heating”. In: *J. Micromech. Microeng.* 26.9 (2016), p. 095020. DOI: 10.1088/0960-1317/26/9/095020.

[54] J. Kokorian, U. Staufer, and W. M. van Spengen. “Atomic scale adhesion phenomena in a two million cycle sidewall contact experiment”. In: *Proceedings of the 18th International Conference on Solid-State Sensors, Actuators and Microsystems (Transducers)*. June 2015, pp. 772–775. DOI: 10.1109/TRANSDUCERS.2015.7181037.

[55] F. Buja, J. Kokorian, A. V. Sumant, and W. M. van Spengen. “First adhesion measurements of conductive ultrananocrystalline diamond MEMS sidewalls”. In: *Nano/Micro Engineered and Molecular Systems (NEMS), 2014 9th IEEE International Conference on*. IEEE, 2014, pp. 77–80. DOI: 10.1109/NEMS.2014.6908763.

[56] F. Buja, G. Fiorentino, J. Kokorian, and W. M. van Spengen. “Observation of nanoscale adhesion, friction and wear between ALD Al_2O_3 coated silicon MEMS sidewalls”. In: *Nanotechnology* 26.25 (2015), p. 255701. DOI: 10.1088/0957-4484/26/25/255701.

[57] F. Buja, J. Kokorian, R. Gulotty, A. V. Sumant, and W. M. van Spengen. “Observation of a Carbon Based Protective Layer on the Sidewalls of Boron Doped Ultrananocrystalline Diamond Based MEMS During in-situ Tribotests”. In: *J. Micromech. Microeng.* (2015). DOI: 10.1088/0960-1317/25/12/125020.

[58] A. Gkouzou, J. Kokorian, G. C. A. M. Janssen, and W. M. van Spengen. “A study of nanoscale friction in MEMS devices with heated contacting surfaces”. In: *Proceedings of the 2015 Nanomechanical Sensing Workshop (unpublished)*. 2015.

[59] W. M. van Spengen, R. Puers, R. Mertens, and I. De Wolf. “Characterization and failure analysis of MEMS: High resolution optical investigation of small out-of-plane movements and fast vibrations”. In: *Microsyst. Technol.* 10.2 (2004), pp. 89–96. ISSN: 09467076 (ISSN). DOI: 10.1007/s00542-003-0326-7.

[60] W. M. van Spengen and E. C. Heeres. “A method to extract the lateral and normal components of motion from the capacitance change of a moving MEMS comb drive”. In: *J. Micromech. Microeng.* 17.3 (2007), pp. 447–451. ISSN: 09601317 (ISSN). DOI: 10.1088/0960-1317/17/3/005.

[61] M. W. Van Spengen, E. Bakker, and J. W. M. Frenken. “A ‘nano-battering ram’ for measuring surface forces: Obtaining force-distance curves and sidewall stiction data with a MEMS device”. In: *J. Micromech. Microeng.* 17.7 (2007), S91–S97. ISSN: 09601317 (ISSN). DOI: 10.1088/0960-1317/17/7/S05.

[62] C. Antoine. “Tensions des vapeurs; nouvelle relation entre les tensions et les températures”. In: *Comptes Rendus des Séances de l’Académie des Sciences* 107 (1888), pp. 681–684, 778–780, 836–837.

[63] W. McKinney. *Python for Data Analysis*. O’Reilly Media, 2012. ISBN: 978-1-4493-1979-3.

[64] W. M. van Spengen, V. Turq, and J. W. M. Frenken. “The description of friction of silicon MEMS with surface roughness: virtues and limitations of a stochastic Prandtl–Tomlinson model and the simulation of vibration-induced friction reduction”. In: *Beilstein J. Nanotechnol.* 1.1 (2010), pp. 163–171. DOI: 10.3762/bjnano.1.20.

[65] A. Gkouzou, J. Kokorian, G. C. A. M. Janssen, and W. M. van Spengen. “Friction and dynamically dissipated energy dependence on temperature in polycrystalline silicon MEMS devices”. In: *Microsystem Technologies* (Oct. 2017). DOI: 10.1007/s00542-017-3575-6.

[66] J. Kokorian and W. M. van Spengen. “The run-in and drift of the adhesive force between polycrystalline silicon MEMS sidewalls (accepted)”. In: *Microsystems Technology* (2020).

[67] R. W. Carpick and M. Salmeron. “Scratching the surface: Fundamental investigations of tribology with atomic force microscopy”. In: *Chem. Rev.* 97.4 (1997), pp. 1163–1194. ISSN: 00092665 (ISSN). DOI: 10.1021/cr960068q.

[68] R. Maboudian, W. R. Ashurst, and C. Carraro. “Tribological challenges in micromechanical systems”. In: *Tribol. Lett.* 12.2 (2002), pp. 95–100. ISSN: 10238883 (ISSN). DOI: 10.1023/A:1014044207344.

[69] D. B. Asay, M. T. Dugger, and S. H. Kim. “In-situ Vapor-Phase Lubrication of MEMS”. In: *Tribol. Lett.* 29.1 (2008), pp. 67–74. ISSN: 10238883 (ISSN). DOI: 10.1007/s11249-007-9283-0.

[70] Y. P. Zhao, L. S. Wang, and T. X. Yu. “Mechanics of adhesion in MEMS–a review”. In: *J. Adhes. Sci. Technol.* 17.4 (2003), pp. 519–546. DOI: 10.1163/15685610360554393. eprint: http://dx.doi.org/10.1163/15685610360554393.

[71] MEMSCap. URL: http://www.memscap.com/mems-development-and-manufacturing-services.

[72] R. Legtenberg, A. W. Groeneveld, and M. Elwenspoek. “Comb-drive actuators for large displacements”. In: *J. Micromech. Microeng.* 6.3 (1996), p. 320. DOI: 10.1088/0960-1317/6/3/004.

[73] Y. Huang, A. S. S. Vasan, R. Doraiswami, M. Osterman, and M. Pecht. “MEMS Reliability Review”. In: *Device and Materials Reliability, IEEE Transactions on* 12.2 (June 2012), pp. 482–493. ISSN: 1530-4388. DOI: 10.1109/TDMR.2012.2191291.

[74] C. Kosla, P. Fitzgerald, and M. Hill. “Continuous dynamic timing measurements to monitor spring and surface forces in MEMS switch reliability”. In: *27th IEEE International Conference on Micro Electro Mechanical Systems, MEMS 2014*. San Francisco, CA: Institute of Electrical and Electronics Engineers Inc., 2014, pp. 596–599. DOI: 0.1109/MEMSYS.2014.6765711.

[75] J. Kokorian and W. M. van Spengen. “Improved analysis and visualization of friction loop data: unraveling the energy dissipation of meso-scale stick–slip motion”. In: *Measurement Science and Technology* 28.11 (Oct. 2017), p. 115011. DOI: 10.1088/1361-6501/aa870a.

[76] J. Kokorian and W. M. van Spengen. “Corrigendum: Improved analysis and visualization of friction loop data: unraveling the energy dissipation of meso-scale stick–slip motion (2017 Meas. Sci. Technol. 28 115011)”. In: *Measurement Science and Technology* 30.9 (July 2019), p. 099501. DOI: 10.1088/1361-6501/ab1d19.

[77] C. M. Mate, G. M. McClelland, R. Erlandsson, and S. Chiang. “Atomic-scale friction of a tungsten tip on a graphite surface”. In: *Phys. Rev. Lett.* 59 (17 Oct. 1987), pp. 1942–1945. DOI: 10.1103/PhysRevLett.59.1942.

[78] R. Maboudian, W. R. Ashurst, and C. Carraro. “Self-assembled monolayers as anti-stiction coatings for MEMS: characteristics and recent developments”. In: *Sens. Actuators A* 82.1 (2000), pp. 219–223. DOI: 10.1016/S0924-4247(99)00337-4.

[79] W. R. Ashurst, C. Yau, C. Carraro, C. Lee, G. J. Kluth, R. T. Howe, and R. Maboudian. “Alkene based monolayer films as anti-stiction coatings for polysilicon MEMS”. In: *Sens. Actuators, A* 91.3 (July 2001), pp. 239–248. DOI: 10.1016/s0924-4247(01)00593-3.

[80] M. Mehregany, C. A. Zorman, N. Rajan, and C. H. Wu. “Silicon carbide MEMS for harsh environments”. In: *Proc. IEEE* 86.8 (1998), pp. 1594–1609. DOI: 10.1109/5.704265.

[81] J. Wu, S. Wang, and J. Miao. “A MEMS device for studying the friction behavior of micromachined sidewall surfaces”. In: *Journal of Microelectromechanical Systems* 17.4 (2008), pp. 921–933. DOI: 10.1109/JMEMS.2008.927179.

[82] I. S. Y. Ku, T. Reddyhoff, J. H. Choo, A. S. Holmes, and H. A. Spikes. “A novel tribometer for the measurement of friction in MEMS”. In: *Tribol. Int.* 43.5-6 (2010), pp. 1087–1090. ISSN: 0301679X (ISSN). DOI: 10.1016/j.triboint.2009.12.029.

[83] D. L. Luck, M. P. de Boer, W. R. Ashurst, and M. S. Baker. “Evidence for pre-sliding tangential deflections in MEMS friction”. In: *Proceedings of the 12th International Conference on Solid-State Sensors, Actuators and Microsystems (Transducers)*. Vol. 1. IEEE. 2003, pp. 404–407. DOI: 10.1109/SENSOR.2003.1215339.

[84] M. C. Elwenspoek. “Mechanism of anisotropic etching of silicon”. In: *J. Electrochem. Soc.* 140.7 (1993), pp. 2075–2080. ISSN: 00134651 (ISSN). DOI: 10.1149/1.2220767.

[85] J. D. Hunter. “Matplotlib: A 2D graphics environment”. In: *Computing In Science & Engineering* 9.3 (2007), pp. 90–95. DOI: 10.1109/MCSE.2007.55.

[86] D. B. Carr, R. J. Littlefield, W. L. Nicholson, and J. S. Littlefield. “Scatterplot Matrix Techniques for Large N”. In: *J. Am. Stat. Assoc.* 82.398 (June 1987), pp. 424–436. DOI: 10.1080/01621459.1987.10478445.

[87] M. C. Hao, U. Dayal, R. K. Sharma, D. A. Keim, and H. Janetzko. “Variable binned scatter plots”. In: *Information Visualization* 9.3 (2010), pp. 194–203. DOI: 10.1057/ivs.2010.4.

[88] Q. Yao and Q. Li. “Line Scan Reconstruction: A Viable Approach for Tracking Atomic Stick–Slip Events and True Tip Position in Atomic Force Microscopy”. In: *Tribol. Lett.* 64.2 (2016), p. 31. ISSN: 1573-2711. DOI: 10.1007/s11249-016-0761-0.

[89] ““Coefficient of Friction””. In: *CRC Handbook of Chemistry and Physics, internet version*. Ed. by W. M. Haynes. 96nd. Boca Raton, FL, USA: CRC Press/Taylor and Francis, 2016. Chap. Coefficient of Friction (15-48). URL: http://hbcponline.com/faces/contents/InteractiveTable.xhtml?tableId=364.

[90] J. C. Maxwell. “Letter to Lewis Campbell”. In: *The life of James Clerk Maxwell*. Cambridge University Press, 1990. Chap. 6, p. 159.

[91] W. M. van Spengen. “Recent developments in experimental on-chip stiction research: A review”. In: *Int. J. Comput. Mater. Sci. Surf. Eng.* 2.3-4 (2009), pp. 186–207. ISSN: 17533465 (ISSN). DOI: 10.1504/IJCMSSE.2009.027482.

[92] J. Kokorian and W. M. van Spengen. “Exposing the tribological run-in of polysilicon MEMS sidewalls in sliding contact using in-situ force measurements with AFM-like resolution”. In: *41st international conference on micro- and nanofabrication and manufacturing*. 2015.

[93] A. Gkouzou, J. Kokorian, G. C. A. M. Janssen, and W. M. van Spengen. “Temperature-dependent friction between locally heated microscale surfaces”. In: *The second european workshop on understanding and controlling nano and mesoscale friction*. 2016.

SUMMARY

The strange and unpredictable behavior of meso-scale adhesion and friction forces is a practical problem for the development of microelectromechanical systems (MEMS) with contacting surfaces. To overcome the associated limitations when designing MEMS devices, the first obstacle to remove is the fact that it is hard to measure displacements and forces in MEMS with sufficient resolution to discern atomic scale details from these meso-scale measurements.

In this PhD thesis we show how an non-invasive, optical method can be used to measure forces and displacements in MEMS with sub-nanometer resolution. It is fundamentally impossible to optically measure topological details below 500 nm in size, due to the wave-like nature of light. However, the location of a moving feature can be tracked with a much higher resolution, by curve-fitting a mathematical function to its shape.

We demonstrate how this curve-fitting method can be used to measure displacements with resolution of ~0.2 nm in a typical adhesion or friction force measurement. We have use this technique with several different cameras, including a low noise, large pixel Charge-Coupled Device (CCD) camera and a high-speed Complementary Metal-Oxide-Semiconductor (CMOS) line scan camera. Although the absolute displacement resolution scales with the square-root of the exposure time, the noise figure per bandwidth was found to be similar for both cases, ~35 pm/$\sqrt{\text{Hz}}$, which proves that resolution limit of these measurements is determined solely by the photon shot noise of the light used to acquire the images.

We applied our curve-fitting technique to measure adhesion forces between the sidewalls of MEMS adhesion sensors using an unprecedented subnanometer and subnanonewton displacement- and force resolution. We measured the evolution of the adhesion force in several 'identical' MEMS devices during millions of repeated contacts. We observed that their behavior is vastly different. However, we found that the magnitude and variability of the adhesion force stabilizes after about fifty thousand cycles. After a quarter of a million cycles, the adhesion forces began to drift again, and no stabilization was observed until the experiment was stopped after a total of three million cycles.

In some adhesion experiments, we have observed a 'gradual pullback' of several nanometers before the moving loader of the MEMS adhesion sensor snaps off from the counter surface it was pushing against. The origins of this effect may differ from case to case. We believe we have seen evidence of viscous tribochemical compounds being synthesized at the contact.

We also applied our curve-fitting technique to measure friction forces between the sidewalls of MEMS tribometers, again with a sub-nanometer and sub-nanonewton resolution. We propose an intuitive way of visualizing friction loops obtained from MEMS tribometer measurements. We were able to detect stick–slip events automatically from the resulting data. This allowed us to separate the dissipated energy into two contributions: the 'semi statically dissipated energy', which is dissipated during stick, and the 'dynamically dissipated energy', which is dissipated during slip.

The atomic scale details resulting from the adhesion and friction measurements clearly demonstrate the potential of our optical measurement technique, applied to *in situ* measurements of MEMS devices. By further optimizing the geometry of the MEMS tribometers, the noise figure of the measurements can be pushed down towards $1\,\mathrm{pm}/\sqrt{\mathrm{Hz}}$. By performing the curve-fit analysis in real time, while images are being captured at high speed, many more discoveries will be made, and a better fundamental understanding of contact mechanics at the meso-scale is within our grasp.

SAMENVATTING

Het vreemde en onvoorspelbare gedrag van adhesie- en wrijvingskrachten op mesoschaal vormt een groot praktisch probleem voor de ontwikkeling van microelectromechanische systemen met wrijvende onderdelen. Dit is een enorme beperking voor de ontwerpvrijheid, en dat moet worden opgelost. Het eerste obstakel dat overwonnen moet worden is dat het erg moeilijk is om verplaatsingen en krachten te meten met voldoende resolutie om atomaire details te destilleren uit metingen op mesoschaal.

In dit proefschrift demonstreren we hoe een non-invasieve, optische methode kan worden gebruikt om krachten en verplaatsingen te meten in MEMS, met subnanometer-resolutie. Het is fundamenteel onmogelijk om optische details te onderscheiden die kleiner zijn dan 500 nm, vanwege de golflengte van licht. De locatie van een bewegend onderdeeltje echter, kan met een veel hogere resolutie worden gedetecteerd, door een mathematische functie die de vorm van het onderdeel beschrijft, te 'fitten' op een afbeelding.

We demonstreren hoe deze curve-fit methode can worden gebruikt om verplaatsingen te meten met een resolutie van 0.2 nm in een typische adhesie- of wrijvingskrachtmeting. We hebben deze techniek gebruikt met meerdere soorten camera's, waaronder een CCD-camera met grote pixels en een lage elektronische ruis, en een hoge snelheid lijnscancamera. Hoewel de absolute resolutie van de verplaatsingsmetingen schaalt met de wortel van de belichtingstijd, blijft de ruis per bandbreedte hetzelfde ongeacht welke camera er gebruikt wordt; ongeveer 35 pm/$\sqrt{\text{Hz}}$. Dit bewijst dat de resolutielimiet van dit soort metingen uitsluitend bepaald wordt door de shot-noise die van nature aanwezig is in het licht waarmee de camerabeelden worden gemaakt.

We hebben onze curve-fit techniek gebruikt om adhesiekrachten tussen twee elkaar rakende onderdelen van een MEMS adhesie sensor te meten met een ongekend lage subnanometer- en subnanonewton-resolutie. We hebben de evolutie van de adhesiekracht in een aantal 'identieke' MEMS devices gemeten, gedurende enkele miljoenen cycli van herhaalde contacten. Het blijkt dat de evolutie van de adhesiekracht erg verschilt van device tot device. De grootte en variabiliteit van de gemeten krachten stabiliseren na $\sim 50 \times 10^3$ cycli. Na 250×10^3 cycli beginnen de gemeten krachten weer uit elkaar te lopen. Geen verdere stabilisatie werd verder waargenomen tot het experiment werd stopgezet na een totaal van 3×10^6 cycli.

In een aantal adhesie-experimenten zagen we dat het beweegbare gedeelte van de adhesiesensor zich over een kleine afstand geleidelijk terugtrok, alvorens volledig los te komen. De oorzaken van dit effect verschillen per geval. We menen in een aantal gevallen bewijs te zien van een tribochemische stof die ter plekke in het contact wordt gesynthetiseerd.

Naast de adhesiemetingen, hebben we onze meettechniek ook gebruikt om wrijvingskrachten te meten tussen twee onderdelen van een MEMS tribometer, wederom met subnanometer-resolutie. We stellen een nieuwe manier voor om zogenaamde wrijvingslussen weer te geven op een intuïtievere wijze dan gebruikelijk. De hoge resolutie van de metingen stelde ons in staat om automatisch te identificeren wanneer er een plak–glij gebeurtenis plaats vind. Aan de hand daarvan is het mogelijk om twee verschillende vormen van energie dissipatie te meten: de semi-statische energie, die wordt gedissipeerd terwijl de onderdelen plakken, en de dynamische energie, die wordt gedissipeerd terwijl de onderdelen glijden.

De details van atomaire schaal die naar voren kwamen uit de adhesie- en wrijvingsmetingen laten duidelijk het grote potentieel van onze optische meetmethode zien, met name voor de toepassing van het *in situ* meten van krachten in MEMS devices. Door de geometrie van de adhesiesensors en tribometers specifiek voor gebruik met deze techniek te optimaliseren, zou de ruis verder moeten kunnen worden verminderd richting 1 $\mathrm{pm}/\sqrt{\mathrm{Hz}}$. Door de curve-fitanalyse in real-time, tijdens metingen op hoge snelheid uit te voeren, worden nog veel meer nieuwe ontdekkingen mogelijk, en ligt een fundamenteel beter begrip van contactmechanica op mesoschaal binnen handbereik.

Curriculum Vitæ

Jaap Kokorian was born on the 20th of November, 1983 in Paris, France, and relocated to the Netherlands shortly thereafter. He obtained a master of science degree in electrical engineering from the University of Twente in 2010, where he majored in microsystems engineering, focusing on the application of passive magnetic levitation in MEMS. After his graduation, he worked as a research engineer and scientific programmer at Wageningen University and Research Centre. Jaap returned to the field of microsystems engineering in may 2012 as a PhD candidate at the precision and microsystems engineering group at Delft University of Technology, which eventually resulted in this book. In February 2017, he entered the talent incubator program at Bright Society, and currently works as a software designer at Philips Healthcare.

LIST OF PUBLICATIONS

JOURNAL PUBLICATIONS

- J. Kokorian, F. Buja, and W. M. van Spengen. "In-plane displacement detection with picometer accuracy on a conventional microscope". In: *J. Microelectromech. Syst.* 24.3 (2015), pp. 618–625. DOI: 10.1109/JMEMS.2014.2335153
- F. Buja, A. V. Sumant, J. Kokorian, and W. M. van Spengen. "Electrically Conducting Ultrananocrystalline Diamond for the Development of a Next Generation of Micro-Actuators". In: *Sens. Actuators, A* 214.0 (2014), pp. 259–266. ISSN: 0924-4247. DOI: 10.1016/j.sna.2014.04.042
- F. Buja, J. Kokorian, A. V. Sumant, and W. M. van Spengen. "Studies on measuring surface adhesion between sidewalls in boron doped ultrananocrystalline diamond based microelectromechanical devices". In: *Diamond Relat. Mater.* 55.0 (May 2015), pp. 22–31. ISSN: 0925-9635. DOI: 10.1016/j.diamond.2015.02.008
- F. Buja, G. Fiorentino, J. Kokorian, and W. M. van Spengen. "Observation of nanoscale adhesion, friction and wear between ALD Al_2O_3 coated silicon MEMS sidewalls". In: *Nanotechnology* 26.25 (2015), p. 255701. DOI: 10.1088/0957-4484/26/25/255701
- F. Buja, J. Kokorian, R. Gulotty, A. V. Sumant, and W. M. van Spengen. "Observation of a Carbon Based Protective Layer on the Sidewalls of Boron Doped Ultrananocrystalline Diamond Based MEMS During in-situ Tribotests". In: *J. Micromech. Microeng.* (2015). DOI: 10.1088/0960-1317/25/12/125020
- A. Gkouzou, J. Kokorian, G. C. A. M. Janssen, and W. M. van Spengen. "Controlling adhesion between multi-asperity contacting surfaces in MEMS devices by local heating". In: *J. Micromech. Microeng.* 26.9 (2016), p. 095020. DOI: 10.1088/0960-1317/26/9/095020
- J. Kokorian and W. M. van Spengen. "Improved analysis and visualization of friction loop data: unraveling the energy dissipation of meso-scale stick–slip motion". In: *Measurement Science and Technology* 28.11 (Oct. 2017), p. 115011. DOI: 10.1088/1361-6501/aa870a
- A. Gkouzou, J. Kokorian, G. C. A. M. Janssen, and W. M. van Spengen. "Friction and dynamically dissipated energy dependence on temperature in polycrystalline silicon MEMS devices". In: *Microsystem Technologies* (Oct. 2017). DOI: 10.1007/s00542-017-3575-6

- J. Kokorian and W. M. van Spengen. "Corrigendum: Improved analysis and visualization of friction loop data: unraveling the energy dissipation of meso-scale stick–slip motion (2017 Meas. Sci. Technol. 28 115011)". In: *Measurement Science and Technology* 30.9 (July 2019), p. 099501. DOI: 10.1088/1361-6501/ab1d19
- J. Kokorian and W. M. van Spengen. "The run-in and drift of the adhesive force between polycrystalline silicon MEMS sidewalls (accepted)". In: *Microsystems Technology* (2020)
- J. Kokorian, J. B. C. Engelen, J. de Vries, H. Nazeer, L. A. Woldering, and L. Abelmann. "Ultra-flat bismuth films for diamagnetic levitation by template-stripping". In: *Thin Solid Films* 550.0 (Jan. 2014), pp. 298–304. ISSN: 0040-6090. DOI: 10.1016/j.tsf.2013.11.074

CONFERENCE CONTRIBUTIONS

- J. Kokorian, F. Buja, U. Staufer, and W. M. van Spengen. "An optical in-plane displacement measurement technique with sub-nanometer accuracy based on curve-fitting". In: *2014 IEEE 27th International Conference on Micro Electro Mechanical Systems (MEMS)*. 2014, pp. 580–583. DOI: 10.1109/MEMSYS.2014.6765707
- F. Buja, J. Kokorian, A. V. Sumant, and W. M. van Spengen. "First adhesion measurements of conductive ultrananocrystalline diamond MEMS sidewalls". In: *Nano/Micro Engineered and Molecular Systems (NEMS), 2014 9th IEEE International Conference on*. IEEE, 2014, pp. 77–80. DOI: 10.1109/NEMS.2014.6908763
- J. Kokorian, U. Staufer, and W. M. van Spengen. "Atomic scale adhesion phenomena in a two million cycle sidewall contact experiment". In: *Proceedings of the 18th International Conference on Solid-State Sensors, Actuators and Microsystems (Transducers)*. June 2015, pp. 772–775. DOI: 10.1109/TRANSDUCERS.2015.7181037
- J. Kokorian and W. M. van Spengen. "Exposing the tribological run-in of polysilicon MEMS sidewalls in sliding contact using in-situ force measurements with AFM-like resolution". In: *41st international conference on micro- and nanofabrication and manufacturing*. 2015
- A. Gkouzou, J. Kokorian, G. C. A. M. Janssen, and W. M. van Spengen. "A study of nanoscale friction in MEMS devices with heated contacting surfaces". In: *Proceedings of the 2015 Nanomechanical Sensing Workshop (unpublished)*. 2015
- A. Gkouzou, J. Kokorian, G. C. A. M. Janssen, and W. M. van Spengen. "Temperature-dependent friction between locally heated microscale surfaces". In: *The second european workshop on understanding and controlling nano and mesoscale friction*. 2016

ACKNOWLEDGEMENTS

This book would not have existed without the involvement of many others besides myself. Many thanks to my MEMS-tribology team mates, Alkisti Gkouzou and Federico Buja, and of course to my promotors Merlijn van Spengen and Urs Staufer. I am grateful to the PME laboratory staff Harry Jansen, Patrick van Holst and Rob Luttjeboer, for their help, insights and passionate involvement in my project, and for sharing the pride of developing my measurement setup.

I also thank the user committee members of Merlijn's Vidi project which funded this work: Anna Lisa Fasolino, Hartmut Fischer and Aniruda Sumant for their interest in this work.

I would like to thank all of my colleagues at PME for their help and friendship. Many thanks especially to Tjitte-Jelte Peters, for being an awesome office mate during the major part of a decade, and to Marli Guffens for having lunch with me almost every day during the major part of said major part. Thanks to Guido Janssen and Eleonoor Verlinden, for the many inspiring discussions. Special thanks my to friend Roel Müller, for pointing out a flaw in my calculations when I was about to hand in the first draft of this book.

Of course there are countless more people who where in some way involved in this project, or in my life in general, without whom this work could not have been completed. I will not attempt to name everyone here explicitly, but please know that I am grateful nonetheless.

With many ups and downs, my PhD project has been a hard but rewarding journey. I would not have made it until the end without the unwavering support of my close friends and my mother. Most of all, I thank Maaike Berkhout, for always believing in me, and for raising our wonderful daughter Merel with me.